ADVANCED SYSTEM DESIGN AND PERFORMANCE ANALYSIS FOR HIGH SPEED OPTICAL COMMUNICATIONS

A Dissertation
Presented to
The Academic Faculty

by

Jie Pan

In Partial Fulfillment
of the Requirements for the Degree
Doctor of Philosophy in the
School of Electrical and Computer Engineering

Georgia Institute of Technology
May 2015

ADVANCED SYSTEM DESIGN AND PERFORMANCE ANALYSIS FOR HIGH SPEED OPTICAL COMMUNICATIONS

Approved by:

Dr. Stephen E. Ralph, Advisor
School of Electrical and Computer Engineering
Georgia Institute of Technology

Dr. Sorin Tibuleac
School of Electrical and Computer Engineering
Georgia Institute of Technology

Dr. Gee-Kung Chang
School of Electrical and Computer Engineering
Georgia Institute of Technology

Dr. Ellen W. Zegura
School of Computer Science
Georgia Institute of Technology

Dr. Matthieu Bloch
School of Electrical and Computer Engineering
Georgia Institute of Technology

Date Approved: March 30, 2015

To my parents for their unconditional support and encouragement

ACKNOWLEDGEMENTS

I want to deliver my sincere graduates to a number of people, without whom this work would have not been possible.

Foremost, I am very grateful to my advisor, Professor Stephen Ralph. I want to thank him for his trust in taking me as his student and let me have the opportunity to pursue Ph.D study in Georgia Tech. He has always given valuable advice in both research and life. It is my great honor and pleasure to work with him as his student.

I also would like to thank Professors Gee-Kung Chang, Matthieu Bloch, Sorin Tibuleac, and Ellen W. Zegura for severing as my committee members, who have delivered valuable advice for improving the quality of this thesis.

Many thanks to all the graduate students in the Georgia Terabit consortium: Cheng Liu, Pierre Isautier, Sriharsha Kota Pavan, Justin Lavrencik, Jerrod Langston, Stuart Hughes, Michael Pratt, David Haupt, Yu-Ting Hsueh, and Andy Stark. Their advice and collaboration is always valuable to me and I enjoyed the four-year life in Georgia Tech because of them.

I want to express my thanks to my families for their love and encouragement. Finally, I would like to thank my boyfriend Wei Mu who is always there to support me.

TABLE OF CONTENTS

	Page
ACKNOWLEDGEMENTS	iv
LIST OF TABLES	vii
LIST OF FIGURES	viii
LIST OF ABBREVIATIONS	xiv
SUMMARY	xvii
CHAPTER	
1 Introduction	1
1.1 Terabit Super-channel System	5
1.2 In-band Crosstalk Analysis	11
1.3 Objectives	12
2 Fiber Optical Communication Systems	14
2.1 Optical Signal Generations	14
2.2 Transmission Channel Impairments	17
2.3 Coherent Receiver Structures	22
2.4 Introduction of Simulation Tools	31
3 DAC enabled Transmitter Pre-shaping	32
3.1 Least Mean Square Directed Transmitter Pre-shaping	32
3.2 Frequency Domain Transmitter Pre-shaping	36
3.3 Experimental Comparison and Validation	47
3.4 Transmitter CD Compensation	52
3.5 Chapter Summary	57
4 Receiver MIMO Digital Signal Processing	59

4.1 Nyquist System Configurations 59
4.2 Pre-requisite Process before ICI Compensation 63
4.3 Inter-Channel Crosstalk Cancellation 69
4.4 Viterbi-Viterbi Algorithm based Joint Carrier Recovery 85
4.5 Chapter Summary 89
5 Gaussian Noise Model Based In-band Crosstalk Analysis 91
5.1 The Gaussian Noise Model 92
5.2 Weighted In-band Crosstalk Metric 95
5.3 Equating Crosstalk Noise and ASE Noise 100
5.4 Performance Predictions and Nonlinear Crosstalk Analysis 104
5.5 Experimental Validations 111
5.6 Chapter Summary 116
6 Conclusions 117
6.1 Future Research Topics 118
REFERENCES 120

LIST OF TABLES

Page

Table 2.1. Examples of CMA algorithms for 64QAM polarization de-multiplexing. 27

Table 2.2. Important simulation parameters in Optism Rsoft..... 31

Table 4.1.Number of real additions and multiplications for LMS-ISI, LMS-ICI and MAP-ICI (p is the tap number. L is the sequence length). 79

LIST OF FIGURES

Page

Figure 1.1. Global IP traffic growth from 2013 to 2018. 1

Figure 1.2. Current 100 Gb/s system design and research trend in transmission beyond 100 Gb/s. 3

Figure 1.3. Spectra and temporal pulses for CO-OFDM and Nyquist-WDM systems. 6

Figure 1.4. Spectra of a) RC, b) RRC at different roll-offs. 8

Figure 2.1. IQ MZM structure with the transfer function. 16

Figure 2.2. Coherent receiver structure for one polarization. 24

Figure 2.3. Block diagrams of the discrete filter and square timing recovery. 26

Figure 2.4. Block diagram of Viterbi-Viterbi carrier phase recovery. 29

Figure 3.1. Transmitter DAC structure and receiver DSP Block Diagram (Post-filter and MLSE are not used for pre-shaping) [92] 34

Figure 3.2. Required OSNR at BER=10^{-3} versus transmitter electrical bandwidth for single channel PM-QPSK system. 36

Figure 3.3. Simulation block diagram for a 3×32 Gbaud PM-QPSK system [92]. 36

Figure 3.4. Required OSNR at BER=10^{-3} versus transmitter electrical filter bandwidths for 3×32 Gbaud PM-QPSK back-to-back system (channel spacing equals to the baud rate). 37

Figure 3.5. Required OSNR at BER=10^{-3} versus launch power for 3×32 Gbaud PM-QPSK system after 12×80 km SSMF transmission (channel spacing equals to the baud rate). 37

Figure 3.6. Frequency domain pre-shaper design scheme with spectra observed at different test points. 40

Figure 3.7. Spectra observed at different test points with frequency domain pre-shaping. 40

Figure 3.8. DD-LMS pre-shaper design scheme with spectra observed at different test points. 41

Figure 3.9. Spectra observed at different test points with DD-LMS pre-shaping. 41

Figure 3.10. a) Transmitter filter shape at different electrical bandwidths b) Frequency domain pre-shapers corresponding to different transmitter electrical bandwidths. c) DD-LMS pre-shapers corresponding to different transmitter electrical bandwidths..... 43

Figure 3.11. Required OSNR at BER=5×10^{-3} versus electrical filter bandwidths with and without pre-shaping, ... 44

Figure 3.12. Required OSNR at BER=5×10^{-3} versus number of filter taps at different transmitter electrical bandwidths with two pre-shaping methods (OSNR=28 dB). 44

Figure 3.13. a) Frequency domain pre-shapers corresponding to different channel estimation OSNR. b) DD-LMS pre-shapers corresponding to different channel estimation OSNR (transmitter bandwidth 7 GHz). 45

Figure 3.14. Required OSNR at BER=5×10^{-3} versus channel estimation OSNR at different transmitter electrical bandwidths with two pre-shaping methods (tap length is 40). 46

Figure 3.15. Estimated inverse channel frequency response: a) frequency domain, b) DD-LMS. 48

Figure 3.16. Experimental setup for a 32 Gbaud Nyquist PM-16QAM system with pre-shaping. 49

Figure 3.17. BER versus OSNR at different pre-shaper filter taps for two pre-shaping methods (channel OSNR is 30 dB). 49

Figure 3.18. BER versus OSNR at different channel estimation OSNR for two pre-shaping methods (pre-shaper tap length is 40). 50

Figure 3.19. BER versus OSNR for PM-QPSK signals at different baud rates using frequency domain pre-shaping (pre-shaper tap length is 40 and channel OSNR is 30 dB). 51

Figure 3.20. Received signal baseband spectrum plots for PM-QPSK signal at different baud rates without (top row) and with (lower row) frequency domain pre-shaping. 51

Figure 3.21. Received signal constellation (after carrier phase recovery) for PM-QPSK signal at different baud rates without (top row) and with (lower row) frequency pre-shaping. 52

Figure 3.22. CD pre-compensation transfer function amplitude and phase. 54

Figure 3.23. Required OSNR at BER=10^{-3} versus LO linewidth × bit duration of 32 Gbaud PM-QPSK system. With 12×80 km SSMF transmission, launch power=-1 dBm. For 32 Gbaud, $log_{10}\nu T = -5$ corresponds to ν=0.32 MHz. 55

Figure 3.24. Required OSNR at BER=10^{-3} versus launch power for 32 Gbaud PM-QPSK system. With 12×80 km SSMF transmission, νT=1.25×10^{-4}. 55

Figure 3.25. Required OSNR at BER=10^{-3} versus launch power for 32 Gbaud DP-QPSK system. With 12×80 km SSMF transmission, νT=1.56×10^{-5}. 56

Figure 3.26. Required OSNR at BER=10^{-3} versus different spans of 80 km SSMF transmission for 32 Gbaud PM-QPSK system. LO=4 MHz, launch power=-1 dBm..... 57

Figure 4.1. Super-channel system design and conventional coherent receiver structure. 60

Figure 4.2. Proposed super-receiver structure with synchronized sampling. 61

Figure 4.3. Primary elements of the superchannel WDM system with joint DSP..... 63

Figure 4.4. Phase of CD compensator for independent subchannel and joint multiple subchannels. 64

Figure 4.5. Demonstration of side subchannel's frequency shifts. 65

Figure 4.6. OSNR gain with ICI equalization at different time delays for 3×28 Gbaud PM-QPSK system [102]. 66

Figure 4.7. Phase of the cross-product spectra in the center subchannel band before and after removing the time delay 67

Figure 4.8. TDE-ICI equalizer OSNR gain at different relative frequency offset for 3×28 Gbaud PM-QPSK system [102]..... 68

Figure 4.9. MIMO linear ICI equalization for the center subchannel. 70

Figure 4.10. NRZ-QPSK signal spectrum before filtering (0.1 nm resolution) and the optical filter spectrum at different bandwidths [101]. 71

Figure 4.11. Required OSNR at BER 3×10^{-3} versus electrical and optical bandwidths. Receiver based DSP includes a 15-tap ISI equalizer (channel spacing=baud rate=28 GHz) [101]..... 72

Figure 4.12. Required OSNR to achieve a BER of 3×10^{-3} at different optical filter bandwidths for system without ICI and ISI equalization and with LMS-ISI or LMS-ICI compensation techniques (channel spacing=baud rate) [101]. 74

Figure 4.13. BER versus OSNR without ICI and ISI equalization and with LMS-ISI or LMS-ICI at optimal optical filter bandwidth (channel spacing=baud rate). Single channel reference is obtained with the LMS-ISI equalization [101]..... 74

Figure 4.14. Required OSNR to achieve a BER of 3×10^{-3} at different optical filter bandwidths for system without ICI and ISI equalization and with LMS-ISI or MAP-ICI compensation techniques (channel spacing=baud rate) [101]. 77

Figure 4.15. BER versus OSNR without ICI and ISI equalization and with LMS-ISI or MAP-ICI at optimal optical filter bandwidth (channel spacing=baud rate). Single channel reference is obtained with the LMS-ISI equalization [101]..... 78

Figure 4.16. Required OSNR to achieve a BER of 3×10^{-3} system without ICI and ISI equalization and with different types of compensation techniques after different transmission distance (channel spacing=baud rate) [101]. 78

Figure 4.17. Frequency domain adaptive equalization block diagram (highlighted block is for side subchannels)..... 82

Figure 4.18.Required OSNR at BER=10^{-3} versus channel spacing with TDE/FDE for ISI or ICI cancellation (Optical filter bandwith is 37.5 GHz). 83

Figure 4.19. Required OSNR at BER=10^{-3} versus optical filter bandwidth with TDE or FDE for ISI or ICI cancellation (Channel spacing is 28 GHz). 84

Figure 4.20. Required OSNR at BER=10^{-3} versus launch power with TDE/FDE for ISI or ICI cancellation (optical filter bandwidth is 31.25 GHz and channel spacing is 28 GHz). 84

Figure 4.21. Generation of the phase locked sub-carriers based on Bessel expansion..... 86

Figure 4.22. Joint Viterbi-Viterbi carrier phase recovery block diagram. 87

Figure 4.23. a) BER versus OSNR with and without joint carrier phase recovery at different channel spacing. b) BER versus OSNR with and without joint carrier phase recovery at 31.25 GHz channel spacing after 8×80 km fiber propagation. 89

Figure 5.1. Rsoft simulation configuration for transmission system with in-band crosstalk addition. 97

Figure 5.2. Crosstalk shaping filters, transmission signal PSDs and crosstalk PSDs..... 97

Figure 5.3. PM-QPSK received constellation in the absence of ASE noise under the impairments of in-band crosstalk φ_{XTw}=-13 dB: a) type 1 crosstalk, b) type 5 crosstalk; Histogram of the received signal points about their statistical average: c) type 1 crosstalk, d) type 5 crosstalk. 98

Figure 5.4. OSNR penalty versus a) crosstalk and b) weighted crosstalk at BER=3×10^{-3} for five types of crosstalk shapes of back-to-back transmission systems. 99

Figure 5.5. BER versus $OSNR_{ASE,dB}$ for back-to-back 112 bits/s PM-QPSK transmission with and without crosstalk impairments and the theoretical performance curve (dashed line). 101

Figure 5.6. Calculated weighting factor η versus $OSNR_{ASE,dB}$ for back-to-back transmission with crosstalk impairments and the theoretical predicted η=0.41 (dashed line). 103

Figure 5.7. a) PM-QPSK transmission signal PSDs with Nyquist pulse shaping (rolloff is 0.1) at 16 Gbaud, 28 Gbaud and 32 Gbaud. The dashed line is the crosstalk PSD. b) Calculated η for systems with Nyquist signaling. Crosstalk powers vary from -19 dB to -13 dB. Dashed lines are the theoretical η. 104

Figure 5.8. Predicted and measured OSNR penalty versus weighted crosstalk for five types of crosstalk shapes for back-to-back transmission. 105

Figure 5.9. Predicted and measured OSNR penalty versus weighted crosstalk for five types of crosstalk shapes in linear regime 14×90 km SSMF transmission (Pch=-4 dBm). 106

Figure 5.10. Predicted and measured OSNR penalty versus weighted crosstalk for five types of crosstalk shapes for nonlinear regime 14×90 km SSMF transmission (Pch=5 dBm). 108

Figure 5.11. Transmission signal PSD: $S(f)$, Crosstalk PSDs $X(f)$, transmission nonlinear PSDs with and without crosstalk addition: $G_S(f)$ and $G_{SX}(f)$. crosstalk induced nonlinear PSDs $G_X(f)$ (weighted crossalk is -13 dB, 14×90 km SSMF fiber transmission, Pch=5 dBm). 109

Figure 5.12. a) Nonlinear crosstalk versus linear weighted crosstalk, b) Nonlinear weighted crosstalk versus linear weighted crosstalk for five crosstalk types after span transmission (Pch=5 dBm). 110

Figure 5.13. Experimental setup for PM-QPSK with crosstalk addition. 111

Figure 5.14. OSNR penalty versus a) crosstalk, b) weighted crosstalk (Pch=-1 dBm), c) crosstalk, d) weighted crosstalk (Pch=3 dBm) [110]. 111

Figure 5.15. BER versus OSNR for system with and without crosstalk impairments in back-to-back, linear, and nonlinear regimes (type 1 crosstalk, weighted crosstalk is -15 dB)..... 112

Figure 5.16. PSDs of primary transmission signal and crosstalk. 113

Figure 5.17. Measured colored-to-white noise weighting factor for weighted crosstalk between -21 dB to -12 dB (different data marks) for each of the crosstalk PSDs of Figure 5.16. The dashed line represents the theoretical expectation. 114

Figure 5.18. OSNR penalty versus a) crosstalk, b) weighted crosstalk for six types of crosstalk shapes in back-to-back 31.5 Gbaud PM-QPSK transmission systems (BER=10^{-3}). Dashed line: GN model predicted performance. 115

Figure 5.19**.** BER versus OSNR at different crosstalk PDL value for type 1 crosstalk of weighted crosstalk power -17.7 dB..... 116

LIST OF SYMBOLS AND ABBREVIATIONS

IP	Internet Protocol
DWDM	Dense Wavelength Division Multiplexing
CD	Chromatic Dispersion
PMD	Polarization Mode Dispersion
PM	Polarization Division Multiplexing
DSP	Digital Signal Processing
QPSK	Quadrature Phase Shift Keying
OOK	On-Off Keying
SDM	Spatial Division Multiplexing
MCF	Multi-core Fiber
QAM	Quadrature Amplitude Modulation
ROADM	Reconfigurable Add/Drop Multiplexor
TDM	Time Division Multiplexing
O/E	Optical-to-Electrical
E/O	Electrical-to-Optical
ADC	Analog to Digital Converter
OSNR	Optical Signal to Noise Ratio
BPSK	Binary Phase Shift Keying
CO-OFDM	Coherent Orthogonal Frequency Division Multiplexing
Nyquist-WDM	Nyquist Wavelength Division Multiplexing
ISI	Inter-symbol Interference
ICI	Inter-channel Interference

NRZ	Non Return to Zero
RC	Raised Cosine
RRC	Root Raised Cosine
CMOS	Complementary Metal–Oxide–Semiconductor
DAC	Digital to Analog Converter
MAP	Maximum A Posterior
MLSE	Maximum Likelihood Sequence Detection
GN	Gaussian Noise
DUM	Dispersion Unmanaged Link
ASE	Amplified Spontaneous Emission
PSD	Power Spectral Density
RZ	Return to Zero
ENOB	Effective Number of Bits
MZM	Mach-Zehnder Modulator
MZI	Mach-Zehnder Interferometer
EDFA	Erbium Doped Fiber Amplifier
DCF	Dispersion Compensation Fiber
PDL	Polarization Dependent Loss
DGD	Differential Group Delay
SPM	Self Phase Modulation
XPM	Cross Phase Modulation
FWM	Four Wave Mixing
PBS	Polarization Beam Splitter
LO	Local Oscillator
CMA	Constant Modulus Algorithm

MIMO	Multiple-In Multiple-Out
DD-LMS	Decision Directed Least Mean Square
BER	Bit-Error Rate
SSMF	Standard Single Mode Fiber
ICA	Independent Component Analysis
PRBS	Pseudo-Random Bit Sequence
EEPN	Equalizer Enhanced Phase Noise
IFFT	Inverse Fast Fourier Transform
FFT	Fast Fourier Transform
FDE	Frequency Domain Equalizer
TDE	Time Domain Equalizer
NLI	Nonlinear Interference
DM	dispersion Managed
NLSE	Nonlinear Schrodinger Equation
RMS	Root Mean Square

SUMMARY

The Nyquist WDM system realizes a terabit high spectral efficiency transmission system by allocating several subcarriers close to or equal to the baud rate. This system achieves optimal performance by maintaining both temporal and spectral orthogonality. However, ISI and ICI effects are inevitable in practical Nyquist WDM implementations due to the imperfect channel response and tight channel spacing and may cause significant performance degradations. Our primary research goals are to combat the ISI effects via the transmitter digital pre-shaping and to remove the ICI impairments at the receiver using MIMO signal processing.

First we propose two novel blind channel estimation techniques that enable the transmitter pre-shaping design for the ISI effects mitigation. Both numerical and experimental results demonstrate that the two methods are very effective in compensating the narrow band filtering and are very robust to channel estimation noise. Besides pre-shaping, the DAC-enabled transmitter chromatic dispersion compensation is also demonstrated in a system with high LO laser linewidth.

Next a novel "super-receiver" structure is proposed, where different subchannels are synchronously sampled, and the baseband signals from three adjacent subchannels are processed jointly to remove ICI penalty. Three different ICI compensation methods are introduced and their performances compared. The important pre-processes that enable a successful ICI compensation are also elaborated. Despite ICI compensation, the joint carrier phase recovery based on the Viterbi-Viterbi algorithm is also studied in the carrier phase locked systems.

In-band crosstalk arises from the imperfect switch elements in the add-drop process of ROADM-enabled DWDM systems and may cause significant performance degradation. Our third research topic is to demonstrate a systematic way to analyze and predict the in-band crosstalk-induced penalty. In this work, we propose a novel crosstalk-to-ASE noise weighting factor that can be combined with the weighted crosstalk weighting metric to incorporate the in-band crosstalk noise into the Gaussian noise model for performance prediction and analysis. With the aid of the Gaussian noise model, the in-band crosstalk-induced nonlinear noise is also studied. Both simulations and experiments are used to validate the proposed methods.

CHAPTER 1

INTRODUCTION

In recent years, there is an increasing demand in data traffic for high-speed internet, data centers and internet video services applications. According to Cisco's analysis, the Internet Protocol (IP) traffic will grow at a compound annual growth rate of 21% from 2013 to 2018 [1]. As illustrated in Figure 1.1, the global IP traffic reached 51.2 Exabyte per month in 2013 and will increase nearly three folds to 131.6 Exabyte by 2018 [1]. The expansion of the data traffic motivates the development in fiber optical communications.

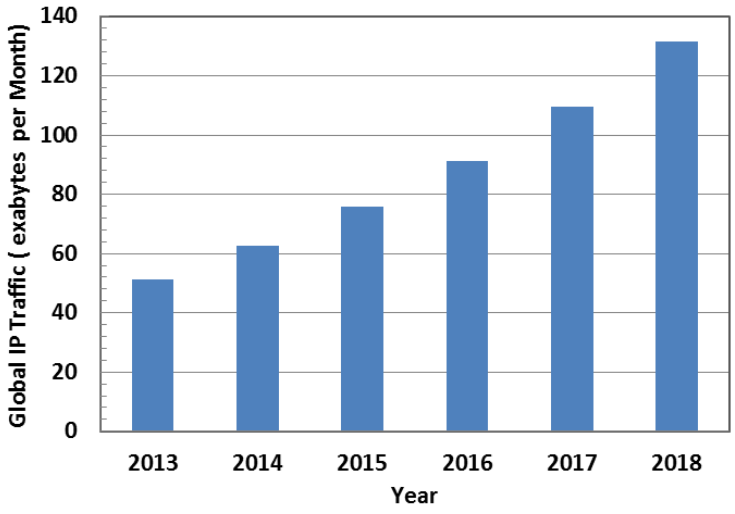

Figure 1.1. Global IP traffic growth from 2013 to 2018.

Fiber optic communication has been increasingly used for high data rate and high capacity long distance transmission. Compared to the electrical cables, significant advantages have been demonstrated for optical fibers in terms of the reach and

transmission capabilities. Specifically, the fiber loss in the commonly used C bands in single mode fibers is about 0.2 dB/km [2]. In comparison, the loss of the common RG-6 coaxial cable is above 200 dB/km at 1000 MHz. Meanwhile, optical fibers are immune to various kinds of electromagnetic interference and are more suitable for data links in industrial environments. Because of the optical fiber's ability to support long reach and high speed transmission, they have replaced copper wires in all the core and metro networks.

The major research in optical communication society is to increase the channel capacity while retaining a maximal system performance. The earlier capacity growth was realized mostly by increasing the intensity modulation rate and the use of dense wavelength division multiplexing (DWDM) techniques [2]. However, because of electronic devices' limitations and their inability to compensate channel impairments in a direct detection scheme, the intensity modulation rate can hardly be boosted beyond 10 Gb/s [3]. For a fixed number of channels, the achievable capacity is limited. Coherent detection employs a hybrid receiver structure to retrieve the phase of the electrical field. With the knowledge of the phase information, channel impairments like chromatic dispersion (CD) [4], polarization mode dispersion (PMD) [5], or Kerr nonlinear effects can be compensated [6-8]. Therefore, polarization division multiplexing (PM) schemes and more advanced modulation formats become feasible, enabling a channel capacity increase and channel speed upgrading to 100 Gb/s and beyond.

The advent of coherent detection and advanced digital signal processing (DSP) has driven the rapid growth in high speed and high capacity optical transmission. In recent years, optical transport industries have commercialized the 100 Gb/s transponders

using a single optical carrier in the single mode fiber. Owing to the coherent detection techniques the 100 Gb/s module supports a more complicated format, quadrature phase shift keying (QPSK) instead of the conventional intensity modulated on-off keying (OOK) [9]. The PM scheme is also deployed, which doubles the spectral efficiency by transmitting data in orthogonal polarizations. These successes in the 100 Gb/s research laid a solid foundation for the future terabit link development, which will soon be required to meet the increasing traffic demand. Some of the on-going researches are exemplified in Figure 1.2.

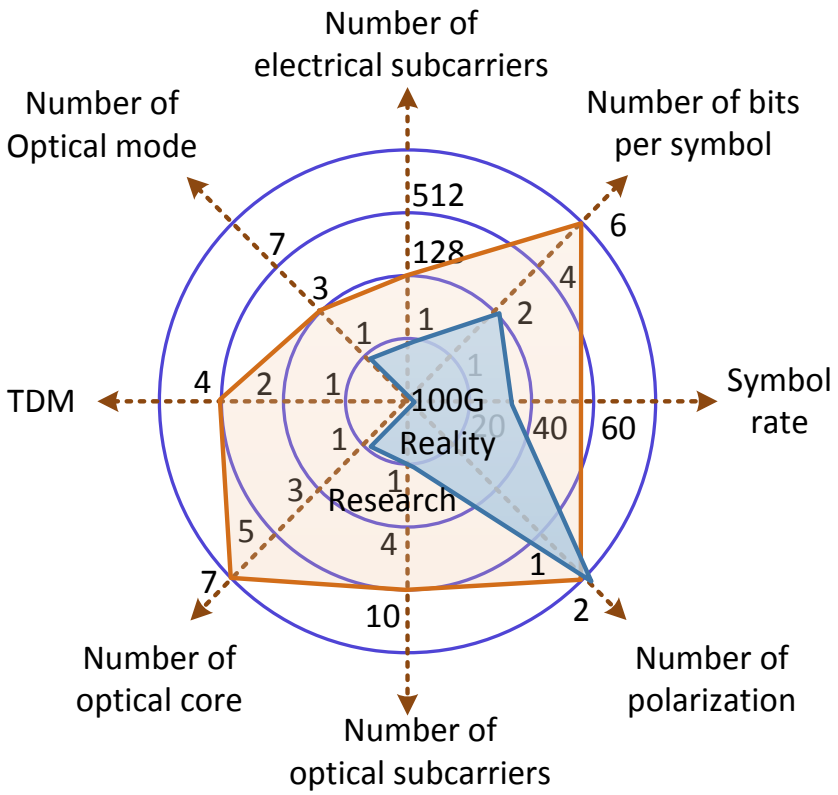

Figure 1.2. Current 100 Gb/s system design and research trend in transmission beyond 100 Gb/s.

Multi-core and multi-mode are the two fiber configurations that enable spatial division multiplexing (SDM) in optical communications [10]. The multi-mode fiber has a core diameter larger than the single mode fiber, allowing the propagation of multiple modes simultaneously [2]. Because of mode coupling in long distance transmission, the core size is usually confined to support few modes transmission, for example, six spatial and polarized modes transmission are demonstrated in reference [11]. The transmission paths of multi-core fiber (MCF) are several distinct arrays of single mode fiber cores [12]. Because of the fiber reliability, the MCF diameter is restricted to 200 μm and most MCF has a hexagonal arrange of seven-cores [12]. Recent work has demonstrated a ~52 km PM-32ary quadrature amplitude modulation (QAM) transmission over the ring geometry structured 12-cores MCF, reaching a 1.01 Pb/s capacity [13]. SDM can increase the channel capacity by using multiple cores or modes. However, the amplifiers, the reconfigurable optical add-drop multiplexers (ROADM), and the receivers are required to be reconfigured to support the SDM structure. Thereafter, many challenges from the component to system level are to be overcome before the new fibers can be deployed in the field [10].

Time domain division multiplexing (TDM) increases the transmission speed by time-multiplexing several lower bit-rate streams [14]. Electrical TDM multiplexes the signal electrically and then converts it into optical signals, thus requiring large electrical bandwidth in the optical-to-electrical (O/E) and electrical-to-optical (E/O) interfaces at high baud rate [15]. Optical TDM multiplexes the signal optically. Therefore, the system' electrical bandwidth requirement is relaxed and is related to the baud rate of each subcarrier [14]. However, the CD and PMD compensation have to be performed optically, such that the residual pulse spreading is within the symbol period for accurate individual subchannel demultiplexing [16, 17]. Because of the hardware constraint and the system stability, TDM is challenging to be used for the terabit per channel system design.

Achieving terabit transmission using a single wavelength by increasing the symbol rate or the modulation format is difficult to realize. To date, a single carrier 107 Gbaud PM-QPSK signal generated with electrical TDM has been demonstrated, but the research relies on very high speed analog-to-digital converters (ADCs), followed by off-line DSP [15]. Higher order modulation formats like PM 64-QAM have gained a lot of interest recently [18], nonetheless the reach is limited because of the need for high optical signal to noise ratio (OSNR), high receiver sensitivity, and linearity. Thereafter, the most reliable way to design the upcoming terabit optical link lies in the joint optimization of three dimensions: symbol rates, modulation formats, and subcarriers. To address this problem, the super-channel concept has been brought up, where multiple optical subcarriers are tightly spaced to increase the channel capacity and each wavelength operates at the maximum data rate permitted by commercially available ADC components [19]. Modulation formats, such as binary phase shift keying (BPSK), QPSK, or 16-QAM, can be chosen to balance the reach and spectral efficiency.

1.1 Terabit Super-channel System

The terabit super-channel attempts to achieve high spectral efficiency by using maximally dense channel spectra while retaining both spectral and temporal orthogonality, as shown in Figure 1.3. Two related schemes are coherent optical orthogonal frequency-division multiplexing (CO-OFDM) [20-24] and Nyquist-wavelength division multiplexing (Nyquist-WDM) [20, 25-28]. In the CO-OFDM system, frequency domain *sinc-like* subcarriers are spaced exactly at the baud rate to obtain high spectral efficiency and the symbol transitions are time-aligned for all the carriers [22]. Ideally, this achieves both inter-channel interference (ICI) and inter-symbol

interference (ISI) free operation if proper filtering and sampling is performed [20]. Nonetheless, the realization is challenging because of the stringent requirement of perfect rectangular temporal pulse shaping and large receiver bandwidth with fast ADCs [27]. If the OFDM signals are generated electrically, extreme high electrical bandwidth is required to achieve an overall terabit transmission. An alternative super-channel scheme, Nyquist-WDM, requires *sinc*-shaped time domain pulse and thus an ideal rectangular shaped spectrum with a bandwidth equal to the baud rate [25]. Since the spectra of the subchannels are not overlapped, the ICI effects can be avoided. Furthermore, when sampling at zero-crossing points of the Nyquist pulses, the system is ISI free. Compared with CO-OFDM, the Nyquist-WDM system relaxes the bandwidth requirement of the receiver, and exhibits better nonlinearity tolerance because of the smaller spectral overlap [20]. Thereafter, Nyquist system is a preferred design scheme of the super-channel system and is our primary research topic.

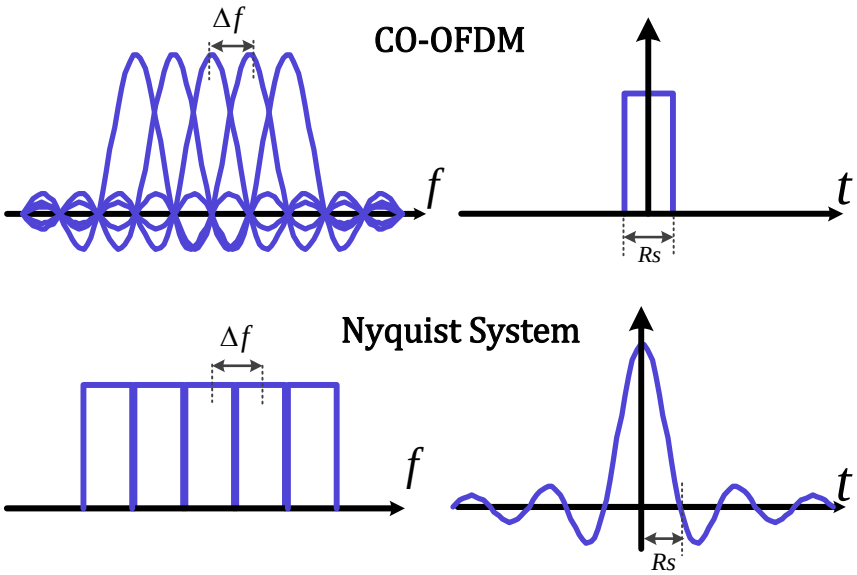

Figure 1.3. Spectra and temporal pulses for CO-OFDM and Nyquist-WDM systems.

In real Nyquist-WDM systems, delivering a perfect rectangular spectrum, with flat phase, to the receiver is difficult because of signal generation imperfections and the impact of cascaded filters in the transmission system. Thereafter, practical systems are not ideal Nyquist, although it is common to refer to them as Nyquist-WDM systems. First of all, the channel spacing is not restricted to the baud rate for balancing the requirement of channel spectral efficiency and system performance [29, 30]. Second, the practical transmitter pulses are usually not perfect temporal *sinc*-shaped thus inducing non-rectangular transmitter spectra. For example, Super Gaussian optical filters are used to shape the conventional non-return-to-zero (NRZ) waveforms. The goal is to suppress ICI effects as much as possible, rather than creating perfect temporal orthogonal transmitter pulses. An alternative design is to use the raised cosine (RC) or root raised cosine (RRC) shaped Nyquist pulses [31, 32]. These Nyquist pulses maintain orthogonal temporal shapes while controlling the spectral spreading via the roll-off factor. They are easier to generate and retain than the perfect *sinc* pulses. The frequency domain representation of an RC pulse is in Eq. 1.1 [32]

$$H_{TX,RC}(f) = \begin{cases} T, & |f| < \frac{1-\beta}{2T} \\ \frac{T}{2}\left\{1 + cos\left[\frac{\pi T}{\beta}\left(|f| - \frac{1-\beta}{2T}\right)\right]\right\}, & \frac{1-\beta}{2T} \le |f| \le \frac{1+\beta}{2T} \\ 0, & otherwise \end{cases} \quad (1.1)$$

T is the symbol period of the signal and β ($\beta \in [0,1]$) is the roll-off factor that controls the spectrum occupation bandwidth. Assuming channel filter bandwidth is much larger than the signal bandwidth such that there is no ISI, the samples of the received waveform at T is not interfering with the adjacent symbols. However, when RC spectra are used at the transmitter and a matched filter is used at the receiver, the overall system response is not RC and might cause the received signals lose orthogonality. Therefore, in practical communication systems, RRC shape is usually used. The frequency domain

representation of RRC is in Eq. 1.2. To maintain an overall RC response, the receiver matched filter $H_{RX,RRC}$ is also RRC shaped and resembles the transmitter pulse shaping.

$$H_{TX,RRC} = \sqrt{H(f)} = H_{RX,RRC} \tag{1.2}$$

Figure 1.4 exemplifies the RC and RRC shaped spectra at different roll-offs. As β approaches zero, the spectrum is more rectangular-like. Although RRC is preferred over RC in terms of maximizing SNR when a matched filter is used, the spectral tail is larger than RC at the same roll-off, potentially causing more ICI at tight channel spacing.

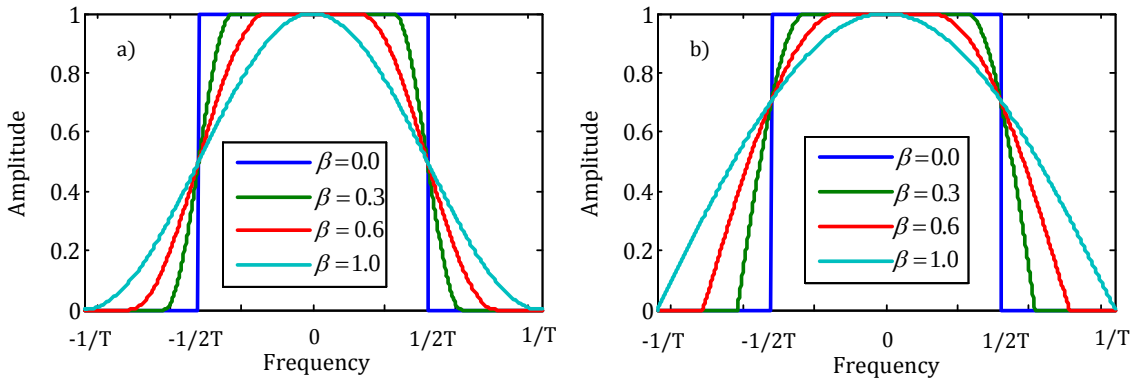

Figure 1.4. Spectra of a) RC, b) RRC at different roll-offs.

The Nyquist pulse generation can be performed optically using a wave-shaper. However, because the optical wave-shaper delivers spectral resolution of about 1 GHz or higher, spectra with sharp roll-off are hard to achieve, inducing ICI penalties at tight channel spacing [31]. With advances in complementary metal-oxide-semiconductor (CMOS) and DSP techniques, high speed digital-to-analog converters (DACs) enable a flexible high speed transmitter side signal processing. Compared to the optical wave-shaper, DAC delivers Nyquist pulses with a finer resolution and can generate near

rectangular spectra [31-34]. Nonetheless, ISI impairment is still important because of the DAC bandwidth limitation, the imperfect gain profile of the driver, and any other filter effects from the channel and the receiver.

Based on the previous discussion, ISI and ICI are two important impairments in a super-channel system. Our primary research topics are to explore different compensation techniques that deal with the two effects.

1.1.1 Inter-symbol Interference Effect

The ISI effect results in the loss of orthogonality between the time domain Nyquist pulses because of the narrow band filtering effects mainly coming from the limitations of the pulse generator, optical modulator, and the coherent receiver. The filtering effects of the switch elements of the ROAMs typically only impact the side subchannels, since the entire super-channel is routed as a combined group and no multiplexing filter is applied to each subchannel. Several ISI compensation methods are available. Receiver equalization may compensate the ISI effects by adaptively tracking the inverse channel response. However, because the performances of the DSP modules before equalization are significantly affected by the residual ISI, and the high frequency bands of the noise spectra are significantly enhanced during equalization, the receiver equalizer performance is limited. Advanced algorithms based on the maximum likelihood sequence detection (MLSE) [35] or maximum a posterior (MAP) have demonstrated better ISI compensation ability, but the receiver complexity is increased [36]. The high speed DAC together with a modern DSP capability provides a reconfigurable and flexible waveform optimization capability that enables the transmitter DSP. The transmitter ISI compensation has demonstrated its efficiency to combat ISI without introducing

significant complexity [37]. Pre-shaping the signal before transmission requires the knowledge of the channel response; nominally the filter shapes of the cascading optical and electrical elements. A frequency domain channel estimation method has been proposed that first transmits a known training sequence [38]. The ratio between the Fourier transform of the transmitted and received baseband signals is an estimate of the frequency domain transfer function and is used for pre-shaping. The major challenge is that a large number of measurements are required to retrieve an estimate sufficiently free of noise [38]. Although full demodulation of the training sequence is not required, exact symbol information needs to be known at the receiver.

1.1.2 Inter-channel Interference Effect

The other important penalty is the ICI effect. In Nyquist systems, subcarriers are closely spaced to maximize the channel capacity. However, significant performance penalties have been observed at tight channel spacing [32], which motivates further efforts to compensate ICI. Conventional ICI mitigation methods for Nyquist-WDM systems use strong optical or electrical filtering to suppress the crosstalk, yet this also requires additional DSP to compensate the associated narrow filtering impairments [36]. Another approach is to use prefiltering (predistortion) to emphasize the high frequency components of the transmitting signal, so that cascaded filtering effects are compensated and the overall received spectrum is closer to the desired rectangular spectrum [20, 25]. Nevertheless, the performance improvement is limited at narrow channel spacing.

1.2 In-band Crosstalk Analysis

In ROADM-enabled dense wavelength division multiplexing (DWDM) systems, the optical switch can be set either to drop certain wavelengths at one ROADM,

forwarding the rest of the wavelengths to the next ROADM, or to add wavelength at certain ROADM before sending them off to the next ROADM. Because of the finite isolation and imperfect filter shapes of the switching elements, crosstalk arises during the add-dropping process and is accumulated at each successive add/drop node [39-42]. Thereafter, the in-band crosstalk has diverse spectral contents determined by the specific link configurations and is generally dissimilar to the primary transmission signals. As crosstalk is one of the most significant impairments in DWDM system, it is desirable to incorporate the crosstalk noise into the Gaussian noise (GN) model for performance prediction and analysis.

The GN model is used to assess fiber nonlinearity in dispersion unmanaged links (DUM) [43-45]. It has been found that after short dispersion, the nonlinear noise is statically Gaussian distributed and is added up in power with the amplified spontaneous emission (ASE) noise to generalize the conventional OSNR for performance predictions [44, 46, 47]. The GN model also demonstrates that the received signals under the linear impairments of ICI and ISI are also Gaussian-*like* [46]. The linear noise can be quantified by investigating the back-to-back transmission system sensitivity, and then combined with the ASE noise and nonlinear noise for performance assessment [46]. Therefore, crosstalk noise can also be added into the GN model for performance prediction in a similar manner.

Previously a spectral weighting method was shown to account for the colored noise characteristics of ROADM-induced crosstalk and was used to accurately assess penalties for a wide range of crosstalk spectra for linear link configurations in QPSK and DPSK systems [40, 41]. With this approach, the crosstalk with the same weighted

crosstalk power incurs the same penalty, regardless of the crosstalk shapes. However, the weighted crosstalk power cannot be directly used in the GN model for performance predictions because it is not quantitatively equivalent to ASE noise. Meanwhile, the spectral weighting metric is validated only in the linear transportation regime and as most links operate in the nonlinear regime the crosstalk penalties may not simply follow the design rules of the linear regime. It is desirable to devise and validate design rules for systems with both channel nonlinearity and crosstalk impairments.

1.3 Objectives

The objectives of my research focus on three aspects. Frist, we investigate the pre-shaper design to compensate channel ISI impairments for systems with Nyquist signaling. Two pre-compensation algorithms based on the receiver adaptive equalizer and receiver signal power spectral density (PSD) extraction will be introduced. Meanwhile, the DAC enabled transmitter CD compensation is studied.

The second objective is to investigate the receiver ICI compensation in the terabit super-channel system. A novel super-receiver structure will be proposed, where subchannels undergo synchronized sampling, enabling joint signal processing at the receiver. Three different ICI mitigation methods will be demonstrated and validated in PM-QPSK Nyquist-WDM systems. The performance and complexity of those ICI compensators will be investigated. The joint carrier phase recovery is also discussed.

The third objective is to use the GN model to investigate the in-band crosstalk penalty in ROADM-enabled DWDM system. A crosstalk to ASE noise weighting factor is proposed and is combined with the in-band crosstalk weighting metric to treat the weighted crosstalk quantitatively as ASE noise for performance prediction. The crosstalk

induced nonlinearity will be investigated using the GN model and will be quantitatively compared with its corresponding linear crosstalk noise.

The outlines of the dissertation are organized as following. Chapter 2 introduces the basic structures of an optical communication system, primary the transmitter signal generation, the transmission channel impairments, and the coherent receiver design. The coherent receiver demodulation techniques are also summarized. Chapter 3 focuses on discussing two novel blind channel estimation techniques for transmitter pre-shaping. The performances of the two pre-shapers are compared and the noise impacts on channel estimation are also investigated. Both simulations and experiments are performed to validate the proposed algorithms. A transmitter CD pre-compensation is discussed. Chapter 4 introduces receiver ICI compensation in the Nyquist WDM system. A novel super-receiver structure is proposed to enable a joint ICI cancellation using the information from adjacent subchannels. The pre-required techniques that enable a successful ICI compensation are introduced, and different ICI compensation methods are discussed. A joint carrier recovery is also presented for systems deploying carrier phase locked lasers. Chapter 5 gives an overview of the transmission impairments induced by the add-drop nodes in WDM networks. GN model is used to analyze and predict the in-band crosstalk induced linear and nonlinear penalties. Chapter 6 provides a summary of the main results of this work and discusses potential research topics.

CHAPTER 2

FIBER OPTICAL COMMUNICATION SYSTEM DESIGN

The primary construction of an optical fiber communication system resembles other communication systems. It composes of a modulator which modulates the electrical waveforms onto the optical carrier (lasers); the transmission channel that conveys the optical signal; a receiver that extracts information from the optical signals and compensates the transmission penalties. In this chapter, we give an overview of the optical system design and the major channel impairments in a single mode fiber system.

2.1 Optical Signal Generations

The simplest optical signal is the intensity modulated OOK, which may take two modulation formats: NRZ and return-to-zero (RZ). NRZ modulation has been widely used in many transmission systems because of its ease of generation and its low occupation bandwidth [48]. On the other hand, RZ modulation is used because it is less susceptible to ISI and is more tolerated to fiber nonlinearity [48, 49]. However, as conventional electrical source usually delivers NRZ pulses, the creation of RZ format requires an additional pulse carving stage with the pulse duty cycles controlled by the frequency of the sinusoidal driving wave and the bias voltage [48, 50-52]. Extensive studies of RZ formats have been carried out in direct detection 10 Gbit/s and 40 Gbit/s transmission links [53, 54] and the same RZ carving techniques are applicable to coherent detection systems [41, 55].

Additional electrical sources, electrical delay, and extra modulation stages are needed to generate higher order modulation formats using the conventional non-

programmable transmitter [56-58]. The high speed DAC offers a flexible way to deliver signals with various modulation formats and pulse shapes [34, 37, 59-61] by digitally creating arbitrary waveforms offline. The baseband digital signal generation usually follows subsequent orders; symbol mapping for given transmission bits, pulse shaping, resampling to deliver the desired baud rates, and finally quantization. The resampling and quantization is performed according to the DAC intrinsic characteristics. For example, to deliver 32 Gbaud waveforms of DACs with a fixed operation rate of 64 samples/s, the oversampling rate is two; For a DAC with effective number of bits (ENOB) of eight, the digital signals are quantized to fall in between -128 and 127. The current generation of DACs usually has a tight electrical bandwidth which is one of the primary ISI sources.

RF amplifiers are paired with the RF sources to boost the power levels of the electrical signals before forwarding them to the modulator. Two main characteristics of the RF amplifiers are the frequency response and the nonlinearity. The amplifier nonlinearity can be modeled by a second order and third order harmonic process [62]. Numerical simulations reveal that even small nonlinear coefficients may cause noticeable OSNR penalties and constellation distortions in systems with high order modulation formats [62]. After amplification, the RF signals are used to drive the modulator.

The configuration of a commonly used IQ modulator includes two-parallel Lithium Niobate ($LiNiO_3$) Mach-Zehnder modulators (MZM) nested in MZ interferometer (MZI) with a single MZM transfer function represented by [63, 64]

$$E_{out} = E_{in} \cos\left(\frac{\pi V_{in}}{V_{\pi}}\right) \tag{2.1}$$

where V_{in} is the driving voltage and E_{in} (E_{out}) is the input (output) field of the optical signals. V_{π} is the half-wave voltage of the modulator. The two sub-MZMs (MZMa and

MZMb) are used to create the in-phase and quadrature optical signals and the third component (MZIc) is used to introduce a 90 degree phase shift between the in-phase and quadrature components [65], as illustrated in Figure 2.1.

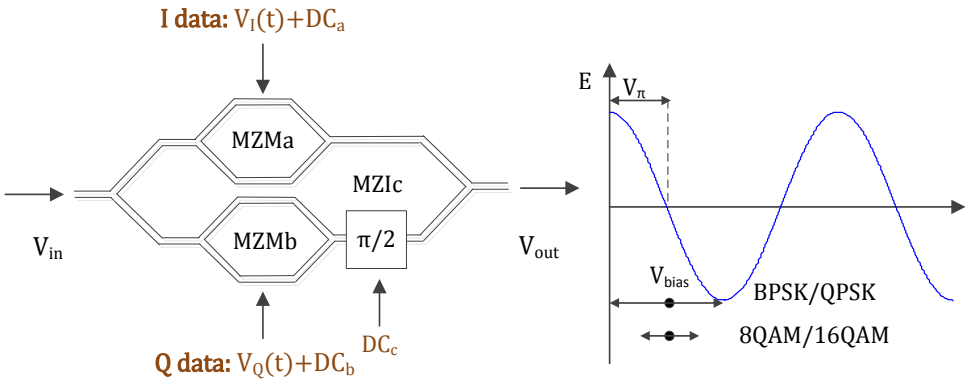

Figure 2.1. IQ MZM structure with the transfer function.

The driving signals of the two MZMs include a modulation voltage (RF voltage) and a DC voltage (bias voltage). The RF voltage controls the output signals modulation and the bias voltage selects the operation point of the modulator and tracks possible modulator drifts caused by thermal changes, static electrical charge accumulation, and imbalance of the MZMs. The optimal bias voltage may be manually located according to the transmission signal quality or may be automatically tracked by a bias control device [66]. Because the transfer function of MZMs is nonlinear; the swing of the RF driving signal becomes important for higher order constellations. For QPSK signals, the modulator is biased at null and is driven at $2V_\pi$ to maximize the extinction ratio of the output eye diagram. For high order modulation formats, unless the modulator

nonlinearity is pre-compensated [60], it is preferred to drive the signal in the linear regime, around $1.5V_{\pi}$.

After modulation, the optical signals are amplified before transmission to ensure a sufficiently high OSNR upon receiving. Two commonly used optical amplifiers are the erbium doped fiber amplifiers (EDFAs) and the Raman amplifiers. Typical EDFA uses pump lasers at a wavelength of 980 nm or 1480 nm to produce gains in the C-band and a gain equalizer is used to flat the gain spectrum at different wavelengths [67]. EDFA may also be designed to enable transmission in the L-band [67, 68]. However, the EDFA configuration in this regime requires high pump powers and the noise figure is larger [2]. The Raman amplifier provides gains at a wavelength centered about 100 nm higher than the pump wavelength [2]. It is able to deliver gains at different wavelengths and thus makes it feasible to extend current optical transmission bands. Nowadays, the most popular use of the Raman amplifier is to complete EDFAs by providing additional gain in a distributed manner in ultra-long haul systems [2].

2.2 Transmission Channel Impairments

The transmission capacities in optical communication systems are constrained by a number of factors that come from various system components. For example, the finite transmission bandwidths caused by the transmitter DAC, the driver, the modulator, and the receiver; nonlinearity from the modulator and the driver; limitations of the receiver sampling speed and etc. Meanwhile, the transmission channel has several linear and nonlinear impairments that degrade the system performance.

Loss in silica fiber is an important mechanism that limits the transmission distance between amplifiers or repeaters. The intrinsic loss arises from the fundamental

material properties of the silica fiber, such as ultraviolet absorption, infrared absorption, and Rayleigh scattering [69]. The intrinsic loss is wavelength dependent and it is about 0.2 dB/km in the vicinity of the C-band. The extrinsic loss may be caused by the metallic and rare earth impurities, the OH, the bending loss, and fiber splicing [69]. The input and output optical power level difference after transmitting through a fiber of loss α and distance L is specified by

$$P_{out} = P_{in} 10^{\frac{-\alpha L}{10}} \tag{2.2}$$

Chromatic dispersion causes pulses spreading and complicates the receiver detection. Dispersion arises because the propagation constant β varies nonlinearly with the frequency. For a given carrier frequency ω_0, β can be approximated by a Taylor series expansion truncated at the third order.

$$\beta(\omega) \approx \beta|_{\omega_0} + (\omega - \omega_0)\frac{d\beta}{d\omega}\Big|_{\omega_0} + \frac{1}{2}(\omega - \omega_0)^2 \frac{d^2\beta}{d^2\omega}\Big|_{\omega_0} + \frac{1}{6}(\omega - \omega_0)^3 \frac{d^3\beta}{d^3\omega}\Big|_{\omega_0}$$

$$= \beta_0 + (\omega - \omega_0)\beta_1 + \frac{1}{2}(\omega - \omega_0)^2\beta_2 + \frac{1}{6}(\omega - \omega_0)^3\beta_3 \tag{2.3}$$

β_2 describes the quadrature dispersion of the fiber and is an important parameter that determines the extent of pulse spreading [69]. The cubic dispersion β_3 is important in cases when there is a frequency exists such that the quadrature dispersion becomes zero; or pulses have a bandwidth that occupies a large portion of the $\beta - \omega$ curve [69].

The dispersion in fiber is usually standardized by the dispersion parameter D which relates the quadrature dispersion β_2 as follows

$$\beta_2 = -\frac{\lambda_0^2}{2\pi c} D(\lambda_0) \tag{2.4}$$

λ_0 is the center wavelength. When considered the third order dispersion, D relates to β_3 as

$$\beta_3 = \frac{\lambda_0^3}{2\pi^2 c^2}\left[D(\lambda_0) + \frac{\lambda_0}{2}\frac{dD}{d\lambda}\Big|_{\lambda_0}\right] \quad (2.5)$$

The first derivative of D is known as the dispersion slope [69].

Chromatic dispersion can be compensated by the dispersion compensation fiber (DCF) with negative dispersion. Denote the transmission and compensation fiber dispersion parameter as D_1 and D_2 and length L_1 and L_2, the relation for dispersion compensation is

$$D_1 L_1 + D_2 L_2 = 0 \quad (2.6)$$

For large bandwidth pulse transmission, for example, the WDM channel, it is also necessary to compensate the dispersion slope

$$L_1 \frac{dD_1}{d\lambda}\Big|_{\lambda_0} + L_2 \frac{dD_2}{d\lambda}\Big|_{\lambda_0} = 0 \quad (2.7)$$

The use of DCF is discouraged because of the extra loss and high nonlinearity in DCF. Other dispersion compensation methods are also available, including the chirped fiber Bragg gratings [70, 71], and the Gires-Tournois interferometers [69]. Dispersion shall be compensated digitally at the receiver, which will be elaborated in the next section.

Polarization dependent loss (PDL) and PMD are the two major polarizations associated linear impairments. PDL arises from the polarization dependent nature of the optical components such as optical amplifiers, attenuators, and filters [49]. It causes inequality between the two polarization tributes and degrades the OSNR. For a fixed PDL value, the system penalty varies dramatically because the orientation of the arrived polarization is arbitrary with respect to the principle axis of the PDL elements [72, 73]

and because of the interaction between PDL and fiber nonlinearity [74]. PMD describes the pulse broadening and distortion caused by the fiber birefringence properties and is the most important polarization dependent penalty in high data rate long haul transmission systems. PMD is characterized by the differential group delay (DGD) between the two principle states of polarization with certain fiber transmission and follows a Maxwell distribution. The PMD induced penalty is more significant for high baud rate signals because the pulse broadening is affecting more symbols, and thus PMD needs to be compensated at the receiver.

Self-phase modulation (SPM), cross-phase modulation (XPM), and four-wave mixing (FWM) are the primary nonlinear effects in optical fibers. The fundamental understanding of those nonlinear effects necessitates the investigation of the wave propagation in a nonlinear transmission medium. For a sourceless and nonmagnetic medium, the wave equation for the real instantaneous electric field in time domain is [69]

$$\nabla^2 \boldsymbol{\mathcal{E}}(\mathbf{r},\mathrm{t}) - \mu_0 \epsilon_0 \frac{\partial^2 \boldsymbol{\mathcal{E}}(\mathbf{r},\mathrm{t})}{\partial t^2} = \mu_0 \frac{\partial^2 \boldsymbol{\mathcal{P}}(\mathbf{r},\mathrm{t})}{\partial t^2} \tag{2.8}$$

Where ϵ_0 is the free space permittivity. $\boldsymbol{\mathcal{P}}(\mathbf{r},\mathrm{t})$ is the macroscopic polarization vector with the power series expanded as

$$\begin{aligned} \boldsymbol{\mathcal{P}}(\mathbf{r},\mathrm{t}) = \epsilon_0 \chi_e \boldsymbol{\mathcal{E}}(\mathbf{r},\mathrm{t}) &= \epsilon_0 \left[\chi^{(1)} \boldsymbol{\mathcal{E}} + \chi^{(2)} \boldsymbol{\mathcal{E}}\boldsymbol{\mathcal{E}} + \chi^{(3)} \boldsymbol{\mathcal{E}}\boldsymbol{\mathcal{E}}\boldsymbol{\mathcal{E}} + \cdots\right] \\ &= \boldsymbol{\mathcal{P}}_L(\mathbf{r},\mathrm{t}) + \boldsymbol{\mathcal{P}}_{NL}(\mathbf{r},\mathrm{t}) \end{aligned} \tag{2.9}$$

where $\chi^{(1)}$ determines the linear part of $\boldsymbol{\mathcal{P}}(\mathbf{r},\mathrm{t})$ and the fourth-rank tensors $\chi^{(3)}$ describes the third-order nonlinear process in optical fibers. $\boldsymbol{\mathcal{E}}$ is the sum of all incident fields and those generated by the nonlinear polarization. The nonlinearity analysis in optical fibers can be carried out by incorporating the nonlinear polarization $\boldsymbol{\mathcal{P}}_{NL}(\mathbf{r},\mathrm{t})$ into the wave equation. Assume propagating in the z direction, Eq. 2.8 becomes

$$\frac{\partial^2 \boldsymbol{\mathcal{E}}(\mathrm{z,t})}{\partial z^2} - \mu_0 n^2 \epsilon_0 \frac{\partial^2 \boldsymbol{\mathcal{E}}(\mathrm{z,t})}{\partial t^2} = \mu_0 \frac{\partial^2 \boldsymbol{\mathcal{P}}_{NL}(\mathrm{z,t})}{\partial t^2} \qquad (2.10)$$

Assume a signal propagates through the fiber along the X-principle axis with the electrical field represented as

$$\boldsymbol{\mathcal{E}}_{in} = \frac{1}{2} E_x e^{-ikz} e^{i\omega t} \hat{x} + c.c. \qquad (2.11)$$

where k is the phase constant and ω is the transmission frequency. At the output of the nonlinear medium, a third harmonic term is generated and the total electrical filed $\boldsymbol{\mathcal{E}}$ becomes

$$\boldsymbol{\mathcal{E}} = \frac{1}{2}\left(E_x e^{-ikz} e^{i\omega t} + E_{\tilde{x}} e^{-ik'z} e^{i3\omega t}\right)\hat{x} + c.c. \qquad (2.12)$$

The nonlinear polarization is computed by $\boldsymbol{\mathcal{P}}_{NL}(z,t) = \epsilon_0 \chi^{(3)} \boldsymbol{\mathcal{E}}^3(z,t)$. For SPM, we only interest in the nonlinearity that is caused by the interaction between input field and itself at frequency ω, therefore the corresponding nonlinear polarization amplitude is

$$P^{\omega}_{NL,x} = \frac{3}{4} \epsilon_0 \chi_{xxxx}(\omega; \omega, -\omega, \omega) |E_x|^2 E_x e^{-ikz} \qquad (2.13)$$

Substitute Eq. 2.11 and 2.13 into the wave equation Eq. 2.10, the refractive index n which relates to the phase constant k ($k = n\omega/c$) is approximated by [69]

$$n \approx n_0 + n_2' |E_x|^2 \qquad (2.14)$$

where n_2' is the nonlinear refractive index defined as

$$n_2' = \frac{3\chi_{xxxx}}{8n_0} \qquad (2.15)$$

Thus, the electrical field contains an additional time-varying phase term that introduces a new frequency component to the original pulse after propagating through the nonlinear medium [69]. The analysis of XPM resembles the SPM examination except that the input pulses have different frequencies or polarizations. The refractive index in the presence of

XPM for waves propagating along the X-polarization at different frequencies is described as follows

$$n = n_0 + 2n_2'|E_{2x}|^2 \tag{2.16}$$

The nonlinear refractive index due to XPM is doubled compared to Eq. 2.14. FWM describes the generation of a fourth frequency tone with the interaction of three fields. The analysis of the FWM can be carried out in a similar manner using the wave equation. SPM may be compensated digitally using back-propagation [75] or Volterra series analysis [6], while the XPM digital compensation requires additional information from adjacent channels [76].

2.3 Coherent Receiver Structures

A simple intensity modulated direct detection system measures the incoming signal intensity using square law direct detection. This type of detection is cost effective and the receiver sensitivity is independent of the carrier phase and the state of polarization. However, as the phase information is not retained, all the channel impairments like CD and PMD have to be compensated before the receiver, limiting the deployment of a variety of spectral efficiency modulation formats. In contrast, coherent detection has a more complicated receiver structure which keeps the amplitude and phase of the optical electric field and the state of the polarization. This information can be used to realize electrical post processing for channel estimation and impairment compensation, which has massive potential to innovate the optical communication society.

Coherent detection is usually implemented in a dual polarized system. An example of the coherent detection scheme corresponding to one of the polarization is demonstrated in Figure 2.2. At first, the incoming optical signals of E_s and LO laser pass through a

polarization beam splitter (PBS) to isolate the signals along the two principle axis. Then the resulting optical signal field (E_{sx}) is mixed with the LO laser (E_{LOx}) using a 3 dB coupler which has a power transmission of ε. The electric fields at the coupler outputs are represented in Eq. 2.17-2.20.

$$E_{x1}(t) = \sqrt{1-\varepsilon}[E_{sx}(t) + N] + \sqrt{\varepsilon}\, E_{LOx} \quad (2.17)$$

$$E_{x2}(t) = -\sqrt{\varepsilon}[E_{sx}(t) + N] + \sqrt{1-\varepsilon} E_{LOx} \quad (2.18)$$

$$E_{x3}(t) = \sqrt{1-\varepsilon}[E_{sx}(t) + N] + i\sqrt{\varepsilon}\, E_{LOx} \quad (2.19)$$

$$E_{x4}(t) = -\sqrt{\varepsilon}[E_{sx}(t) + N] + i\sqrt{1-\varepsilon}\, E_{LOx} \quad (2.20)$$

After the photodetectors, the output electrical signals follow the rule of $S_k(t) = R_k|E_k(t)|^2$, where R_k is the responsivity of each photodetector.

$$S_{x1} = R_1\left[(1-\varepsilon)(|E_{sx}|^2 + |N|^2 + 2\mathrm{Re}\{E_{sx}N^*\}) + \varepsilon|E_{LOx}|^2 + 2\sqrt{\varepsilon(1-\varepsilon)}\mathrm{Re}\{E_{sx}E_{LOx}^* + NE_{LOx}^*\}\right] (2.21)$$

$$S_{x2} = R_2\left[\varepsilon(|E_{sx}|^2 + |N|^2 + 2\mathrm{Re}\{E_{sx}N^*\}) + (1-\varepsilon)|E_{LOx}|^2 - 2\sqrt{\varepsilon(1-\varepsilon)}\mathrm{Re}\{E_{sx}E_{LOx}^* + NE_{LOx}^*\}\right] (2.22)$$

$$S_{x3} = R_3\left[(1-\varepsilon)(|E_{sx}|^2 + |N|^2 + 2\mathrm{Re}\{E_{sx}N^*\}) + \varepsilon|E_{LOx}|^2 + 2\sqrt{\varepsilon(1-\varepsilon)}\mathrm{Im}\{E_{sx}E_{LOx}^* + NE_{LOx}^*\}\right] (2.23)$$

$$S_{x4} = R_4\left[\varepsilon(|E_{sx}|^2 + |N|^2 + 2\mathrm{Re}\{E_{sx}N^*\}) + (1-\varepsilon)|E_{LOx}|^2 - 2\sqrt{\varepsilon(1-\varepsilon)}\mathrm{Im}\{E_{sx}E_{LOx}^* + NE_{LOx}^*\}\right] (2.24)$$

For an ideal balanced receiver, where $\varepsilon = 0.5$ and $R_k = R$, the outputs of the coherent receiver become

$$S_{Ix}(t) = S_{x1} - S_{x2} = 2R\mathrm{Re}\{E_{sx}E_{LOx}^* + NE_{LOx}^*\} \quad (2.25)$$

$$S_{Qx}(t) = S_{x3} - S_{x4} = 2R\mathrm{Im}\{E_{sx}E_{LOx}^* + NE_{LOx}^*\} \quad (2.26)$$

Both the in-phase and quadrature components are retained, making the receiver digital signal processing possible. These electrical signals are sampled using a real-time sampling scope and then forwarded for offline signal processing.

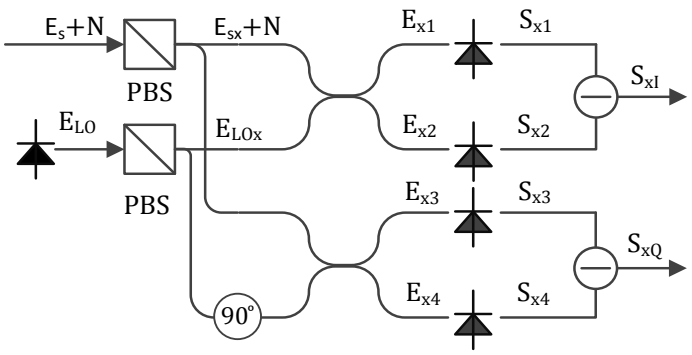

Figure 2.2. Coherent receiver structure for one polarization.

The first stage of the coherent demodulation is the dispersion compensation. The CD is a linear transmission channel impairment that causes a parabolic phase change of the transmission signal with the frequency domain transfer function modeled as [77]

$$H_{CD}(f) = exp\left(-i\frac{\pi cDL}{(f_c - f)^2}f^2\right) \tag{2.27}$$

where L is the fiber length and D is the fiber dispersion coefficient defined in Eq. 2.5. For an unknown transmission system, the total accumulated dispersion DL can be estimated blindly via various approaches [78, 79]. f_c is the carrier frequency and f is the frequency of the electrical signal ($-F_s/2 \le f \le F_s/2$, F_s is the ADC sampling rate). Since $f_c \gg f$, $(f_c - f)^2$ can be approximated by f_c^2. In a dispersion unmanaged link, the digital CD compensation module removes the accumulated dispersion by applying the same transfer function with negative sign to the baseband signal. The minimum tap length of $H(f)$ is estimated by $cLDf_{max}F_s/f_c^2$, where f_{max} is the frequency of the spectrum edge of the transmitted signal [77]. The most straightforward way to implement this linear filter is to convolve it with the baseband signals. However, the computation complexity is proportional to the square of the filter tap length. The other approach is to implement this

filter in the frequency domain using the overlap-save method [77, 80] which significantly reduces the implementation complexity.

After CD removal, either polarization de-multiplexing or timing recovery is performed. It is found that the system performance can be slightly improved if the polarization de-multiplexing is performed synchronously. Symbol timing recovery removes the sampling jitter of transmitter and receiver clock sources by extracting the periodic clock tone from the received signal spectrum and conveys samples corresponding to the maximal eye opening. Timing recovery is realized via the feedforward digital filter and square method [81].

Denote the $r(n)$ as the discretely sampled received baseband signal, the squared output of r_k contains a spectral component at the clock frequency $1/T$, Figure 2.3. This clock tone is obtained by computing the complex Fourier coefficients of $x(n)$ and the normalized phase of the coefficient is an unbiased estimation of the time error for the m_{th} data block [81].

$$\hat{\tau}_m = -\frac{1}{2\pi}\arg\left\{\sum_{n=mLM}^{(m+1)LM-1} |r(n)|^2 \exp\left(-\frac{i2\pi n}{M}\right)\right\} \qquad (2.28)$$

Square timing recovery is a block process with the block size denoted as M. M is properly chosen such that it is sufficient long to average out the channel noise and is able to track the timing variation. $\hat{\tau}_m$ delivers a time error that is normalized to the oversampling rate and has a value between $[-1/2, 1/2]$. During compensation, $\hat{\tau}_m$ has to be converted to the sampling index. Meanwhile, the timing error is continuous, therefore the estimated $\hat{\tau}_m$ has to be unwrapped before being used for sampling error correction [82].

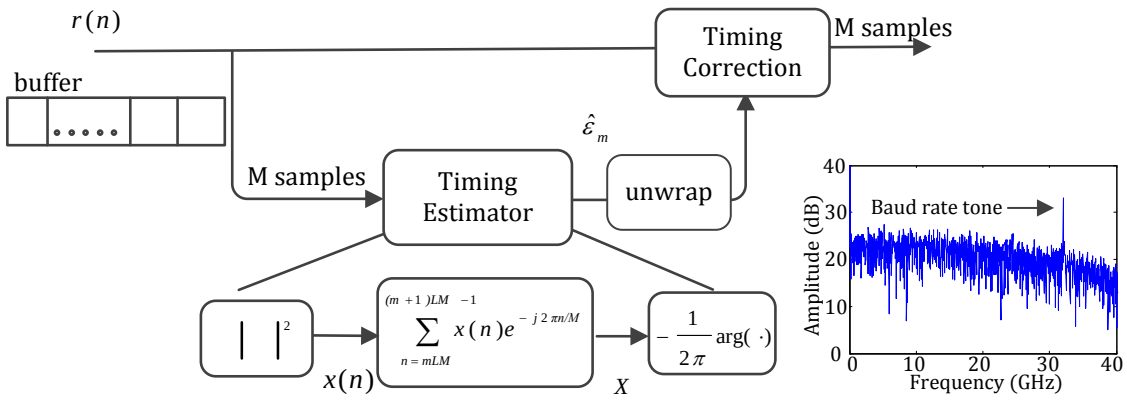

Figure 2.3. Block diagrams of the discrete filter and square timing recovery.

In a dual polarized system, the signals arriving at the coherent receiver are separated into two linear polarized components with a PBS. Because the signals have an arbitrary state of polarization, the detected signals contain mixed information from both polarizations. The transmission channel can be modeled by the Jones matrix A, with the input and output electrical filed relation described by [83, 84]

$$E_{out} = AE_{in}$$

$$\begin{bmatrix} E_x \\ E_y \end{bmatrix} = \begin{bmatrix} \sqrt{\varepsilon}e^{i\delta} & -\sqrt{1-\varepsilon} \\ \sqrt{1-\varepsilon} & \sqrt{\varepsilon}e^{-i\delta} \end{bmatrix} \begin{bmatrix} E_{x,in} \\ E_{y,in} \end{bmatrix} \quad (2.29)$$

where $E_{x/y,in}$ ($E_{x/y}$) are the channel input (output) electrical fields corresponding to the X and Y polarization respectively. ε and δ denote the power splitting ratio and the phase difference between the two polarization. For QPSK modulation, the envelope of each input component $E_{x/y,in}$ is normalized to one. The goal of the polarization de-multiplexing is to identify the inverse of the Jones matrix such that $A^{-1}E_{out}$ approximates E_{in}. Thus, polarization de-multiplexing may be performed through a 2×2 multiple-input multiple-output (MIMO) expressed as

$$\begin{bmatrix} E_X \\ E_Y \end{bmatrix} = \begin{bmatrix} H_{xx} & H_{xy} \\ H_{yx} & H_{yy} \end{bmatrix} \begin{bmatrix} E_x \\ E_y \end{bmatrix} \tag{2.30}$$

The elements in the matrix are complex valued coefficients. To ensure proper convergence, the following coefficients constrains must apply $H_{xx} = H^*{}_{yy}$ and $H_{xy} = H^*{}_{yx}$. The blind identification of the matrix is based on the commonly used constant modulus algorithm (CMA), which targets at bringing the electrical fields to have constant amplitudes [85]. Specifically, the coefficients are updated by

$$H_{xx}(n) = H_{xx}(n) + \mu(1 - |E_X(n)|^2)E_X(n)E^*{}_X(n) \tag{2.31}$$

$$H_{xy}(n) = H_{xy}(n) + \mu(1 - |E_X(n)|^2)E_X(n)E^*{}_Y(n) \tag{2.32}$$

Table 2.1. Examples of CMA algorithms for 64QAM polarization de-multiplexing.

Algorithms	Error Functions	Remarks
Constant modulus algorithm	$y(n)(Ri^2 - \|y(n)\|^2)$	Use for pre-convergence (first or second ring)
Cascade two-modulus algorithm	$y(n)\left(\left\|\|y(n)\| - r_1\right| - r_2\right| - r_3\right)$ $r_1 = \frac{Ri_1+Ri_2}{2}, r_2 = \frac{Ri_3-Ri_1}{2}, r_3 = \frac{Ri_3-Ri_2}{2}$	Unstable at low OSNR
Multi-modulus on real and imaginary part	$4\, y_{re}(n)(\|y_{re}(n)\|^2 - Ri^2) + i4y_{im}(n)(\|y_{im}(n)\|^2 - Ri^2)$	Los tolerance to frequency offset
Weighted multi-modulus algorithm	$y(n)\left(\|y(n)\|^{\lambda} Ri^2 - y(n)^2\right)$	λ needs to be optimized

CMA algorithm uses one constant ring value for computing the error function of QPSK signal and the error function needs to be modified for polarization de-multiplexing of high order modulation formats. Table 2.1 summarizes examples of different CMA algorithms for the 64QAM polarization demultiplexing [86-88]. Ri is the ring value and $y(n)$ is the equalizer output.

In practical transmission system, the LO laser is generally not strictly phase locked to the transmitter laser and is slowly drifting over time. The coherent receiver observes the phase penalty of the received signal in two aspects: the frequency offset and the carrier phase noise. Denote the transmitter and LO lasers as $e^{i(\omega_s t+\phi_s)}$ and $e^{i(\omega_{LO} t+\phi_{LO})}$, where ω_s (ω_{LO}) is the carrier angular frequency of the transmitter (LO) laser. ϕ_s (ϕ_{LO}) is the phase of the transmitter (LO) laser. Frequency offset $\Delta\omega$ is the carrier frequency difference between the transmitter and LO lasers.

$$\Delta\omega = \omega_s - \omega_{LO} \tag{2.33}$$

The frequency offset is treated as a constant over a fairly long time period because it varies slowly in a real transmission system. $\Delta\omega$ can be compensated by applying a constant rotation factor to the frequency. Carrier phase noise is the phase noise difference between the transmitter and LO lasers. At certain discrete time instant n, the phase noise can be represented by

$$\phi(n) = \phi_s(n) - \phi_{LO}(n) \tag{2.34}$$

When the signal and LO lasers have Lorentzian line-shape, the phase noise can be modeled by a Wiener process as follows

$$\phi(n) = \phi(n-1) + \psi(n) \tag{2.35}$$

where $\psi(n)$ is a Gaussian noise sequence with variance σ_ψ^2

$$\sigma_{\psi}^{2} = 2\pi T \Delta \upsilon \quad (2.36)$$

$\Delta \upsilon$ is the sum of the full width half maximum linewidths of the signal and LO lasers [89] and T is the symbol rate. The phase noise can be estimated by removing the data modulation and then track the phase change.

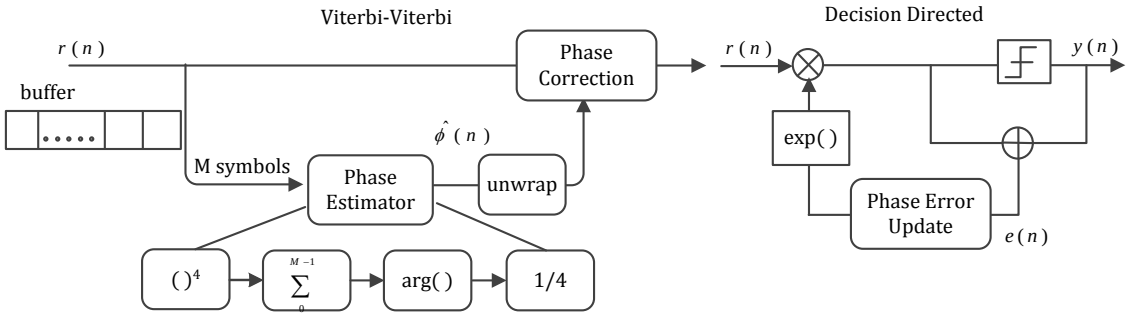

Figure 2.4. Block diagram of Viterbi-Viterbi carrier phase recovery.

We first introduce the phase recovery based on the Viterbi-Viterbi algorithm and take QPSK signals as an example. Consider a sequence of QPSK symbols in a polar representation with phase noise $\phi(n)$

$$r(n) = e^{-i\Theta(n)+\phi(n)} + N(n), n = 0,1 \ldots, M-1, \Theta(n) \in \left\{\frac{\pi}{4}, \frac{3\pi}{4}, \frac{5\pi}{4}, \frac{7\pi}{4}\right\} \quad (2.37)$$

where $N(n)$ is complex Gaussian noise. The phase noise is assumed to be constant over M symbols. The Viterbi-Viterbi phase estimator computes the phase by raising $r(n)$ to the power of four to remove data modulation and then sum them over M symbols to remove the channel noise. The phase of the resulting signal is considered as the estimated phase noise $\hat{\phi}(n)$.

$$\hat{\phi}(n) \approx \frac{1}{4}\arg\left[\sum_{n=0}^{M-1} r^4(n)\right] \tag{2.38}$$

$\hat{\phi}(n)$ lies in between $-\pi/4$ and $\pi/4$ and has to be unwrapped before compensating [89, 90]. The phase unwrapping process is described as [65]

$$\hat{\phi}(n) = \hat{\phi}(n) + \frac{2\pi}{4} f\left(\hat{\phi}(n) - \hat{\phi}(n-1)\right) \tag{2.39}$$

where $f(x)$ is defined as

$$f(x) = \begin{cases} 1, x < -\pi/4 \\ 0, |x| \leq \pi/4 \\ -1, x > \pi/4 \end{cases} \tag{2.40}$$

The carrier phase recovery algorithm for higher order modulation format is performed using the decision directed approach which is derived from the "stop-and-go" algorithm [47, 64, 91]. The phase error is estimated by

$$\hat{\phi}(n+1) = \hat{\phi}(n) - \mu \mathrm{Im}\{y(n)e^*(n)\} \tag{2.41}$$

where $e(n)$ is the error function defined as

$$e(n) = r(n)e^{-i\phi(n)} - y(n) \tag{2.42}$$

$y(n)$ is the slicer output of $r(n)e^{-i\hat{\phi}(n)}$ and μ is the step size.

The last stage of the coherent demodulation is the linear equalization, which compensates the residual ISI and CD in the link and produces the optimum estimation of the transmission sequences. It assumes that the channel is stationary (time invariant) over a long period of time. Although different linear equalization structures and coefficients update algorithms are available, the most straightforward one is the decision directed LMS (DD-LMS) algorithm based on steepest descent principle [80]. The equalizer is implemented in a blind fashion, where the Euclidean distance between the filter output and the reference constellation point is used to update the tap weights. Equalization is

performed on X/Y-polarization separately. The linear equalizer in this work operates at one sample/symbol and can be extended to multiple samples/symbol operation.

2.4 Introduction of Simulation Tools

Extensive simulations are performed in this work using the Optism Rsoft. This simulation tool performs design of the optical system in a propagation level, where different optical components and the optical fiber linear and nonlinear characteristics are modeled. Table 2.2 exemplifies the key simulation components in a 32 Gbaud PM-QPSK system for standard single model fiber (SSMF) propagation.

Table 2.2. Important simulation parameters in Optism Rsoft.

Components	**Parameters**
Laser	Laser linewidth: 0.1 MHz
Modulator	Insertion loss:3 dB, Extinction ratio: 13 dB, V_π: 2.5 V, Bandwidth: 25 GHz
Optical Filter	3.5^{th} order Super Gaussian fiber, Filter bandwidth:50 GHz
Optical Fiber	Loss: 0.2 dB/km, Dispersion: 17 $ps/nm/km$, PMD: 0.05 $ps/\sqrt{km}$, Nonlinear coefficient: 1.16 $/w/km$
Optical Amplifier	Noise figure: 6 dB
Electrical Filter	10^{th} order Bessel Filter, Filter bandwidth: 22 GHz
Photodetector	Responsivity: 0.87 A/W, Dark current: 0.1 nA, Bandwidth: 30 GHz,

CHAPTER 3

DAC ENABLED TRANSMITTER PRE-SHAPING

In optical communication links, the Nyquist WDM system attempts to address the demand of increasing channel capacity by allocating each subchannel equal to or close to the baud rate [20]. Because of the lack of synchronized information from different sub-channels for ICI compensation, the transmitter narrow band optical filtering or pre-shaping is compulsory before multiplexing for suppressing the crosstalk as much as possible, leaving the residual ISI to be compensated at the receiver. Nonetheless, the filtering effects of the transmitter, the transmission channel, and the receiver are likely to cause additional ISI effects, especially when the transmitted signal baud rate is boosted to increase the spectral efficiency.

In the following sections, we will introduce two blind channel estimation approaches with their performance compared. The noise impairments on the inverse channel estimation are also investigated. Both simulations and experiments are used to validate the proposed algorithms' capabilities in ISI compensation. Other than pre-shaping, we also investigate the CD pre-compensation using the DAC to investigate the dispersion map effects on system performance when the LO laser linewidth is large.

3.1 Least Mean Square Directed Transmitter Pre-shaping

The pre-shaping method based on the DD-LMS is discussed at first. The transmitter pre-shaping principle is to perform digital filtering of the baseband signals using the transversal filter transfer function determined at the receiver. Denote the transmission siganl as s_k and the received signals as $r(t)$.

$$r(t) = E_s \sum_{k=-\infty}^{\infty} s_k \, g(t - kT) e^{i\phi(t)} * h(t) + N(t) \qquad (3.1)$$

where $h(t)$ denotes the channel reponse, $N(t)$ is the channel noise, $g(t)$ is transmission pulse shaping, E_s is signal intensity, $\phi(t)$ is the phase, and T is the symbol duration. Since the channel estimation is performed after carrier phase recovery, the phase noise is not presneted in the channel estimation. From the above equation, it is found that if the sampled information of $s_k g(t)$ and the received information $r(t)$ are known, the channel reponse h can be obtained adaptively use the trasverse filter at moderate channel noise. $s_k g(t)$ is the input to the adaptive equalizer and $r(t)$ is the desired output.

The pre-shaping contains two stages: the training stage and the compensation stage. First, training sequences are sent to obtain the pre-shaping transfer function. At the receiver, after coherent detection the baseband training signals undergo conventional DSP procedures, Figure 3.1. Then, the pre-processed signals are forwarded to the linear equalization at the last stage for channel estimation. Because the equalization is preferred in a blind fashion, we use the decision device output rather than the exact transmission sequences to estimate the channel. Therefore, the equalizer is updated every T instant and the DD-LMS aims at achieving a flat spectrum within the Nyquist band. The major advantage of the DD-LMS approach is that no transmission data information is required at the receiver. As long as the modulation format is known, the channel can be estimated blindly. However, because the equalization is performed on the last stage, the channel response estimation is likely to be affected when the channel OSNR is low. A lower order modulation format is used for channel estimation because its tolerance to ASE noise. Meanwhile, a single polarization signal is preferred. It is because we want to pre-

compensate all the ISI effects to benefit from the high SNR at the transmitter. When dual-polarized signals are transmitted, the equalizer in the polarization demultiplexing stage already partially compensates the channel ISI effects and DD-LMS cannot capture all the channel filtering effects, limiting the pre-shaping performance. In the compensation mode, the estimated channel response is applied to the baseband signal and the pre-shaped digital signals are converted to analog drive signals using the high speed DAC.

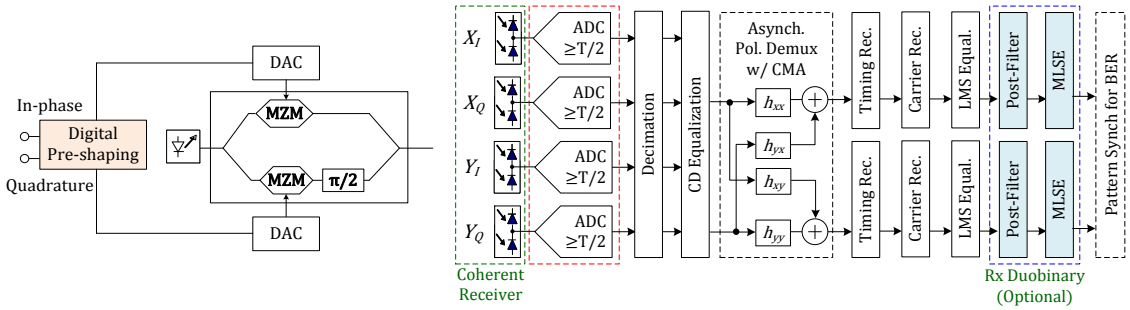

Figure 3.1. Transmitter DAC structure and receiver DSP Block Diagram (Post-filter and MLSE are not used for pre-shaping) [92].

We use duo-binary filtering as a benchmark to show the benefit of the proposed pre-shaping method. The duo-binary filtering is a receiver side compensation which addresses the equalizer noise enhancement problem.and is an efficient way for ISI compensation without sending training sequences [93-95]. The post filter is a two-tap transverse filter with the transfer function of $H(z) = 1 + z^{-1}$ and is performed after the LMS equlization, as seen in Figure 3.1. While the receiver time domain equalizer emphasizes the received singal spectrum at the edges, the ASE noise is also enhanced. In contrast, this duo-binary filter has a filter shape equivalent to the narrow band filtering and the signals are filtered with a known fashion to suppress the ASE noise. Meanwhile,

the signal spectrum is mostly determined by this post filter. Therefore, the decision can be made for given received symbols using the MLSE. The MLSE uses the post filter to compute values of the branches and has a memory of two. The values on the trellis tree branches are determined by the sum of current state and previous state. Then Euclidean distances between the branches and the received signals are computed and the minimum distance is tracked. The symbols along the path that corresponding to the minium distance are considered to be the decision.

For practical implementation, the MLSE is more likely to be used in lower modulation format, therefore, we perform a numerical simulation of a single channel 32Gbaud PM-QPSK system. We transmit NRZ shaped QPSK signals and use the 10th order Butterworth electrical filter with different bandwidths to introduce ISI effects. Then the DD-LMS equalizer estimates the optimal inverse channel response and the obtained pre-shaper is used at the transmitter for ISI compensation.

The required OSNR versus eletrcial transmitter bandwidths at a fixed bit error ratio (BER) for a single channel PM-QPSK system is demonstrated in Figure 3.2. OSNR penalty increases with the decreasing of transmitter filter bandwidths of the conventional receiver due to the receiver equalizer noise enhancement. The proposed DD-LMS pre-shaping method outperforms the conventional receiver LMS equalizer and is more beneficial at narrower electrical filter bandwidth in single channel applications, because most ISI is compensated at the transmitter, relaxing the receiver demodulation burden. The receiver duobinary filtering method shows some penalties at transmitter electrical bandwidths greater than 16 GHz because of the inherent partial response signaling penalties [94].

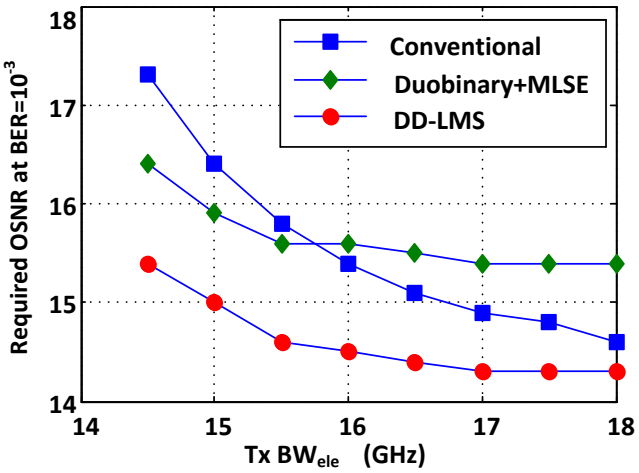

Figure 3.2. Required OSNR at BER=10^{-3} versus transmitter electrical bandwidth for single channel PM-QPSK system.

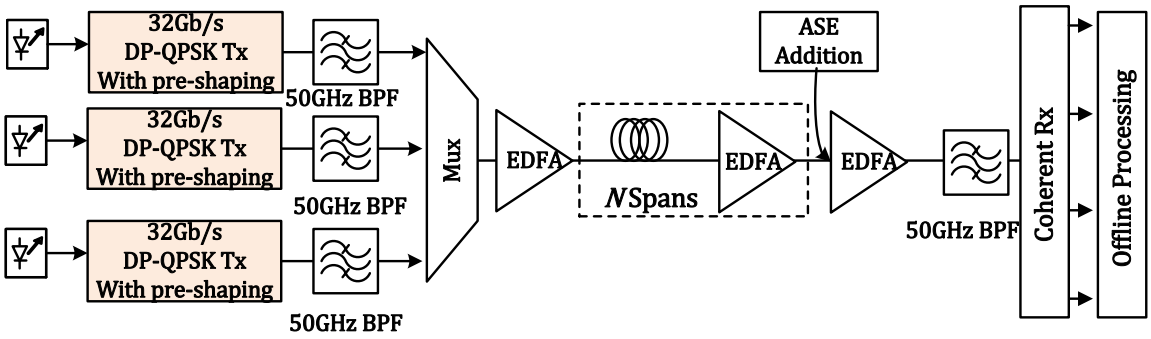

Figure 3.3. Simulation block diagram for a 3×32 Gbaud PM-QPSK system [92].

The pre-shaping performance is also investigated in the tightly spaced WDM system with the center channel performance evaluated. When implemented in 1-bit/s/Hz "superchannel" system (channel spacing equals to the baud rate), the pre-shaping methods retain their advantages at different electrical bandwidths, and a maximum of about 4 dB OSNR gain is observed at bandwidth of 20 GHz, Figure. 3.4. Although more crosstalk occurs with increasing bandwidths, the pre-shaping is still effective because the

transmitted signal is more Nyquist-like. The proposed algorithm still outperforms the duobinary approach.

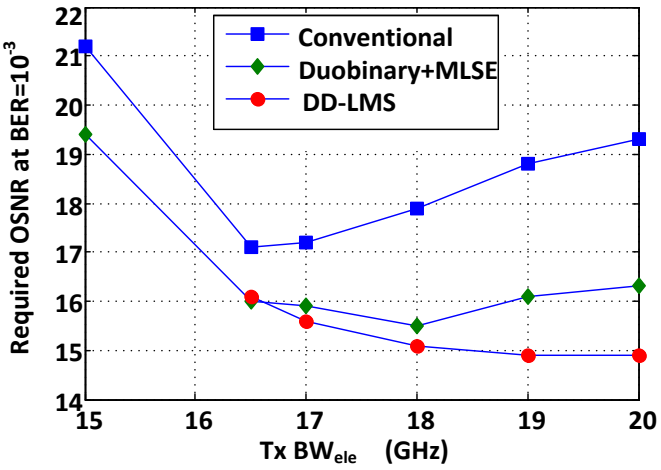

Figure 3.4. Required OSNR at BER=10^{-3} versus transmitter electrical filter bandwidths for 3×32 Gbaud PM-QPSK back-to-back system (channel spacing equals to the baud rate).

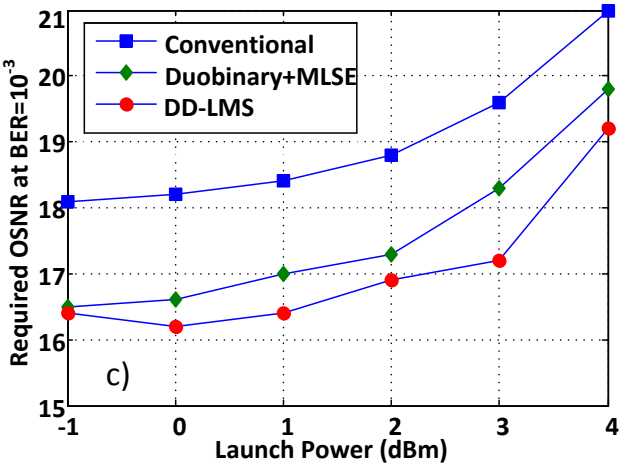

Figure 3.5. Required OSNR at BER=10^{-3} versus launch power for 3×32 Gbaud PM-QPSK system after 12×80 km SSMF transmission (channel spacing equals to the baud rate).

Span test is performed on a 12×80 km SMF transmission system at different launch powers to demonstrate effectiveness in the nonlinear transport regime for a fixed transmitter bandwidth of about 16 GHz, Figure. 3.5. Performance degradations are

observed for each compensation method at high launch powers due to nonlinearities. However, the proposed pre-shaping method retains an overall 2 dB OSNR gain compared with the conventional receiver linear equalization method. Furthermore the proposed method is shown to be comparable to or slightly better than the duobinary approach.

3.2 Frequency Domain Transmitter Pre-shaping

A time domain channel estimation approach based on adaptive filtering is introduced in section 3.1. Although the channel response is estimated in a blind fashion, the performance of the channel estimation relies on the optimization of the receiver demodulation code. Single polarization training sequences with lower order modulation format are preferred for channel estimation. Here we propose a novel channel estimation concept where the inverse channel response is obtained by transmitting signals with flat, Nyquist-like spectra to capture the net channel filtering effects and then computing the received baseband signal PSD [96]. In contrast to other methods, the proposed approach requires no training symbol information and no receiver demodulation. Once the pre-shaper is designed, it can be used to perform system compensation for various baud rates and modulation formats without re-estimating the channel response. In the following discussion, the principle of the pre-shaper design is demonstrated and detail comparison between the frequency domain approach and the DD-LMS will be carried out in terms of channel estimation OSNR and the filter taps. The two pre-shaping methods are demonstrated particularly for Nyquist signaling.

The pre-shaper design is based on the inverse channel response extracted from the received baseband signal without any demodulation. First, training sequences are generated via offline DSP. Unlike other channel estimation approaches where lower order

modulation formats are preferred for training sequence design to ensure an accurate channel estimation that is not affected by the demodulation, the proposed approach can use any *m*-QAM data. The training sequences are designed by up-sampling the transmitted symbols by zero-padding the second sample, resulting in a flat spectral shape. The principle can be understood by considering a simple DSP principle. The spectrum of the *m*-QAM signal at one sample per symbol is flat and occupies the bandwidth of the baud rate. Suppose the DAC operates at two samples per symbol. According to sampling theory, if upsampling the transmission signal by inserting zeros to the second symbol. The spectrum over the total transmission band is flat. Therefore, the training signal modulation formats can be flexibly chosen as long as the waveform has zero mean. At the receiver, the PSD, which now reflects the overall channel narrow filtering, is computed via the baseband information.

The detail of the design scheme is illustrated in Figure 3.6. After two times up-sampling the training sequence by inserting zeros, the signal spectrum is flat over the transmission band, as shown in Figure 3.6 (TP-1). Thereafter, the receiver electrical spectrum reflects the net filtering effects from the transmitter, the transmission channel, and the receiver, Figure 3.6 (TP-3). Because the in-phase and quadrature components usually experience the same filtering effects, only one branch is used to compute the received signal PSD upon receiving the training sequences. Finally the inverse of the square root of the PSD is considered as the pre-shaper, Figure 3.6 (TP-4). Because of the symmetry of the spectra, pre-shaper coefficients corresponding to half of the estimated spectral shape are forwarded to the transmitter side. The transmitter performs offline symbol mapping, two times up-sampling by zero padding, and Nyquist signaling in the

conventional fashion followed by pre-shaping. An example of the pre-shaped signal is demonstrated in Figure 3.7 (TP-6), where the high frequency components are enhanced to overcome channel filtering. After passing through the transmission channel, the received spectrum (TP-3) is close to the Nyquist signal.

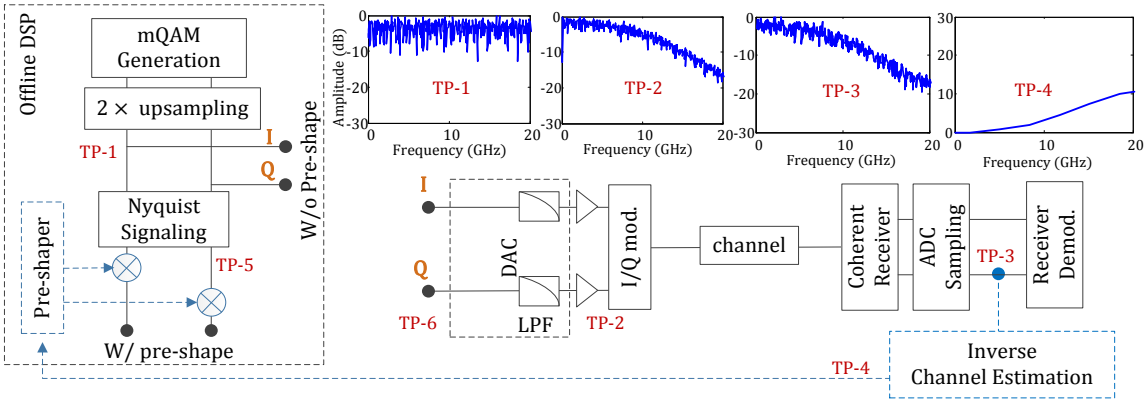

Figure 3.6. Frequency domain pre-shaper design scheme with spectra observed at different test points.

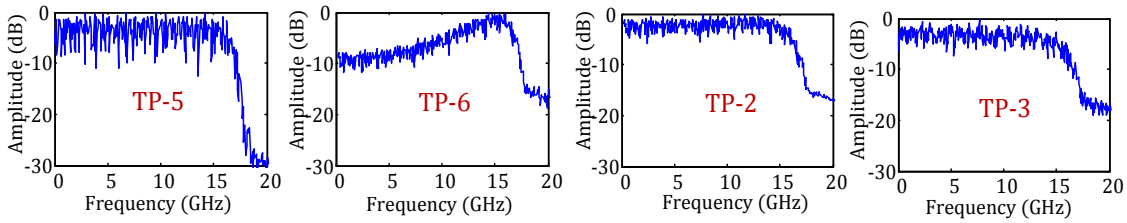

Figure 3.7. Spectra observed at different test points with frequency domain pre-shaping.

We included the DD-LMS design and PSDs at different test points for comparison. The Nyquist shaped signal is sent at first for obtaining the inverse channel response. The PSDs at different test points before and after pre-shaping are given in Figure. 3.8 and 3.9 respectively. Spectrum loses the RRC shape after the cascading filter from the transmitter and receiver (TP-3). On the last stage of the coherent receiver

demodulation, DD-LMS adaptively estimates the inverse channel response within the Nyquist band (TP-4). Then the obtained pre-shaper is applied to the transmitter for ISI pre-compensation. After pre-shaping, the high frequency band has been emphasized (TP-1). The received spectrum after the cascading of the channel filters is near flat, Figure 3.9 (TP-3).

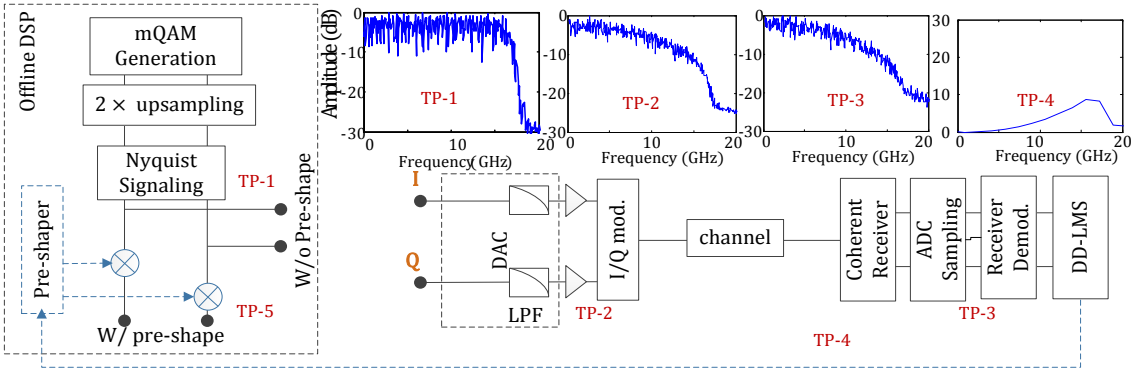

Figure 3.8. DD-LMS pre-shaper design scheme with spectra observed at different test points.

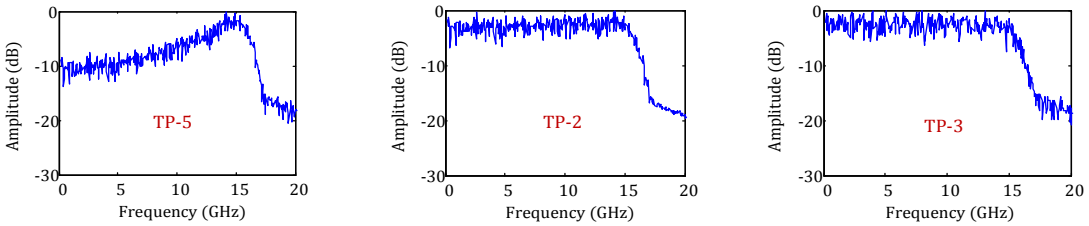

Figure 3.9. Spectra observed at different test points with DD-LMS pre-shaping.

The pre-shaping effectiveness in channel filtering compensation is demonstrated via Rsoft simulation for a 32 Gbaud Nyquist RRC rolloff 0.1 PM-16QAM system with the transmitter DAC operating at 64 Gsamples/s. In the training mode, SP-16QAM with flat spectrum is transmitted. It is noted that X-/Y-pol separation is optional for training sequence design if the channel filtering effects are similar for both polarizations. At the

receiver, after coherent detection and 80 Gsamples/s ADC sampling, the in-phase branch is used to compute the inverse channel response without any further demodulation. Then, coefficients corresponding to half of the inverse spectrum are sent to the transmitter. The pre-shaper filter taps are defined as the total number of coefficients in both negative and positive frequencies. In the demodulation process, a digital Nyquist RRC matched filter is used to maximize the received signal SNR. Then the baseband signals go through chromatic dispersion compensation, square timing recovery, polarization de-multiplexing via independent component analysis (ICA), frequency offset removal, carrier recovery, and DD-LMS equalization. For the DD-LMS approach, channel estimation is performed using lower order modulation format, SP-QPSK signal. Then the obtained channel response is used to compensate the channel. The receiver demodulation algorithm is the same as the frequency domain approach.

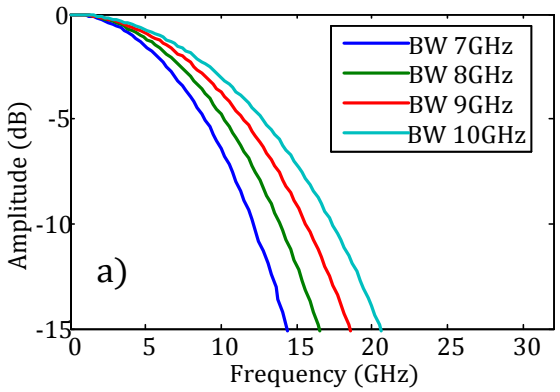

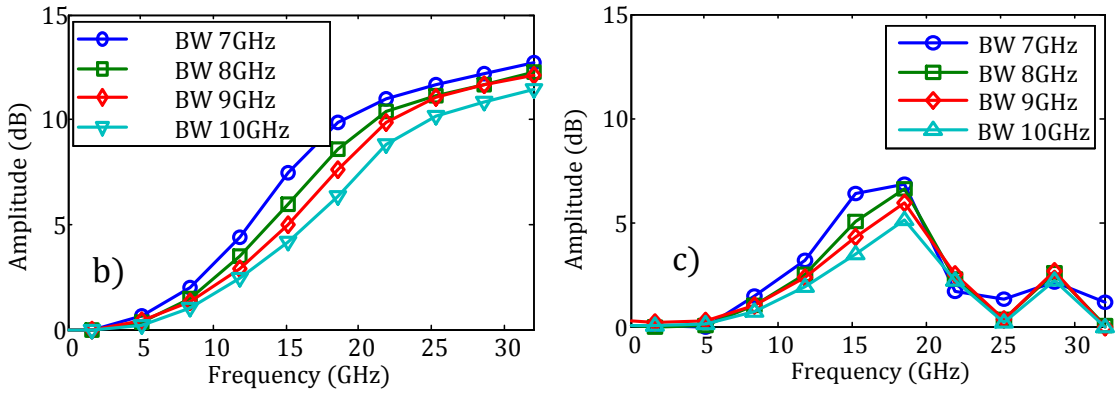

Figure 3.10. a) Transmitter filter shape at different electrical bandwidths b) Frequency domain pre-shapers corresponding to different transmitter electrical bandwidths. c) DD-LMS pre-shapers corresponding to different transmitter electrical bandwidths.

The main filtering effects originate with the transmitter DAC analog bandwidth which is modeled by a 7th order Bessel function with different 3 dB electrical bandwidths, Figure 3.10.a. The corresponding estimated inverse channel responses at different 3 dB electrical bandwidths using the frequency domain approach and DD-LMS are illustrated in Figures 3.10.b and c respectively, with the channel estimation OSNR fixed at 24 dB and with 20 pre-shaper taps. In both cases, the inverse channel response follows the shape of the transmission filter shape. While the frequency domain approach inverses the whole transmission channel, the DD-LMS optimizes the channel response within the Nyquist band, therefore, high frequency bands are attenuated.

The required OSNR versus transmitter electrical bandwidths at BER=5×10^{-3} with and without pre-shaping is demonstrated in Figure 3.11. Without pre-shaping, a 4 dB OSNR penalty is observed as the bandwidth decreases from 14 GHz to 9 GHz, because the receiver demodulation is sensitive to ISI. The frequency domain pre-shaping delivers consistent and significant performance improvements at all transmitter bandwidths, showing over 4 dB OSNR improvement for bandwidths smaller than 9 GHz and an

overall OSNR improvement compared to the DD-LMS approach. Within 2 dB penalty shows at an electrical bandwidth of 7 GHz with both pre-shaping approaches, enables high baud rate ISI free Nyquist signal transmission.

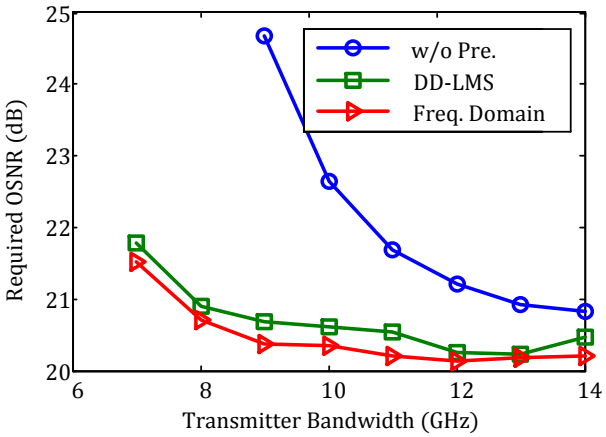

Figure 3.11. Required OSNR at BER=5×10^{-3} versus electrical filter bandwidths with and without pre-shaping,

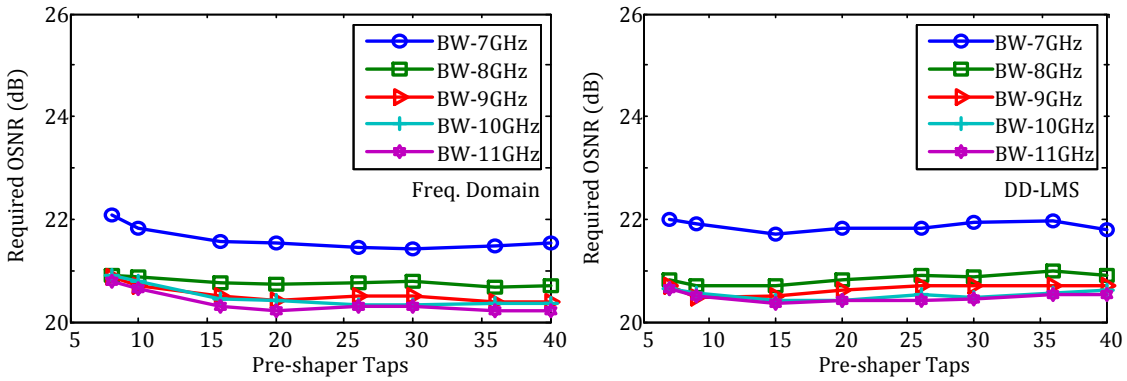

Figure 3.12. Required OSNR at BER=5×10^{-3} versus number of filter taps at different transmitter electrical bandwidths with two pre-shaping methods (OSNR=28 dB).

The impact of the tap length of the pre-shaper performance is shown in Figure 3.12. Both pre-shaping methods show great tolerance for the tap length at different

transmitter filter bandwidths. However, at small equalizer taps, the frequency resolution between each frequency domain taps is insufficient to capture the channel distortion and small degradation is showing up. In both pre-shaping approaches a tap length greater than ten is preferred to have a performance without penalty.

A success estimation of the transmission channel response significantly improves the pre-shaping performance. The above work assumes that channel estimation is performed at high OSNR and the filter tap length is sufficiently long to capture the channel response. As in real systems, the channel OSNR is limited and thus affecting the received signal quality. Thereafter, we study the channel estimation OSNR impacts on the pre-shaping performance. The pre-shaper frequency responses at different OSNR are exemplified in Figure 3.13 with transmitter electrical bandwidth at 7 GHz. The inverse channel responses have similar shapes at different OSNR up to the frequency of 8 GHz with the amplitude of the side lobes decreasing with a reduction of channel estimation OSNR at frequency beyond 8 GHz. For the DD-LMS approach, the channel response cannot be achieved for channel OSNR below 9 dB.

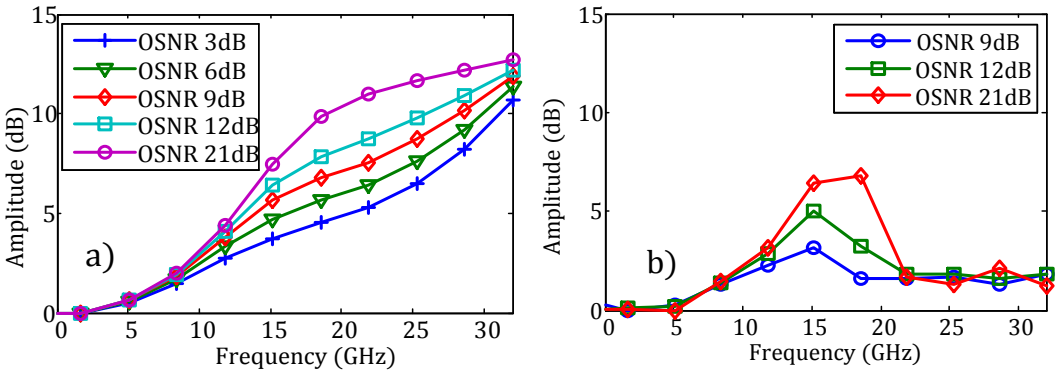

Figure 3.13. a) Frequency domain pre-shapers corresponding to different channel estimation OSNR. b) DD-LMS pre-shapers corresponding to different channel estimation OSNR (transmitter bandwidth 7 GHz).

The channel estimation OSNR impacts on BER performance of fixed filter taps of 40 are demonstrated in Figure. 3.14. In the frequency domain approach, the OSNR effects on channel estimation are less important at bandwidth greater than 9 GHz. Channel OSNR (single polarization) as low as 3 dB can be used to estimate the channel response when filter bandwidth is at 10 GHz. Because part of the channel response is shadowed by the ASE noise, the BER starts to increase once the OSNR decreases to 12dB at electrical bandwidth smaller than 9 GHz. The DD-LMS approach is less tolerated to the channel estimation OSNR because the failure in receiver demodulation. Even at large filter bandwidths, significant performance degradation is observed for OSNR smaller than 8 dB. For transmitter bandwidth smaller than 8 GHz, the preferred channel estimation OSNR of DD-LMS is higher than 20 dB.

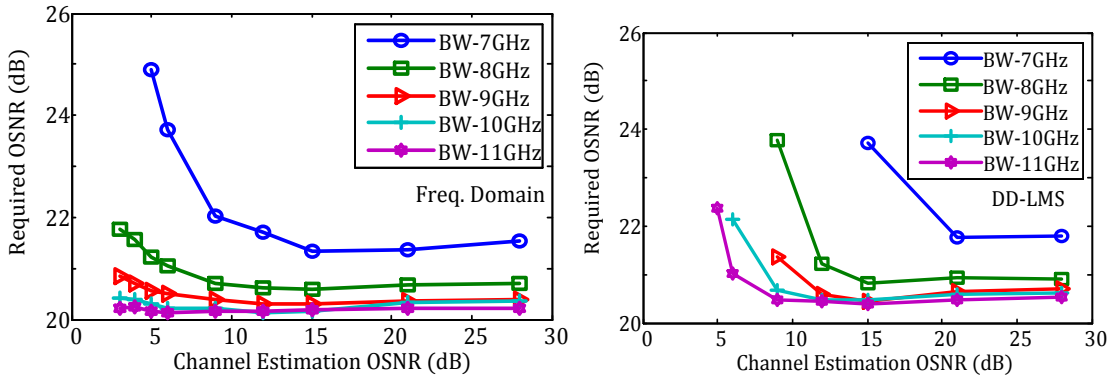

Figure 3.14. Required OSNR at BER=5×10^{-3} versus channel estimation OSNR at different transmitter electrical bandwidths with two pre-shaping methods (tap length is 40).

3.3 Experimental Comparison and Validation

We experimentally validate the proposed two pre-shaping approaches using a 32 Gbaud PM-16QAM system and compare their performances. The pre-shaping design principles in the experiment are the same as the simulation. For DD-LMS pre-shaping, we transmit Nyquist-shaped QPSK training sequences with roll-off 0.1 and let the DD-LMS optimize the transmitter waveform in the training mode. A single-polarization training signal is sent to avoid interference between X and Y polarizations. After timing recovery, residual frequency offset removal and carrier recovery, the two samples per symbol DD-LMS equalizer is used to compensate the channel ISI effects. When the equalizer tap weights reach a steady state, they are saved as the pre-shaping filter. For the frequency domain estimation, we create a 16QAM training sequence with flat spectrum. At the receiver, after real-time sampling, the received signal PSD is computed without any further demodulation. The square root of the inverse of the received signal PSD is obtained and saved as the pre-shaper.

An example of the estimated inverse channel responses is given in Figure 3.15. In all cases, the high frequency components within the transmission signal optical bandwidth (32 GHz) are enhanced to compensate the channel narrow band filtering. For the frequency domain approach, the overall channel is inverted. Although, the DD-LMS pre-shaper is complex valued and has the potential for phase compensation, the amplitude response of the inverse channel is the most significant feature of the pre-shaper design since this directly impacts the received SNR and the phase impairments can be corrected at the receiver.

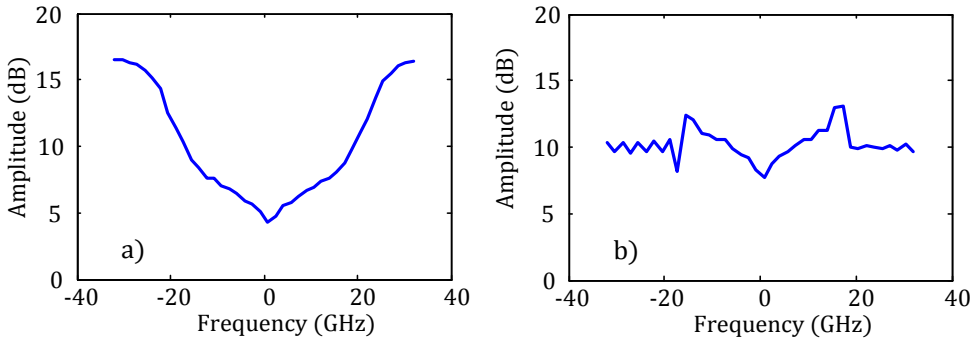

Figure 3.15. Estimated inverse channel frequency response: a) frequency domain, b) DD-LMS.

The experiment setup with transmitter pre-shaping is in Figure 3.16. In the transmitter, we use a high speed DAC with a nominal sampling rate of 64 GHz and ENOBs of eight. The baseband digital signals are generated offline and loaded to the DAC. A linear driver is used to amplify the signal to drive the modulator. The bias control board is biased at null and operates at V_π mode. The PM is created by delaying one polarization with respect to the other. Following coherent detection, the signals are sampled via an 80 Gsamples/s Agilent scope and then processed off-line. A Nyquist shaped matched filter is used to maximize the SNR. Polarization de-multiplexing is performed after timing recovery via independent component analysis (ICA) at one sample per symbol; the remaining algorithms also operate at one sample per symbol. During channel estimation polarization de-multiplexing stage is disabled. In all cases, a DD-LMS equalizer is included in the receiver to compensate residual channel impairments.

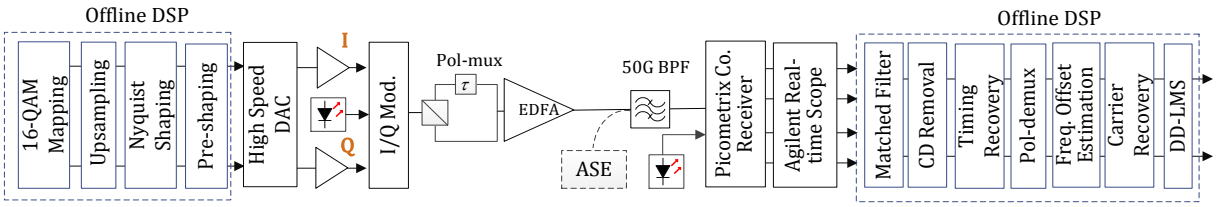

Figure 3.16. Experimental setup for a 32 Gbaud Nyquist PM-16QAM system with pre-shaping.

The BER versus OSNR at different filter taps are shown in Figure 3.17. Similar to the simulation observation, penalties occur when the tap length is small. For DD-LMS approach, slight performance degradation is showing up for tap length equals seven, while in the frequency domain approach, no performance difference is observed for tap length equals to eight.

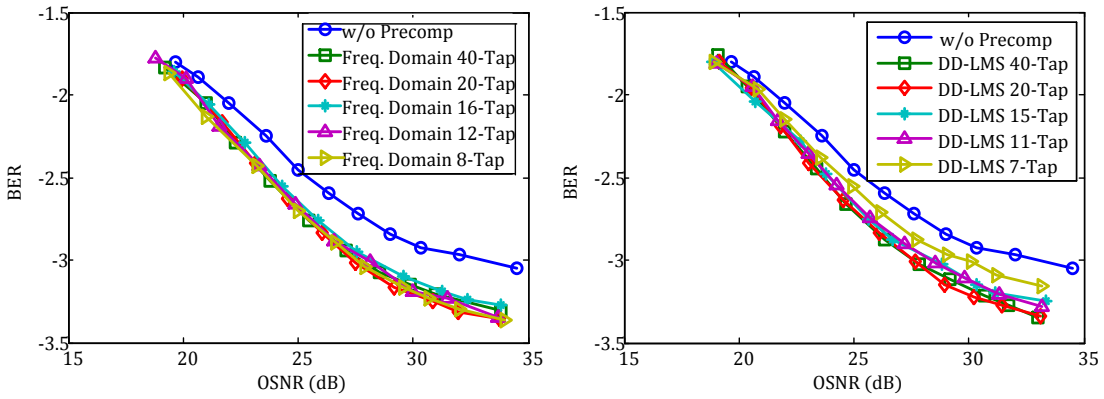

Figure 3.17. BER versus OSNR at different pre-shaper filter taps for two pre-shaping methods (channel OSNR is 30 dB).

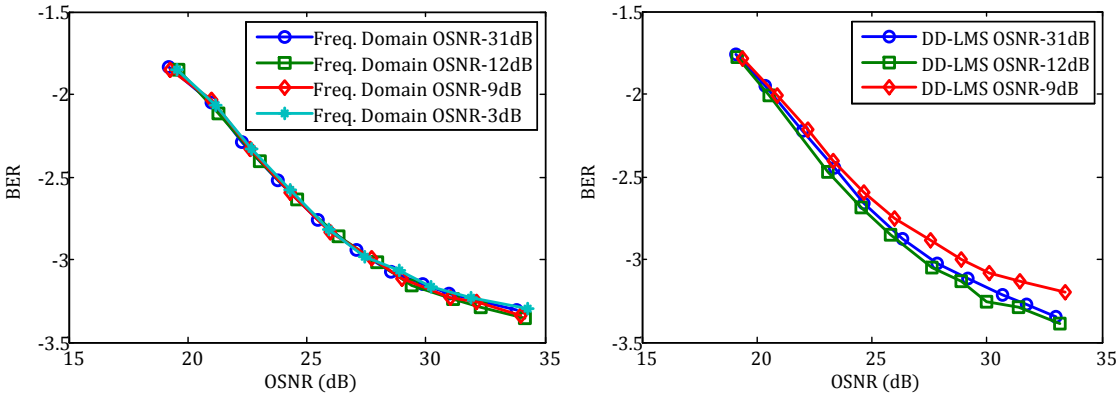

Figure 3.18. BER versus OSNR at different channel estimation OSNR for two pre-shaping methods (pre-shaper tap length is 40).

We fix the tap length at 40 and study the noise impact on channel estimation in Figure. 3.18. For the frequency domain approach, no major performance degradation shows even when the channel OSNR is very low. Channel OSNR as low as 3 dB can be used without introducing performance penalty. However, the DD-LMS approach shows penalty for OSNR at 9 dB and channel estimation fails at OSNR lower than 9 dB.

The frequency domain approach outperforms the DD-LMS approach in terms of channel estimation OSNR. Meanwhile, another advantage of the frequency domain method is that once the channel estimation is done, it can be used for pre-shaping the signal at different baud rates. We demonstrate the frequency domain pre-shaping for PM-QPSK signals at different baud rates using the same estimated pre-shaper, Figure 3.19. In the transmitter, we generate the Nyquist signal at the desired baud rate, eg. for a DAC with 64 Gsamples/s operation rate, the 40 Gbaud (50 Gbaud) signal corresponds to 1.6 (1.28) samples per symbol. Then, the same pre-shaper is applied to the baseband signals at different baud rates. With the increase of baud rate, more OSNR gain is achieved with the pre-shaping. Over 8 dB OSNR improvement has been observed at 50 Gbaud.

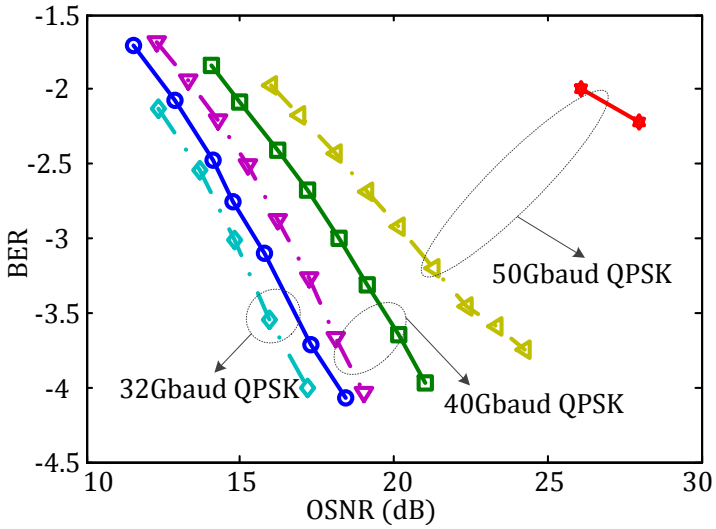

Figure 3.19. BER versus OSNR for PM-QPSK signals at different baud rates using frequency domain pre-shaping (pre-shaper tap length is 40 and channel OSNR is 30 dB).

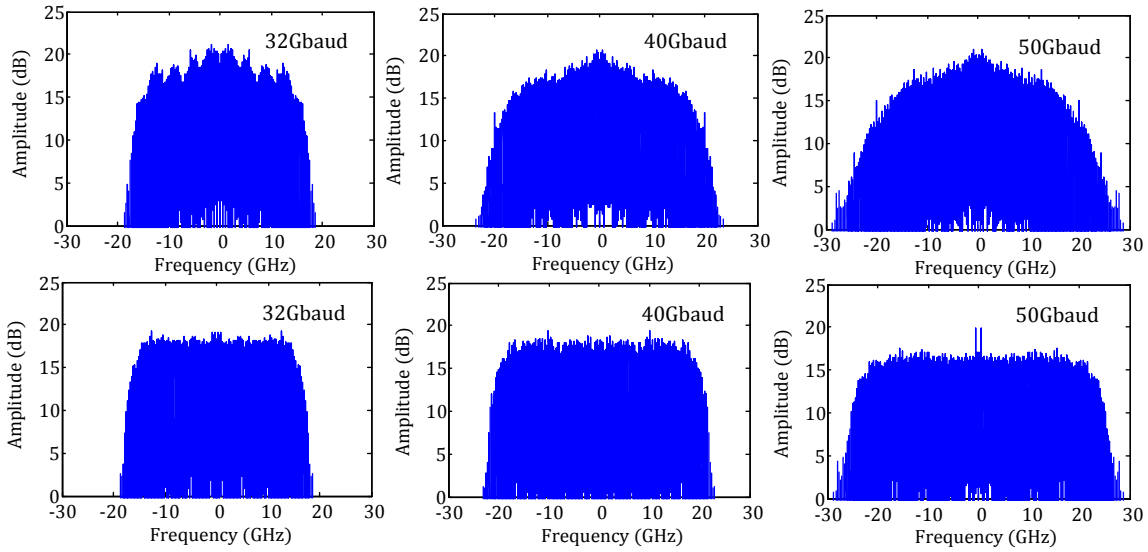

Figure 3.20. Received signal baseband spectrum plots for PM-QPSK signal at different baud rates without (top row) and with (lower row) frequency domain pre-shaping.

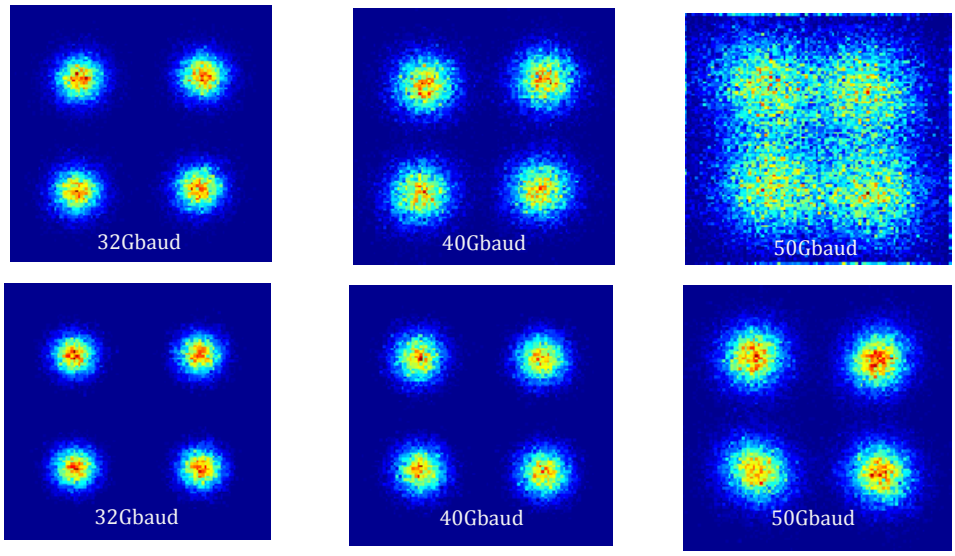

Figure 3.21. Received signal constellation (after carrier phase recovery) for PM-QPSK signal at different baud rates without (top row) and with (lower row) frequency pre-shaping.

The received signal spectra at different baud rates with and without pre-shaping are captured after the receiver matched filter, as shown in Figure 3.20. Without pre-shaping signal loses RC shape because of the channel narrow filtering. And the filtering effects are more significant at high baud rate. After pre-shaping, all the spectra become flat and are close to the RC shape, demonstrating the effectiveness of the frequency domain pre-shaper. The received signal constellations without and with frequency domain pre-shaping are captured after the carrier recovery and before the linear equalization and are demonstrated in Figure 3.21. Improved constellations are observed at different baud rates and the pre-shaping showing significant advantage when the baud rate is high.

3.4 Transmitter CD Compensation

Despite of performing transmitter pre-shaping to compensate the channel narrow band filtering, the DAC enables other channel impairment compensation, for example the

CD pre-compensation. Transmitter electronic CD pre-compensation has been experimentally demonstrated in PM-BPSK super-channel systems for nonlinearity mitigation and is beneficial for other one-dimensional modulation formats (n-PAM) [97]. Furthermore, methods have been developed to mitigate the CD equalizer enhanced phase noise (EEPN) at large LO laser linewidth [98] resulting from LO-phase noise to amplitude noise conversion in the CD equalizer. In this work, we will investigate different dispersion pre-compensation maps for a system with the presence of both nonlinearity and large LO laser linewidths. Meanwhile, we show that Nyquist pulse shaping can be effectively incorporated within the CD pre-compensation without adding extra implementation complexity and that with CD pre-compensation the LO laser linewidth requirement is relaxed.

The principle of digital CD pre-compensation with Nyquist pre-shaping is to perform digital filtering of the baseband signals using specific designed filters. The linear filter $H_{CD}(f)$ that compensates the CD is presented in Eq. 2.27 and the Nyquist RRC filter has a transfer function $H_{TX,RRC}(f)$ in Eq. 1.2. When incorporating the Nyquist pulse shaping into the CD pre-compensation, in the frequency domain the new filter becomes: $X(f) = H_{TX,RRC}(f)H_{CD}(f)$. Since RRC shaping is a spectral shaping process while the CD pre-compensation is a phase correction operation, the two functions can be combined without performance penalties. The tap length of $H_{TX,RRC}(f)$ is set to be the same as the CD pre-compensation transfer function (other than 0% CD pre-compensation), which is sufficient for performing Nyquist pulse shaping in long haul transmission systems. The combined filter spectra and phase is depicted in Figure 3.22.

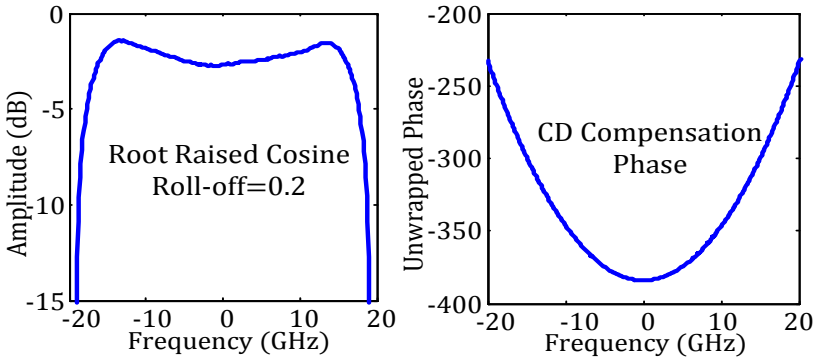

Figure 3.22. CD pre-compensation transfer function amplitude and phase.

Numerical simulation is performed using RSOFT OptSim for a 32 Gbaud PM-QPSK system. The transmission test includes multiple spans of 80 km SSMF transmission. The transmitter laser linewidth is set to be 0.1 MHz and the LO laser linewidth is varied to study the impact of EEPN.

Figure 3.23 shows the required OSNR at BER=10^{-3} with different fractions of the total required CD pre-compensation performed at the transmitter for single channel PM-QPSK system after 12×80 km SSMF transmission. The launch power is fixed at -1 dBm. ν is the laser full width half maximum (FWHM) linewidth and T is the bit period. We choose RRC pulse with roll-off equals 0.2. The receiver CD compensation tap length for the 0%, 25%, 50%, 75%, 100% pre-compensate cases are 256, 256, 128, 64, 0 respectively. The variance of the EEPN induced noise is expressed as: $\sigma^2 = \frac{\pi\lambda^2}{2c}\frac{DL\Delta f_{LO}}{T}$, Δf_{LO} is the 3 dB linewidth of the LO laser [98]. The noise scales linearly with the accumulated dispersion and the linewidth of the LO laser, which is consistent with the results of Figure 3.23. The penalty is seen to be minimized for 100% pre-comp and the penalty increases fastest for 0% pre-comp. We also note the slight improvement in performance for the 100% pre-comp even when the linewidth is not significant i.e.

$log_{10}(\nu T) < -5$. The improvement partially comes from the fact that the receiver DSP operates at a lower sampling rate and lower ENOB than the transmitter DAC, similar to our expected experimental conditions.

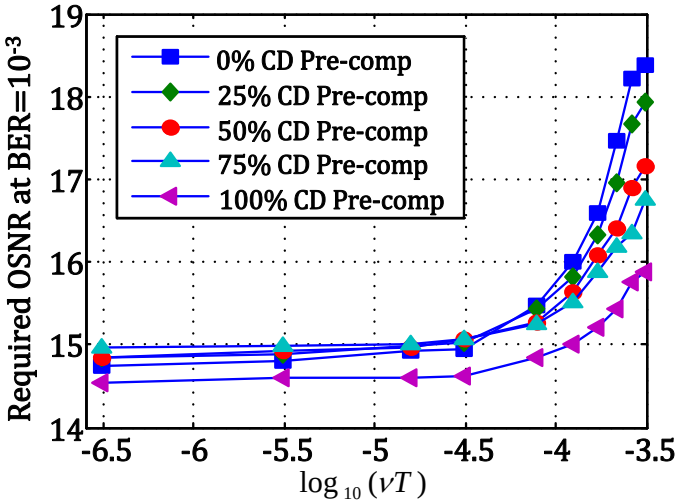

Figure 3.23. Required OSNR at BER=10^{-3} versus LO linewidth × bit duration of 32 Gbaud PM-QPSK system. With 12×80 km SSMF transmission, launch power=-1 dBm. For 32 Gbaud, $log_{10}(\nu T) = -5$ corresponds to ν=0.32 MHz.

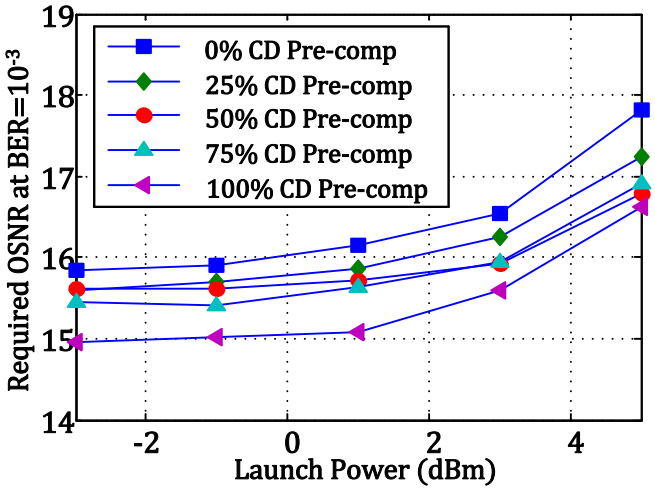

Figure 3.24. Required OSNR at BER=10^{-3} versus launch power for 32 Gbaud PM-QPSK system. With 12×80 km SSMF transmission, νT=1.25×10^{-4}.

The required OSNR at BER=10^{-3} versus launch power with different CD pre-compensation profiles reveals that the benefits of pre-compensation are retained in the nonlinear regime, Figures 3.24 and 3.25. We note that 50% CD pre-compensation shows some benefit in the nonlinear regime. At smaller LO linewidth, small but consistent benefits are observed in systems with 100% CD pre-compensation. Again, the 50% CD pre-compensation case shows slight benefit in the nonlinear regime. System performance versus number of spans is shown in Figure 3.26. With increased transmission distance, the OSNR gains are larger due to the larger EEPN penalty associated the increase of accumulated dispersion.

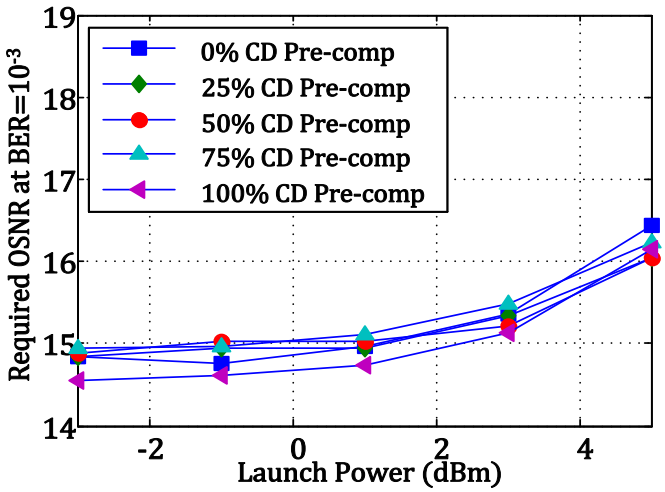

Figure 3.25. Required OSNR at BER=10^{-3} versus launch power for 32 Gbaud DP-QPSK system. With 12×80 km SSMF transmission, νT=1.56×10^{-5}.

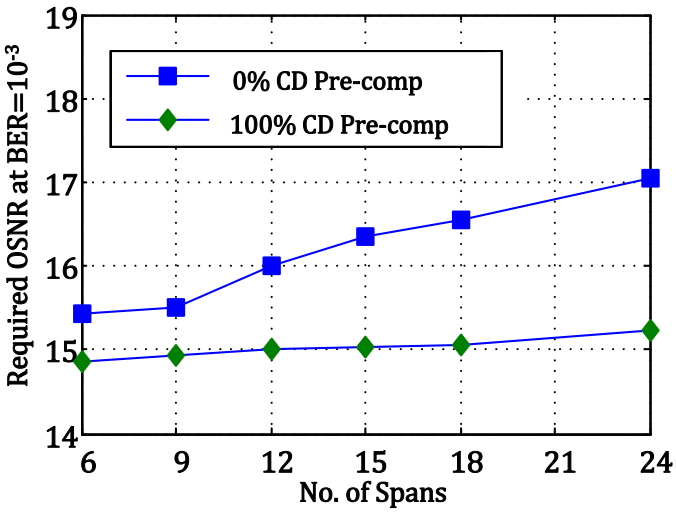

Figure 3.26. Required OSNR at BER=10^{-3} versus different spans of 80 km SSMF transmission for 32 Gbaud PM-QPSK system. LO=4 MHz, launch power=-1 dBm.

3.5 Chapter Summary

In this section, two novel blind pre-shaping schemes were proposed with their performance compared in terms of channel estimation OSNR and tap lengths. Both simulation and experiment have shown that the two pre-shaping methods outperform the conventional receiver equalization, allowing systems to operate at higher baud rates without suffering from significant ISI penalty.

The DD-LMS approach transmits single polarized signals and uses the receiver equalizer to obtain the inverse channel response. Although the DD-LMS pre-shaper is complex-valued and may have the potential for phase compensation, we have observed a linear phase profile in this experiment. The channel estimation is performed in a blind fashion within the Nyquist band and lower order modulation is preferred to obtain optimal results. However, because the channel estimation requires the coherent receiver demodulation, the performance is affected significantly by the channel estimation OSNR and how well the receiver demodulation code is designed.

The frequency domain approach transmits a flat spectral signal and estimates the inverse channel response from the baseband signals without any demodulation. The

proposed approach has been shown to effectively mitigate ISI penalties even at very narrow bandwidths and is very robust to channel noise. Channel estimation can be performed with single polarization OSNR as low as 3 dB without introducing significant performance degradation at electrical bandwidths greater than 9 GHz. Meanwhile, this frequency domain pre-shaper is symmetric and real-valued. Pre-shaper taps corresponding to half of the band are sent to the transmitter. The tap information is typically well described by a few numbers, which minimizes information transmission from receiver to transmitter.

A simplified Nyquist pulses implementation was proposed and demonstrated for systems that employ electronic CD pre-compensation. It is concluded that CD pre-compensation may reduce the effects of EEPN.

CHAPTER 4

RECEIVER MIMO DIGITAL SIGNAL PROCESSING

In a Nyquist system, subchannels are placed as close as possible to increase spectral efficiency. Thereafter, subchannels experiences performance degradations at tight channel spacing due to ICI. Because of the likelihood of high capacity terabit super channel systems experiencing ICI impairments and the increasing capabilities of DSP and electronics, it is important to quantify the benefits of jointly demodulating multiple subcarriers. In the following sections, we will propose a new super-receiver architecture, which performs synchronized sampling for each sub-channel, and thus enables ICI cancellation. First, the super channel configuration and modeling is introduced. Then, the techniques that enable the joint signal processing are investigated, including the joint chromatic dispersion compensation, side-channel frequency shifting, and inter-channel skew removal. Finally, joint ICI cancellation algorithms are proposed. Meanwhile, we also propose a joint carrier phase recovery based on the Viterbi-Viterbi algorithm for carrier locked lasers.

4.1 Nyquist System Configurations

In this work, rather than examining methods to achieve a near perfect rectangular spectrum and hence a true Nyquist system, we focus on a more general case, in which optical filtering is performed to constrain and shape the spectra, and for which is residual ISI and ICI to be compensated. The primary elements of a super-channel system include a method to generate the signal constellation, optical filtering, channel spacing equal to the baud rate to achieve high spectral efficiency, coherent detection and demodulation, as

illustrated in Figure 4.1. Because of the imperfections of the spectral shaping, after multiplexing, subchannels interfere with neighboring channels causing linear and nonlinear crosstalk [99]. For the conventional coherent receiver, after transmission, each subchannel enters independent receivers for O/E and electrical filtering, as shown in Figure 4.1. The resulting baseband signals are fed into the DSP block for CD compensation, PMD compensation, timing recovery, carrier phase recovery, and equalization.

This receiver structure deals with each subchannel independently and does not possess the ability to cancel the linear crosstalk. To address this problem, we propose a new receiver structure in which frequency locked LO lasers are used to beat with the carrier for signal down converting. After O/E, each subchannel undergoes separate but synchronized sampling, Figure 4.2. Thereafter, the synchronized data from each subchannel are available, enabling joint receiver inter-channel impairment compensation.

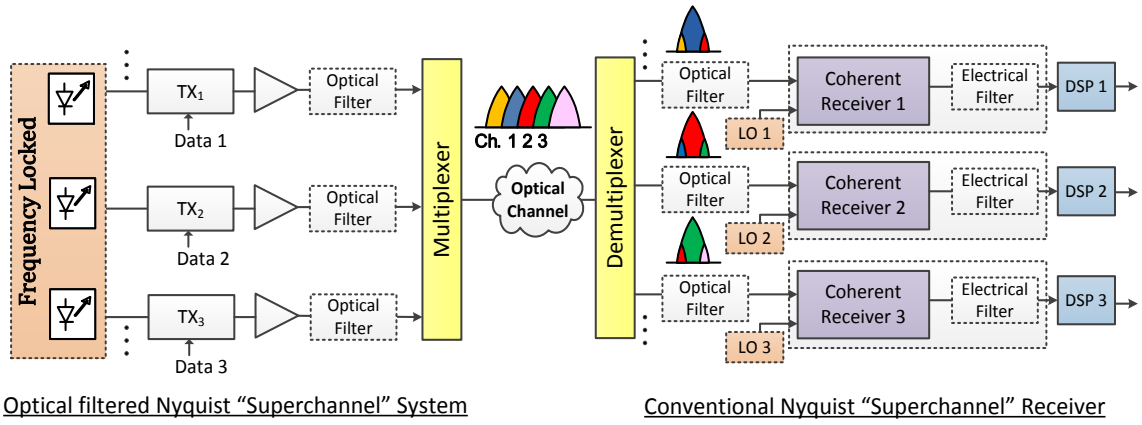

Figure 4.1. Super-channel system design and conventional coherent receiver structure.

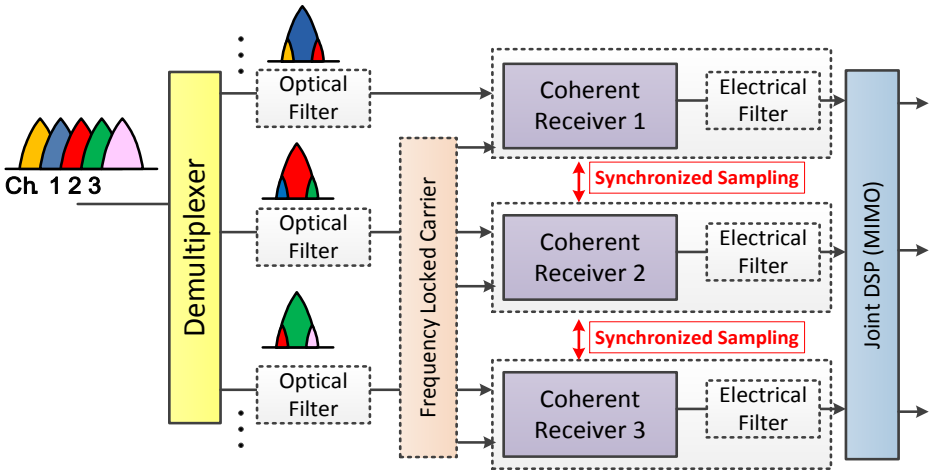

Figure 4.2. Proposed super-receiver structure with synchronized sampling.

The actions of the ICI cancellation via the synchronized baseband signals from each subchannel can be seen in depth by consideration of the received electric field. If E_s denotes the optical field intensity and P represents the total number of subchannels transmitted, the pass-band optical field before de-multiplexing can be written as

$$E(t) = Re\left\{E_s \sum_{j=1}^{P} \sum_{k=-\infty}^{\infty} s_{j,k}\, g(t-kT) e^{i(\omega_j t+\phi_j)}\right\} \qquad (4.1)$$

where ω_j and ϕ_j are the frequency and phase of the j_{th} carrier. $s_{j,k}$ is the k_{th} complex or real valued symbol on the j_{th} carrier formed by a variety of modulation formats. $g(t)$ is the baseband signal profile before demultiplexing and is assume to be the same for all subcarriers.

Suppose the receiver phase noise is negligible, the baseband signal captured by the l_{th} receiver can be written as

$$r_l(t) = E_s \sum_{j=1}^{P} \sum_{k=-\infty}^{\infty} s_{j,k}\, g_{j,l}(t-kT) e^{i\phi_j} + N(t) \qquad (4.2)$$

where $N(t)$ represents the ASE noise, thermal noise, and shot noise. $g_{j,l}(t)$ denotes the signal profile of the j_{th} channel after demultiplexed by the l_{th} channel and it can be represented as

$$g_{j,l}(t) = \frac{1}{2\pi}\int_{-\infty}^{+\infty} G\big(\omega - \omega_j + \omega_l\big)G_r(\omega)e^{i\omega t}d\omega \qquad (4.3)$$

and in frequency domain $G_{j,l}(\omega)$ is:

$$G_{j,l}(\omega) = G\big(\omega - \omega_j + \omega_l\big)G_r(\omega) \qquad (4.4)$$

$G(\omega)$ is the frequency domain representation of the baseband signal before demultiplexing $g(t)$. $G_r(\omega)$ is the equivalent baseband spectrum of the cascading optical and electrical filters and assume the filter is the same for all subchannels. $\omega_l - \omega_j$ is the carrier frequency difference between the l_{th} and j_{th} channel, which is a multiple of the channel spacing. Because of the spectral properties of Nyquist-WDM systems, interference only happens among adjacent subchannels. Suppose the number of transmitters and receivers are the same, the l_{th} received channel contains information from the transmitted l_{th} and neighboring $(l \pm 1)_{th}$ channels. Therefore, we rewrite Eq. 4.4 to express the linear ICI from adjacent two subchannels.

$$r_l(t) \approx E_s \sum_{k=-\infty}^{\infty} s_{l,k}\, g_{l,l}(t - kT)e^{j\phi_l} + E_s \sum_{k=-\infty}^{\infty} s_{l+1,k}\, g_{l+1,l}(t - kT)e^{j\phi_{l+1}}$$

$$+ E_s \sum_{k=-\infty}^{\infty} s_{l-1,k}\, g_{l-1,l}(t - kT)e^{j\phi_{l-1}} + N(t) \qquad (4.5)$$

The ICI from neighboring channels is clearly data-pattern dependent and if the side channel information is available, it is possible to completely compensate ICI at the receiver when nonlinearities are small.

4.2 Pre-requisite Process before ICI Compensation

We exemplify the joint DPS block for the center channel ICI mitigation in Figure 4.3. It includes the CD compensation, polarization de-multiplexing, timing recovery, carrier recovery, frequency shifting, inter-channel de-skew, and ICI cancellation. Among them, the modified CD compensation, frequency shifting, and inter-channel de-skew are the essential techniques that enable the ICI cancellation. In the following sections, the three pre-required stages are discussed in detail. Finally, different ICI compensation schemes are introduced.

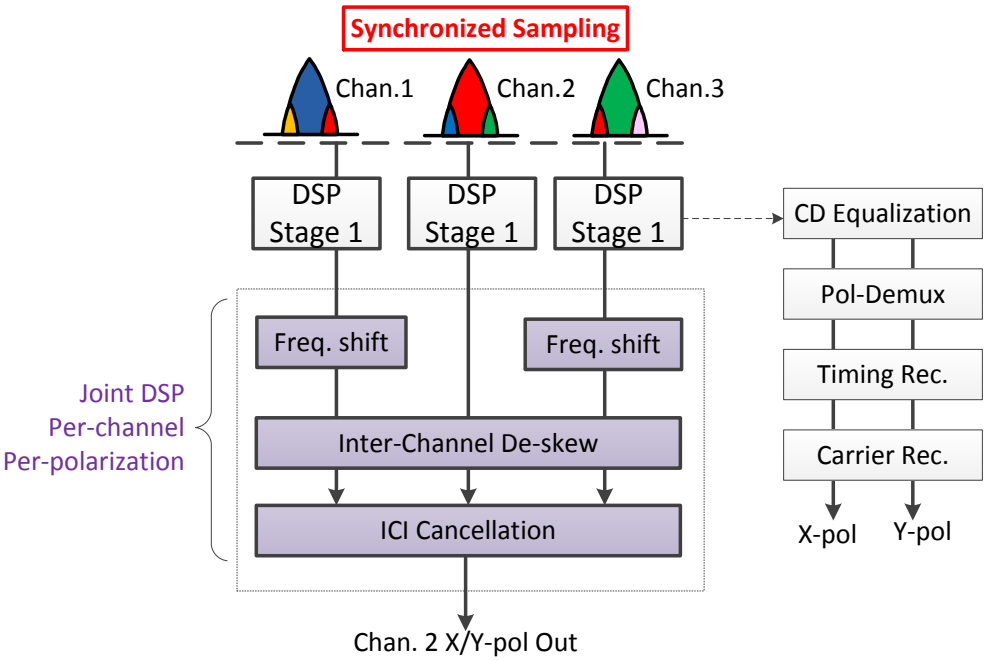

Figure 4.3. Primary elements of the superchannel WDM system with joint DSP.

4.2.1 Modified Side-channel Chromatic Dispersion Compensation

The CD is a linear transmission channel impairment that causes a parabolic phase change of the transmission signal with the frequency domain transfer function modeled as

Eq. 2.27. This phase distortion can either be compensated via inline DCF or a digital CD compensator. No extra CD compensation efforts are required at the receiver if DCF is used to completely remove the accumulated dispersion. Otherwise, the two side-subchannels undergo a modified CD compensation scheme for the center subchannel ICI compensation.

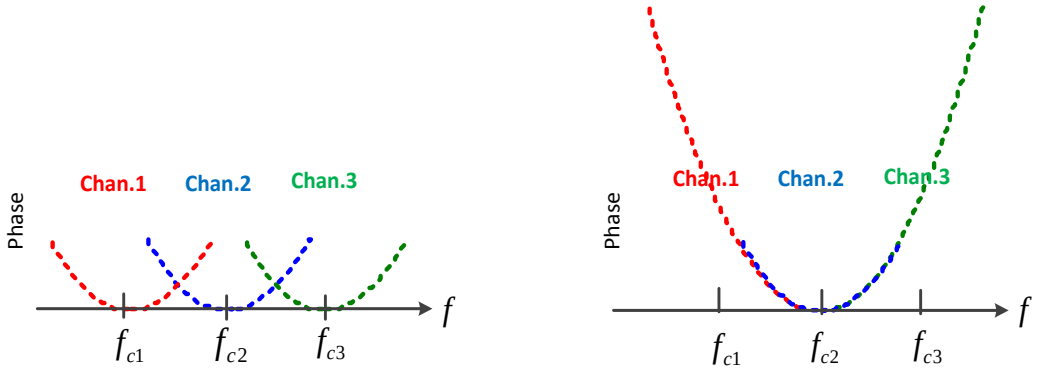

Figure 4.4. Phase of CD compensator for independent subchannel and joint multiple subchannels.

Conventional electronic CD compensation undoes the baseband signal quadrature phase change by using the transfer function in the same form as Eq. 2.27 but with negative phase sign. The phase of the CD compensator transfer function is symmetrically centered at each channel carrier frequency, Figure 4.4. However, for ICI cancellation, the phase of the overlapped band should undergo the same phase compensation [100]. From the center channel point of view, the crosstalk from adjacent channels experiences extended CD parabolic phase response. Specifically, for the center channel, the CD compensation transfer function is $H_{CD}(\omega)$ with ω spanned over the center band. The transfer functions become $H_{CD}(\omega \pm \Delta\omega)$ for the two side-channels, and $\Delta\omega$ is the

channel spacing. We have determined that this offset CD correction can be implemented during the initial CD correction without performance penalty.

4.2.2 Side-Channel Frequency Shifting

In pass band, the center channel's high frequency spectral components are partially overlapping with its neighboring channels, causing linear crosstalk. After the coherent receiver, each subcarrier is separately down converted to the baseband. The joint linear equalizer requires the two side channels' baseband spectra to be precisely shifted by the amount of channel spacing, so that the overlapped high frequency spectrum components can be aligned with the center channel for ICI cancellation, as shown in Figure 4.5.

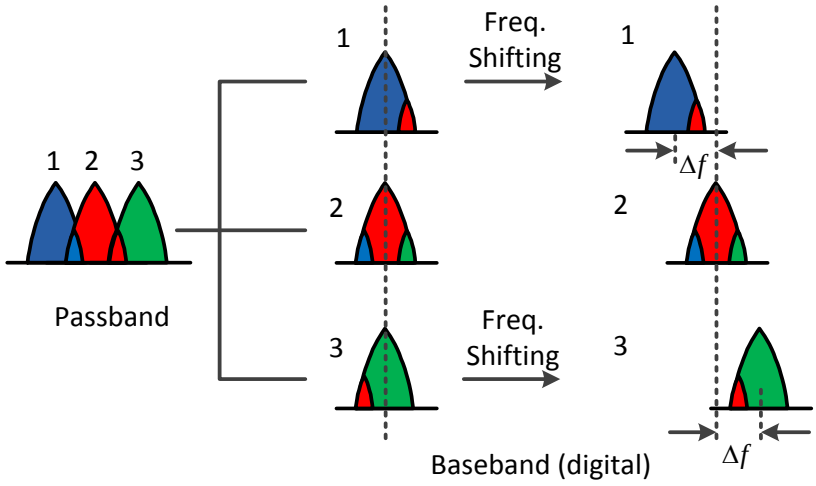

Figure 4.5. Demonstration of side subchannel's frequency shifts.

Without a frequency shifting, the side channel received signal will have a poor correlation with the center channel, limiting the performance of ICI cancellation. The side channel signal representations with frequency shift are

$$\tilde{r}_{l\pm1}(t) = r_{l\pm1}(t)e^{\pm j\Delta\omega t} \tag{4.6}$$

and the center channel remains the same $\tilde{r}_l(t) = r_l(t)$. In digital domain, frequency shifting is sample based [101].

4.2.3 Inter-Channel Skew Removal

With a frequency shifting, the spectra of the side channels are frequency aligned with the center channel. However, after de-multiplexing, relative time delay may be introduced among channels. Consequently, the ICI equalizer tap length needs to be increased to compensate the time delay, increasing the equalizer implementation complexity.

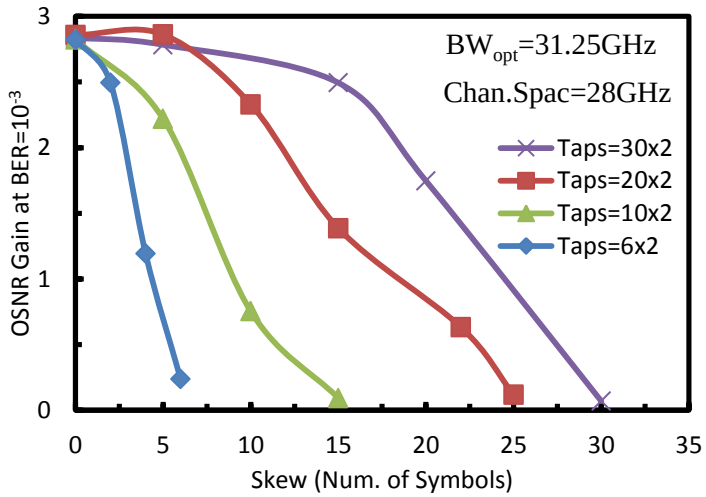

Figure 4.6. OSNR gain with ICI equalization at different time delays for 3×28 Gbaud PM-QPSK system [102].

Figure 4.6 gives an example of the OSNR gain with ICI equalization at various relative time delays for 3×28 Gbaud PM-QPSK system. The delay is represented by symbols and is introduced between the center channel and the two side channels. At zero relative delay, 2.8 dB OSNR gain is obtained with ICI compensation. The equalizer tap length grows proportionally with the increase of time delay. The relative time delay can

be retrieved using the phase information of the overlapped high frequency bands between the neighboring two channels. We denote the frequency shifted samples of channel A as $\tilde{r}_{A,n}$ and the baseband samples of channel B as $\tilde{r}_{B,n}$. Suppose channel B is delayed in time by τ with respect to channel A, the frequency domain representation of A and B is $R_A(k)$ and $R_B(k)e^{j2\pi k\tau/M}$, where M is the sequence length. The cross-product of the two spectra is

$$F_{AB}(k) = R_A^*(k)R_B(k)e^{\frac{j2\pi k\tau}{M}} \tag{4.7}$$

In the overlapped frequency bands, the two channels contain similar information $R_A^*(k) = R_B(k) = R_{AB}(k)$ therefore,

$$F_{AB}(k) = |R_{AB}(k)|^2 e^{j2\pi k\tau/M} \tag{4.8}$$

and the phase of the $F_{AB}(k)$ only contains the relative subchannel delay [103]. Define the phase of $F_{AB}(k)$ in the overlapped band as $\Delta\theta_k$ and $\Delta\theta_k = 2\pi n\tau/M$. We can obtain the time delay by estimating the slope of the phase plot, Figure 4.7. Each time three points (k_1, k_2, k_3) on the overlapped spectral band are used for gradient calculation, Figure 4.7.

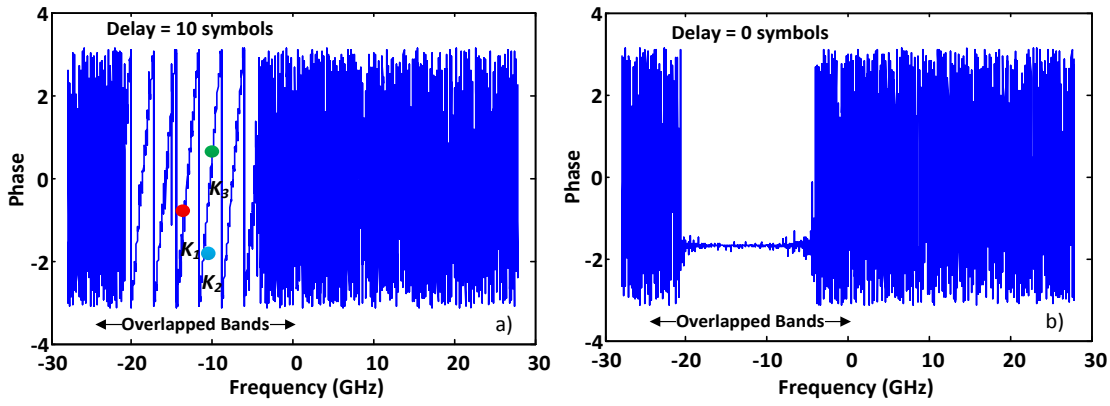

Figure 4.7. Phase of the cross-product spectra in the center subchannel band before and after removing the time delay

The relative channel spacing has to be known to the receiver for the relative frequency removal and ICI compensation. Suppose the relative channel spacing Δf is different from the expected value by δ, then

$$F_{AB}(k) = R_A^*(k)R_B(k-\delta)e^{\frac{j2\pi k\tau}{M}} \quad (4.9)$$

Because $R_A^*(k) \neq R_B(k-\delta)$, the phase of the cross product shows a noisy pattern. Meanwhile, the OSNR gain with ICI compensation decreases with the increase of δ. For 3×28 Gbaud PM-QPSK system, when the frequency offset passes 10 MHz, no OSNR gain is observed, as shown in Figure 4.8. The maintainance of relative frequency offset is necessary for ICI cancellation and thus the carriers of each subchannel are frequency locked.

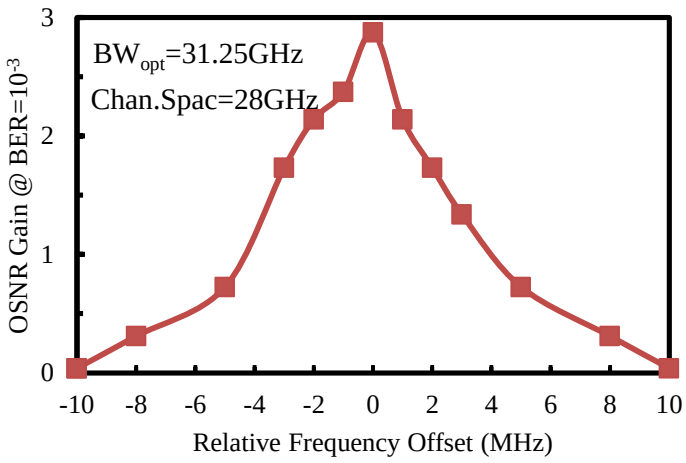

Figure 4.8. TDE-ICI equalizer OSNR gain at different relative frequency offset for 3×28 Gbaud PM-QPSK system [102].

Checking the phase of the spectral crosstalk product is a useful tool to ensure the relative frequency offset are properly set. If δ is a constant, it can be minimized by tuning

until a clear pattern of $\Delta\theta$ is observed. After correcting the relative frequency offset of the subchannels, $\Delta\theta$ of the overlapped band is computed.

4.3 Inter-Channel Crosstalk Cancellation

ICI cancellation is performed at the last stage of the demodulation. In this section, three algorithms are introduced, the DD-LMS algorithm, the MAP algorithm, and the simplified frequency domain equalization.

4.3.1 MIMO Equalizer

The DD-LMS algorithm based ICI cancellation is first introduced. The implementation of the ICI equalizer resembles a MIMO equalizer. However for ICI cancellation the filter is limited to 3×1 for the non-edge subchannel equalization (Figure 4.9) and a 2×1 for each edge subchannel. Define $\widetilde{\boldsymbol{R}}_x$ to be the discrete equalizer input vector from the x_{th} channel and $\boldsymbol{W}_x$ are the corresponding filter coefficients:

$$\widetilde{\boldsymbol{R}}_x(n) = [\tilde{r}_x(n) \quad \tilde{r}_x(n-1) \quad \tilde{r}_x(n-2) \ldots \tilde{r}_x(n-p)]^T \tag{4.10}$$

$$\boldsymbol{W}_x(n) = \left[w_{x,0}(n) \quad w_{x,1}(n) \quad w_{x,2}(n) \quad \ldots w_{x,p}(n)\right]^T \tag{4.11}$$

where p indicates the filter memory length, $\tilde{r}_x(n)$ is the discrete frequency shifted n_{th} sampling point of $\tilde{r}_x(t)$, $x \in [l-1, l, l+1]$ defined in Section 4.1. $[\,]^T$ denotes the transpose and the filter output can be written as

$$\mathrm{y(n)} = \sum_{x=l-1}^{l+1} \boldsymbol{W}_x^T(n)\widetilde{\boldsymbol{R}}_x(n) \tag{4.12}$$

The error is characterized by:

$$e(n) = d(n) - y(n). \tag{4.13}$$

The error between the desired output $d(n)$ and the filter output $y(n)$ is used to update the filter coefficients based on the LMS algorithm [80]

$$\boldsymbol{w}_x(n+1) = \boldsymbol{w}_x(n) + \mathbf{2}\delta e(n)\widetilde{\boldsymbol{R}}_x^*(n), \qquad (4.14)$$

where $[\,]^*$ is the complex conjugate and δ is the step size.

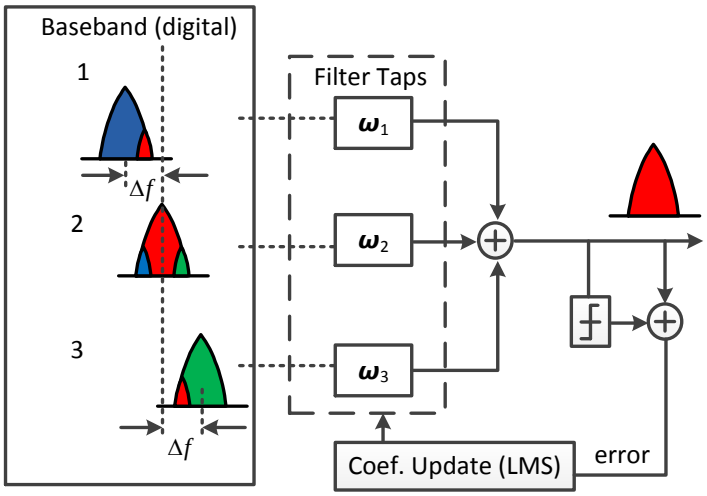

Figure 4.9. MIMO linear ICI equalization for the center subchannel.

To validate the proposed LMS-ICI algorithm in ICI compensation, we have performed extensive numerical simulations using RSOFT OptSim to generate the received electrical signals. Earlier work has demonstrated that our simulation tool has excellent correspondence with experiment. Since the channel spacing must be known or determined we examine the coherent subcarrier case. At the transmitter, phase-locked carriers are generated by a phase modulator which is driven by a sinusoidal clock with frequency equal to the desired channel spacing. The signals are shaped by a raised cosine time domain electrical filter (roll off =0.7). Each of the three phase-locked subcarriers is modulated with 112 Gbit/s PM-NRZ-QPSK. We use different pseudo-random binary sequence (PRBS) for each polarization in each subchannel. These subchannels are further spectrally shaped by 3.5th order Super-Gaussian optical filters, with various 3 dB

bandwidths. Some of the optical filter bandwidths are intentionally relaxed to evaluate the effectiveness of ICI cancellation, Figure 4.10. After filtering, these subchannels are multiplexed and launched into the transmission channel. ASE noise loading is performed at the end of transmission to evaluate BER at different OSNRs. The center channel performance is recorded.

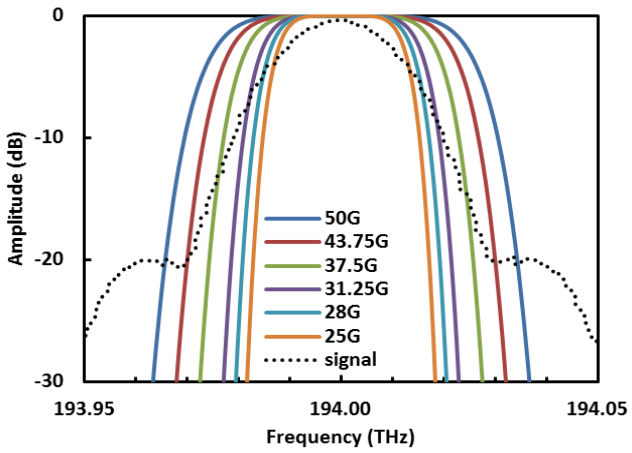

Figure 4.10. NRZ-QPSK signal spectrum before filtering (0.1 nm resolution) and the optical filter spectrum at different bandwidths [101].

Baseline performance is first evaluated for a range of transmitter optical filter bandwidth and receiver electrical filter bandwidths. The required OSNR (BER =3×10^{-3}) for the system with 15-tap ISI equalization is determined, as shown in Figure 4.10. For very narrow electrical bandwidth (less than 0.4×baud rate) there is an OSNR penalty induced by ISI effects. On the other hand, the system performance does not degrade significantly at large electrical bandwidth, in part due to the built-in anti-aliasing DSP filter, yielding a relatively large range from 17 to 22 GHz of near optimal electrical bandwidth. The optimal optical bandwidth is about 27 GHz consistent with the

expectation that it should be close to the baud rate but not exceed the 28 GHz channel spacing.

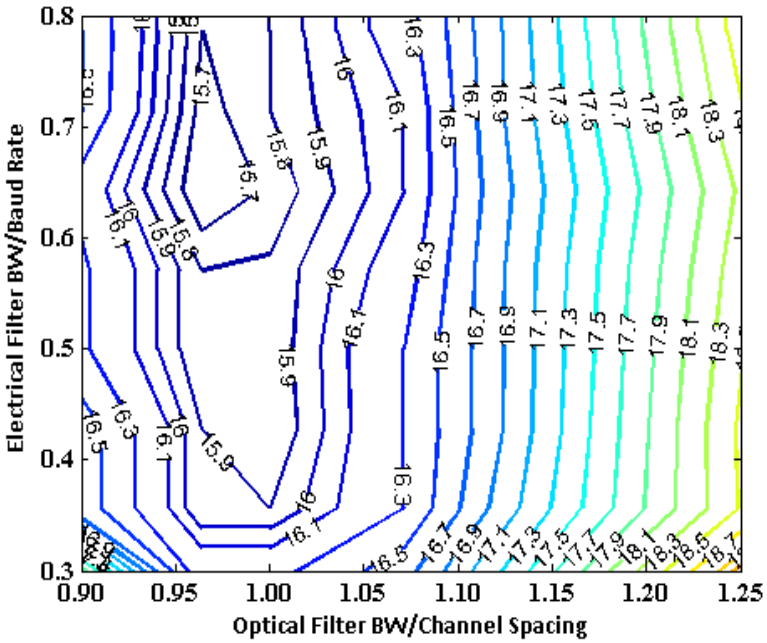

Figure 4.11. Required OSNR at BER 3×10^{-3} versus electrical and optical bandwidths. Receiver based DSP includes a 15-tap ISI equalizer (channel spacing=baud rate=28 GHz) [101].

A separate examination of the optical and electrical bandwidth behavior without ISI (or ICI) equalization reveals that the optimum optical bandwidth occurs near 30 GHz and the optimum electrical bandwidth is near 18 GHz, however the required OSNR increases by about 2.4 dB to 18.1 dB, explicitly quantifying the benefits of the ISI equalization. We note that the CMA used to de-multiplex the polarization inherently provides some ISI mitigation. However, since this must be performed prior to carrier recovery it is not as effective as a post carrier recovery equalizer. CMA equalization is also limited by the number of samples per symbols. In all subsequent simulations the

CMA equalizer remains in place and we examine various ICI and ISI methods operating at the optimal location i.e. after both timing recovery and carrier recovery.

To investigate the performance of the ICI cancellation methods, we choose an electrical filter bandwidth to be 19 GHz and examine the net optical filter bandwidth impact maintaining channel spacing to be same as the baud rate. A potential advantage of mitigating both ICI and ISI in DSP is the ability to produce excellent performance over a wide range of optical filter bandwidth, thereby alleviating the need to carefully control the net spectral shape and crosstalk. We therefore evaluate the robustness of the required OSNR versus optical filter bandwidths, Figure 4.12. With LMS-ICI compensation, an overall system improvement is obtained at all OSNR values. In this stringent test it is shown that a tap length of 15 (for all subcarriers, p =14 in Equation 4.8 is sufficient to recover much of the large induced ICI penalty. Note, the taps of the LMS-ISI equalizer are also set to 15 to achieve a fair comparison. In all cases the LMS-ICI equalizer outperforms the conventional LMS-ISI equalizer. Furthermore the ICI algorithm achieves strong mitigation under high ICI conditions (large optical filter bandwidth) for both 2- and 15-taps. The LMS-ISI algorithm achieves best gains under high ISI conditions (small optical filter bandwidth), yet the 15-tap LMS-ICI algorithm achieves best performance under all optical filtering conditions. For the LMS-ICI equalizer the specific filter bandwidth can range from 27 to 33 GHz with less than 0.25 dB change in OSNR required to achieve BER of 3×10^{-3}. This dramatically eases the need to manage the net system optical bandwidth and represents a primary benefit of implementing ICI mitigation even when optical and electrical bandwidth are near optimum.

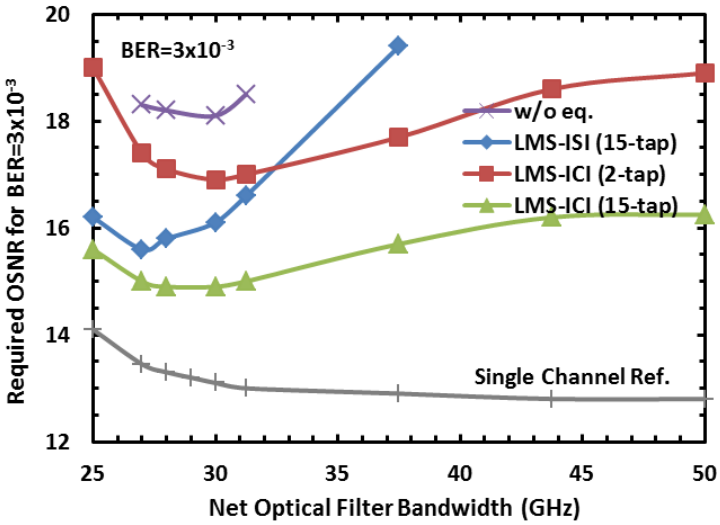

Figure 4.12. Required OSNR to achieve a BER of 3×10^{-3} at different optical filter bandwidths for system without ICI and ISI equalization and with LMS-ISI or LMS-ICI compensation techniques (channel spacing=baud rate) [101].

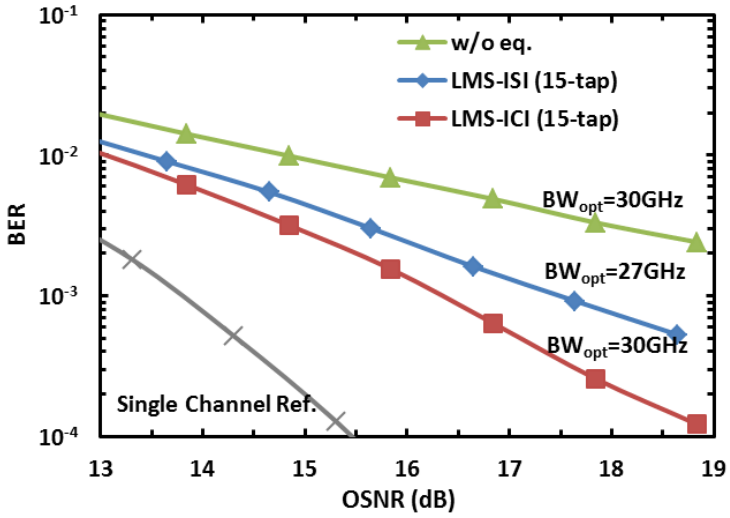

Figure 4.13. BER versus OSNR without ICI and ISI equalization and with LMS-ISI or LMS-ICI at optimal optical filter bandwidth (channel spacing=baud rate). Single channel reference is obtained with the LMS-ISI equalization [101].

The LMS-ICI algorithm performance for a system with optimal optical filter bandwidth (electrical filter bandwidth=19 GHz, and channel spacing = baud rate =28

GHz) is depicted in Figure 4.13. LMS-ICI demonstrates improved performance at all OSNRs and outperforms LMS-ISI, approaching the single channel reference.

4.3.2 MAP Based ICI Compensation

The other ICI compensation approach is based on MAP algorithm. MAP detection contains two steps: a training mode and a compensation mode. First, a QPSK training sequence associated with each possible joint constellation state $\mathcal{M} = 4^{3n}$ is transmitted several times. In the training processor at the receiver, the distorted symbols corresponding to each joint constellation state are averaged and stored as a lookup table [101].

We use $\boldsymbol{s}_m$ to represent all $\mathcal{M} = 4^{3n}$ possible transmitted symbol patterns of the three-channel system and $m \in [1, \mathcal{M}]$. $s_{l,k}$ is the k_{th} transmitted complex QPSK symbol in the l_{th} channel, Eq. 4.1.

$$\boldsymbol{s_m} = \begin{Bmatrix} s_{l-1,k} & s_{l-1,k+1} & \cdots & s_{l-1,k+n-1} \\ s_{l,k} & s_{l,k+1} & \cdots & s_{l,k+n-1} \\ s_{l+1,k} & s_{l+1,k+1} & & s_{l+1,k+n-1} \end{Bmatrix} \tag{4.15}$$

The MAP-ICI tap length is the sum of the number of taps for each channel, generally $3n$. Suppose the received baseband signals of the three subchannels are $r_l(t)$ and $r_{l\pm1}(t)$, Eq. 4.5, and let $r_{l,k}$ denote the optimal sampling of the k_{th} received QPSK symbols in the l_{th} channel, the three-channel received symbols with optimal sampling are written as

$$\boldsymbol{r} = \begin{Bmatrix} r_{l-1,k} & r_{l-1,k+1} & \cdots & r_{l-1,k+n-1} \\ r_{l,k} & r_{l,k+1} & \cdots & r_{l,k+n-1} \\ r_{l+1,k} & r_{l+1,k+1} & & r_{l+1,k+n-1} \end{Bmatrix} \tag{4.16}$$

In the compensation mode, based on the observation of the received $\boldsymbol{r}$, we want to choose the most likely combination from a set of possible transmission symbols $\boldsymbol{s}_m, m \in [1, \mathcal{M}]$,

so that the probability of $P[\boldsymbol{s}_m \,|\boldsymbol{r}]$ is maximized. The optimal detection scheme is known as the MAP rule [104]

$$\tilde{\boldsymbol{s}} = \arg \max_{1 \le m \le \mathcal{M}} P[\boldsymbol{s}_m \,|\boldsymbol{r}] \tag{4.17}$$

The Euclidean distance between optimal sampling of the received symbols and the distorted data stored in the lookup table is used to calculate the MAP probability. The data pattern $\boldsymbol{s}_m$ corresponding to the highest correlation or the minimum Euclidean distance is chosen to be the optimal decision. Therefore, the decision can be made for $r_{l,k}$. Lastly we note that the 15-tap LMS-ICI methods perform nearly as well as the 6-tap MAP.

The 3-tap and 6-tap MAP-ICI cancellation methods are applied to the 3×28 GBaud PM-NRZ-QPSK system with the same setup as in section 4.5.1. The "3-tap" means that the lookup table contains only the k_{th} received symbol of the three channels l_{th} and $l \pm 1_{th}$. The "6-tap" includes the k_{th} and $k + 1_{th}$ received symbols of the three channels. At a large optical filter bandwidth, ICI is dominant and the conventional ISI adaptive equalizer cannot effectively mitigate this inter-channel interference. In contrast, even the 3-tap MAP-ICI canceller readily compensates ICI at large optical filter bandwidth, outperforming the 15-tap ISI equalizer for optical filter bandwidth greater than 31 GHz, Figure 4.14. However, when the signal spectrum bandwidth narrows, the 3-tap MAP equalizer is not sufficient to compensate the narrow filtering induced ISI. The ICI of neighboring channels makes the center channel Nyquist pulses no longer orthogonal to each other, creating additional ISI-like effects. By introducing proper memory size, both ICI, ISI, and ICI induced ISI-like effects can be compensated. For example, when the MAP tap length is increased to six, an overall performance

improvement that is relatively insensitive to optical filter bandwidth is observed. Importantly the 6-tap MAP equalizer yields performance within 2 dB of the single channel performance for optical filter bandwidth from 27 to 37.5 GHz. Furthermore, using a narrow optical filter bandwidth to reduce ICI and incur slightly more ISI the 15-tap LMS-ISI equalizer does not perform as well as the 6-tap MAP-ICI equalizer. The minimum BER occurs at different optical filter bandwidth for different compensation techniques. The conventional LMS-ISI equalizer is optimum at the narrowest optical filter bandwidth of about 27 GHz and the 3-tap MAP-ICI canceller is optimized near 31 GHz.

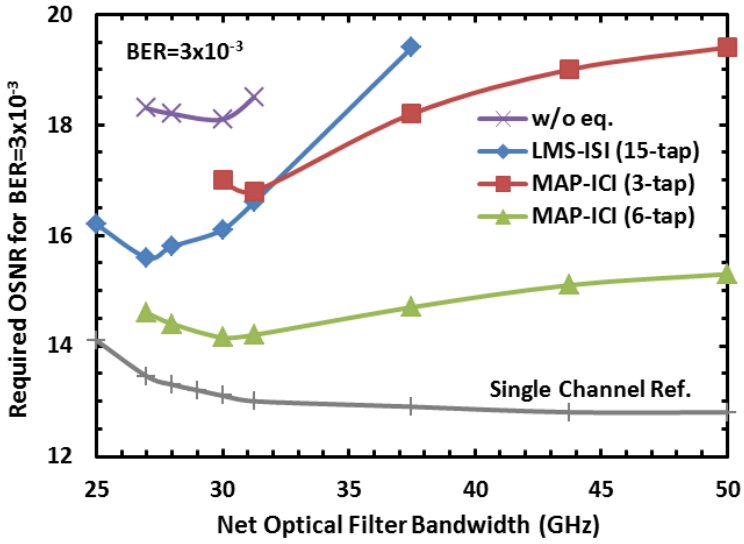

Figure 4.14. Required OSNR to achieve a BER of 3×10^{-3} at different optical filter bandwidths for system without ICI and ISI equalization and with LMS-ISI or MAP-ICI compensation techniques (channel spacing=baud rate) [101].

The MAP-ICI algorithm performance for a system with optimal optical filter bandwidth is depicted in Figure 4.15. The MAP-ICI cancellation recovers over 5 dB

OSNR penalty for the near optimum 30 GHz optical filter at a BER of 10^{-3} and outperforms the LMS-ISI equalizer by 2.5 dB.

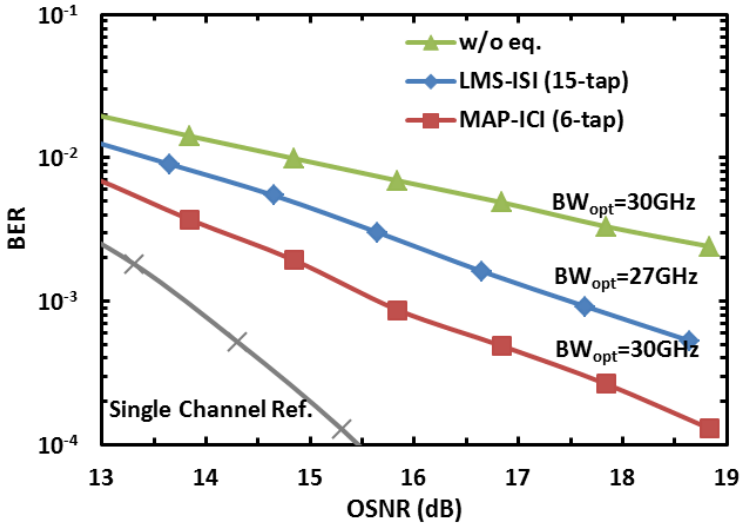

Figure 4.15. BER versus OSNR without ICI and ISI equalization and with LMS-ISI or MAP-ICI at optimal optical filter bandwidth (channel spacing=baud rate). Single channel reference is obtained with the LMS-ISI equalization [101].

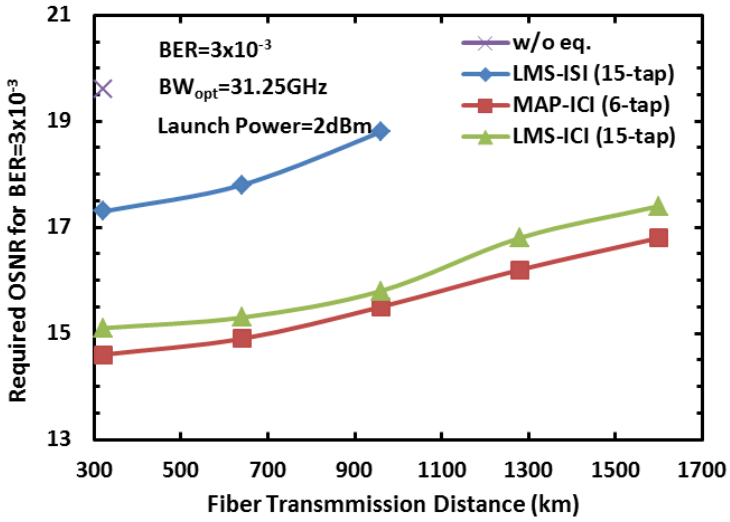

Figure 4.16. Required OSNR to achieve a BER of 3×10^{-3} system without ICI and ISI equalization and with different types of compensation techniques after different transmission distance (channel spacing=baud rate) [101].

Propagation through multiple fiber spans results in additional challenges for any receiver based ICI canceller including residual chromatic dispersion (after CD compensation) and nonlinear effects, Figure 4.16. We have examined performance at BER=3×10^{-3} after propagation through multiple spans of SSMF with the optical filter bandwidth set at 31.25 GHz and launch power at 2 dBm, which insures some nonlinear penalty. The SSMF has an attenuation of 0.2 dB/km and a nonlinear coefficient of 1.165 /km/W. In each span, the EDFA optical amplifier with 6 dB noise figure compensates span loss. The transmitter laser and LO laser are assumed to be perfectly aligned in the frequency domain both with a linewidth of 0.1 MHz. Because of nonlinearity the required OSNR increases with transmission distance. Compared to the system without ICI and ISI compensation, the LMS-ISI equalizer offers a 2 dB gain to achieve a BER of 3×10^{-3} and ICI compensators offer a 4 dB gain. With a 6-tap MAP canceller, a further 0.5 dB gain is observed. Importantly, at a long transmission distance where nonlinear penalties are apparent in the no equalizer case, both MAP and LMS ICI cancellers yield increased benefits demonstrating their ability to compensate nonlinear penalties.

Table 4.1.Number of real additions and multiplications for LMS-ISI, LMS-ICI and MAP-ICI (p is the tap number. L is the sequence length).

Equalizers	Additions	Multiplications
LMS-ISI	$(8p+4)L$	$(8p+8)L$
LMS-ICI	$(24p+12)L$	$(24p+24)L$
MAP-ICI	$(3p4^p-1)L$	$4p4^pL$

The computational complexities of MAP-ICI and LMS-ISI and LMS-ICI vary significantly. For comparison we tabulate the number of real additions and multiplications for each compensation method, Table 4.1. p is the tap number. L is the sequence length. The 15-tap LMS-ICI requires $372L$ additions and $384L$ multiplications whereas 6-tap MAP-ICI requires $73727L$ additions and $98304L$ multiplications.

4.3.3 Simplified Frequency Domain ICI Compensation

Conventional LMS-TDE (time domain equalizer) can be implemented by block-LMS to enable parallel processing and hence improves computational efficiency. Recently, it has been demonstrated that the frequency domain implementation of block-LMS-TDE based on overlap-save method can further reduce the complexity even at small tap length and are capable of operating at multiple samples per symbol [105]. The frequency domain implementation is preferred if there is large relative time delay between each sub-channel and large tap length is required. In this work, we propose a method which further reduces the computation complexity of the frequency domain ICI equalizer.

The principle of the frequency domain adaptive equalizer is described as the following. For a 50% overlap, the $T/2$ *-spaced* frequency domain equalizer (FDE) overlap-save method processes input block of $2P = 4L$ samples and delivers L output samples, where $2L$ is the TDE filter tap length and is also the number of overlapping samples between two consecutive blocks. A straightforward implementation involves a $2P$-inverse fast Fourier transform (IFFT) of the FDE output $\boldsymbol{Z}$ and followed by a time domain down sampling to keep the samples at maximum eye opening. An alternative method is to perform the down sampling in frequency domain [105]. Let $\boldsymbol{Z} =$

$(Z_0, \cdots, Z_{2P-1})$ and the corresponding time domain sequence is $\boldsymbol{z} = (z_0, \cdots, z_{2P-1})$. We denote the even and odd sample of $\mathbf{z}$ by $\boldsymbol{z_e} = (z_0, z_2 \cdots, z_{2P-2})$ and $\boldsymbol{z_o} = (z_1, z_3 \cdots, z_{2P-1})$. The DFT of $\boldsymbol{z_e}$ and $\boldsymbol{z_o}$ is $\boldsymbol{Z_e} = (Z_{e,1}, \cdots, Z_{e,P-1})$ and $\boldsymbol{Z_o} = (Z_{o,1}, \cdots, Z_{o,P-1})$, Eq. 4.18-4.19. The fast Fourier transform (FFT) of even and odd samples of 2P-input $\boldsymbol{y}$ can be calculated in a similar manner. The even and odd filter coefficients $\boldsymbol{C_e} = (C_{e,1}, \cdots, C_{e,P-1})$ and $\boldsymbol{C_o} = (C_{o,1}, \cdots, C_{o,P-1})$ are updated separately using the same error, which is calculated by taking the difference between the L-length optimal output and the decision device. The even and odd coefficients $\boldsymbol{C_e}$ and $\boldsymbol{C_o}$ need to be combined to form a $2P$-length FD weight vector $\boldsymbol{C} = (C_0, \cdots, C_{2P-1})$ as in Eq. 4.20

DFT even and odd samples ($0 \leq l \leq P-1$):

$$Z_{e,l} = (Z_l + Z_{l+P})/2 \tag{4.18}$$

$$Z_{o,l} = (Z_l e^{\frac{j2\pi l}{2P}} + Z_{l+P} e^{\frac{j2\pi(l+P)}{2P}})/2 \tag{4.19}$$

Combine even and odd coefficients:

$$C_l[k] = \begin{cases} C_{e,l}[k] + C_{o,l}[k] e^{-\frac{j2\pi l}{2P}}, 0 \leq l \leq P-1 \\ C_{e,l-P}[k] + C_{o,l-P}[k] e^{-\frac{j2\pi l}{2P}}, P \leq l \leq 2P-1 \end{cases} \tag{4.20}$$

Since only high frequency band of subchannels are overlapped, we further reduce the computation complexity by setting the side-subchannel spectra in the non-overlap band to zero. We denote the ratio of the number of non-zero coefficients to the FD weight length ($2P$) by M and find that more than half of the weights can be set to zero without performance degradation. Therefore, the corresponding coefficients $\boldsymbol{C}$ and output $\mathbf{Z}$ for side-subchannels are also zeros and thus the implementation of Eq. 4.18-20 and the gradient constraint process can be simplified. Take M =0.5 and one side sub-channel as an example, half of the coefficients vector $\boldsymbol{C}$ are zero, and thus Eq. 4.20 can be

simplified. The product computation complexity of $\boldsymbol{C}$ and FFT output $\boldsymbol{Y}$ for side channels is reduced by half. The example of the implementation block diagram is shown in Figure 4.17.

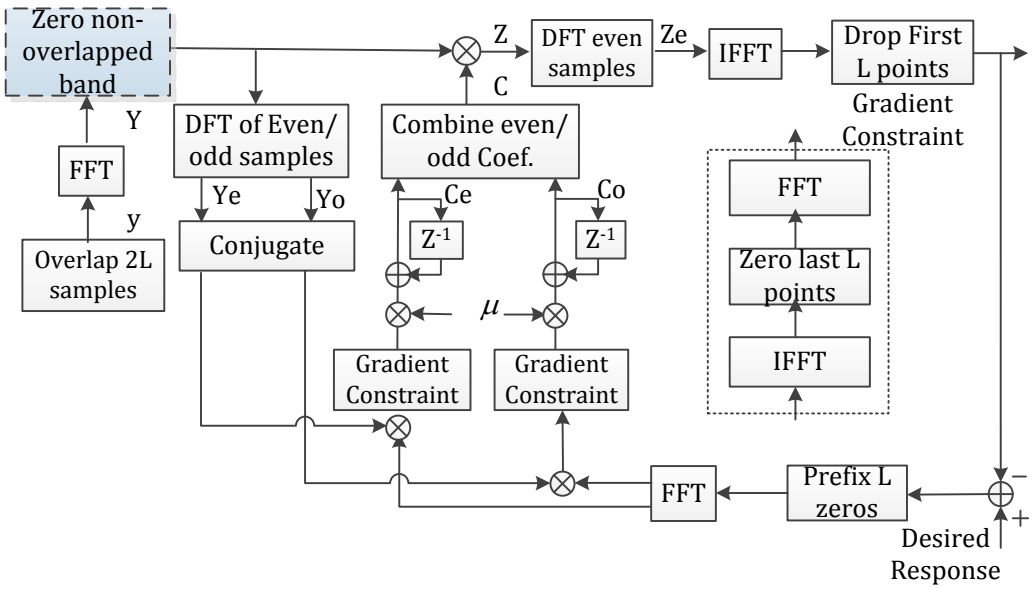

Figure 4.17. Frequency domain adaptive equalization block diagram (highlighted block is for side subchannels).

Simulation results are used to demonstrate the advantages of the proposed FDE for ICI cancellation for a 3×28 Gbaud PM-QPSK system. The receiver DSP block includes: CD compensation, CMA based 7-tap equalizer for polarization demultiplexing, the square and filtering timing recovery, Viterbi-Viterbi carrier recovery, $T/2$-*spaced* standard LMS-ICI or simplified block frequency domain equalizer for ICI cancellation. The TDE tap lengths are chosen to be 20 to cover both ICI and ISI.

In Figure 4.18, with the narrowing of channel spacing, severe crosstalk is introduced and each of the ICI canceller methods show more than 5 dB OSNR gain when

channel spacing equals to the baud rate. The FDE with $M = 1$ and $M = 0.5$ shows comparable performance with the LMS-ICI. To demonstrate the algorithms are valid at high spectral efficiency region, the channel spacing is set equal to the baud rate and optical filter bandwidth is varied, Figure 4.19. When the optical filter bandwidth is less than 33GHz some of the crosstalk is suppressed and M can be further reduced to 0.3 with performance equal to $M = 1$ and within 2 dB of the single channel no ICI result. With the presence of a large amount of crosstalk, slightly performance degradation at $M = 0.3$ presents due to the factor that the overlapped band is larger.

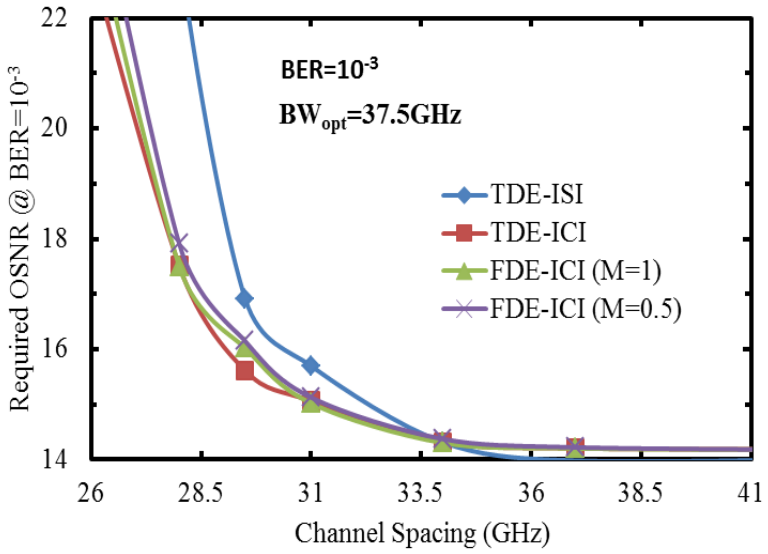

Figure 4.18.Required OSNR at BER=10^{-3} versus channel spacing with TDE/FDE for ISI or ICI cancellation (Optical filter bandwith is 37.5 GHz).

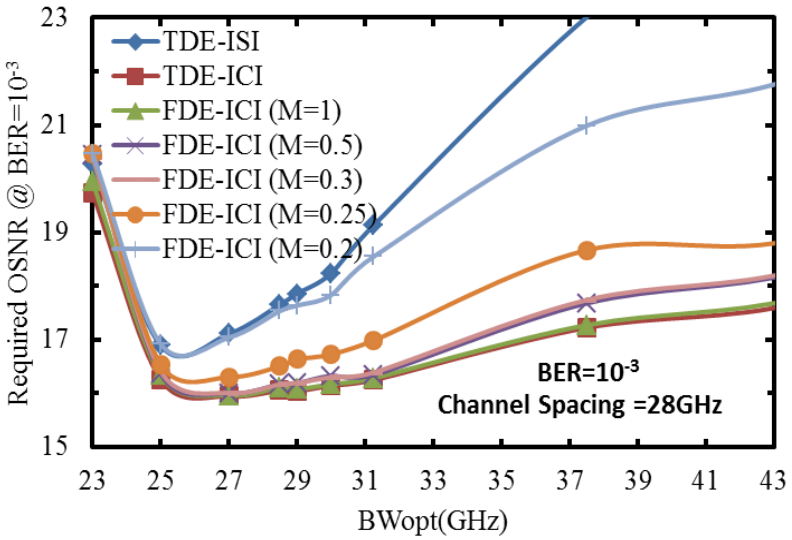

Figure 4.19. Required OSNR at BER=10^{-3} versus optical filter bandwidth with TDE or FDE for ISI or ICI cancellation (Channel spacing is 28 GHz).

The transmission system consists of multiple spans of SSMF with attenuation of 0.2 dB/km and nonlinear coefficient of 1.165 /km/W. In each span, the EDFA optical amplifiers with 6dB noise figure compensate span loss. With TDE/FDE ICI cancellation, ~2 dB OSNR gain is observed for 640 km transmission, Figure 4.20.

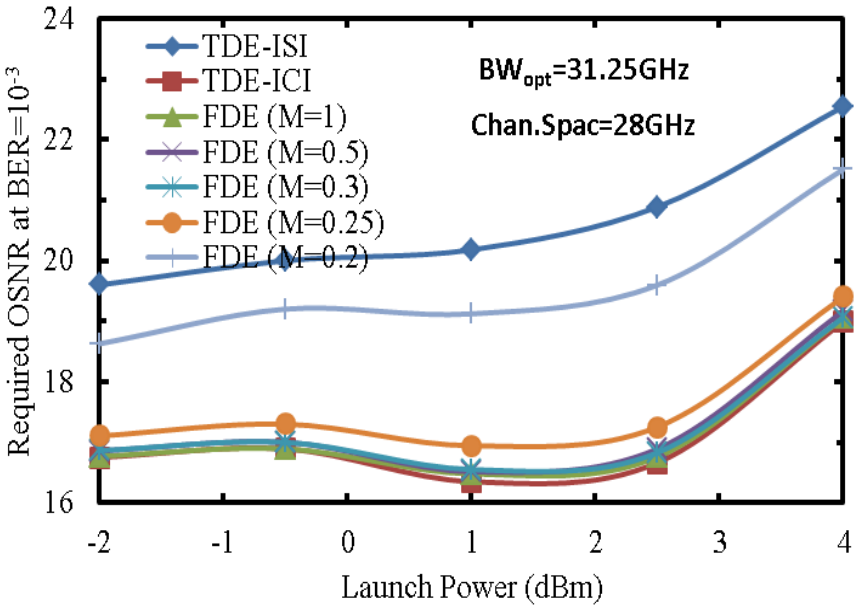

Figure 4.20. Required OSNR at BER=10^{-3} versus launch power with TDE/FDE for ISI or ICI cancellation (optical filter bandwidth is 31.25 GHz and channel spacing is 28 GHz).

4.4 Viterbi-Viterbi Algorithm based Joint Carrier Recovery

If the carrier of each subchannel is frequency and phase locked, we may jointly compensate the phase of each subchannel. The narrowly spaced phase locked carriers are generated by phase modulating a single laser source, Figure 4.21. The driving frequency equals to the channel spacing. The output of the modulator can be analytically represented by

$$x(t) = \cos(\omega_c t + A \cdot \cos(\omega_m t) + \phi)$$

$$= J_0(A)\cos(\omega_c t + \phi) + J_1(A)\cos\left((\omega_c + \omega_m)t + \frac{\pi}{2} + \phi\right)$$

$$- J_1(A)\cos\left((\omega_c - \omega_m)t + \frac{\pi}{2} + \phi\right) + J_2(A)\cos((\omega_c + 2\omega_m)t + \pi + \phi)$$

$$- J_1(A)\cos((\omega_c - 2\omega_m)t + \pi + \phi)$$

$$+ \cdots \qquad (4.21)$$

where ω_c is the angular frequency of the carrier, $\omega_m$the driving tone and ϕ is the phase of the carrier. The first three terms represent the carriers of the three sub-channels. The amplitudes of the carriers are controlled by the power of the driving signal and $J_n(A)$ is the Bessel function. Each sub-carrier is separated and amplified. The phase of the subchannel has the same trend with a constant $\pi/2$ offset between the ω_c and $(\omega_c \pm \omega_m)$ tones. Therefore, it is possible to jointly extract the phase of the three sub-carriers during the demodulation process.

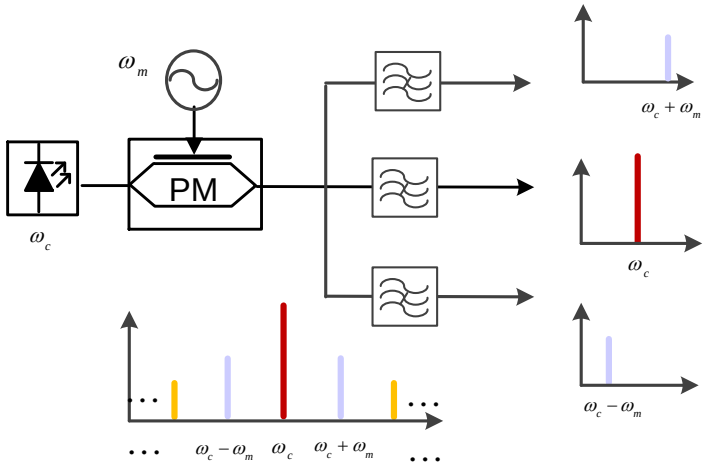

Figure 4.21. Generation of the phase locked sub-carriers based on Bessel expansion.

The sampling of each sub-channel should be synchronized, so that the adjacent channel information can be aligned with the desired channel for joint DSP. Likewise, to make the joint carrier phase recovery possible, the generation of LO lasers should follow the same procedure as the transmitter lasers. The proposed join DSP block diagram is shown in Figure 4.22. We use three channels for demonstration and this configuration can be scaled to multiple channels. After ADC, the data for each channel goes through the electrical dispersion compensation, polarization demultiplexing, and timing recovery independently. Then, the synchronous information from three channels is fed into the joint carrier phase recovery block.

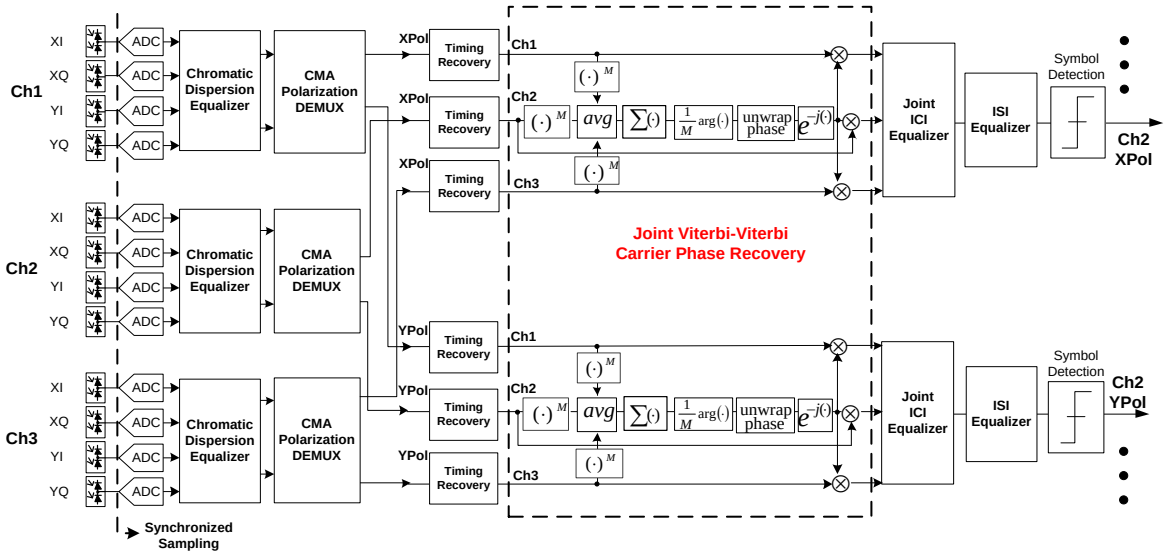

Figure 4.22. Joint Viterbi-Viterbi carrier phase recovery block diagram.

The cross channel joint carrier phase estimation is applicable in carrier locked systems. The procedure is developed based on the Viterbi-Viterbi algorithm and the detailed principle can be explained as follows. The incoming complex low pass signal from each channel (both X-pol and Y-pol) is first raised to the M^{th} power to remove data dependencies. Then, the three data streams are averaged. For narrow linewidth lasers, the laser phase noise can be considered to be slowly varying with time. Therefore, we sum several symbols to remove additional noise. After that, the argument of the output is divided by M and the phase is unwrapped. Finally, the jointly estimated phase error is used to correct the phase of each sub-channel. The merits of the joint carrier phase estimation lie in two aspects: first, by performing additional averaging of the side channels, more ASE noise can be removed. Second, since the two outside channels always have less crosstalk than the center channel, we found that we can use only the phase information from two outside channels to obtain a more accurate phase estimation.

To investigate the effectiveness of the proposed joint signal processing concept in the super-channel WDM systems, we perform numerical simulations for a three-channel 28 Gbaud PM-NRZ-QPSK system using RSoft OptSim. At the transmitter, the QPSK signals are modulated onto several phase locked subcarriers. These sub-channels are spectrally shaped by 3.5^{th} order Super-Gaussian optical filter, with a 38 GHz 3 dB bandwidth. At the receiver, the incoming signals are separated and fed into the corresponding coherent receivers for O/E conversion. The circulation loop test consists of 8×80 km Allwave fibers. For simplicity, inline dispersion compensation is used to guarantee that the phase noise remains the same among sub-channels. For the electronic dispersion compensation case, the variation of group velocity delay between each channel needs to be taken into consideration. The linewidth of the laser is fixed at 0.1 MHz and the transmitter and LO lasers are assumed to be perfectly aligned.

Figure 4.23.a shows the BER versus OSNR before and after joint carrier phase recovery with different channel spacing. We observed a consistent benefit at various channel spacing. It is because the more ASE has been averaged out. Figure 4.23.b shows the span test results for a three-channel case, in all cases the joint carrier recovery demonstrates an improved performance. In the nonlinear regime (2 dBm) where the nonlinear phase noise is large, the joint Viterbi-Viterbi algorithms can make the system less vulnerable to phase slip.

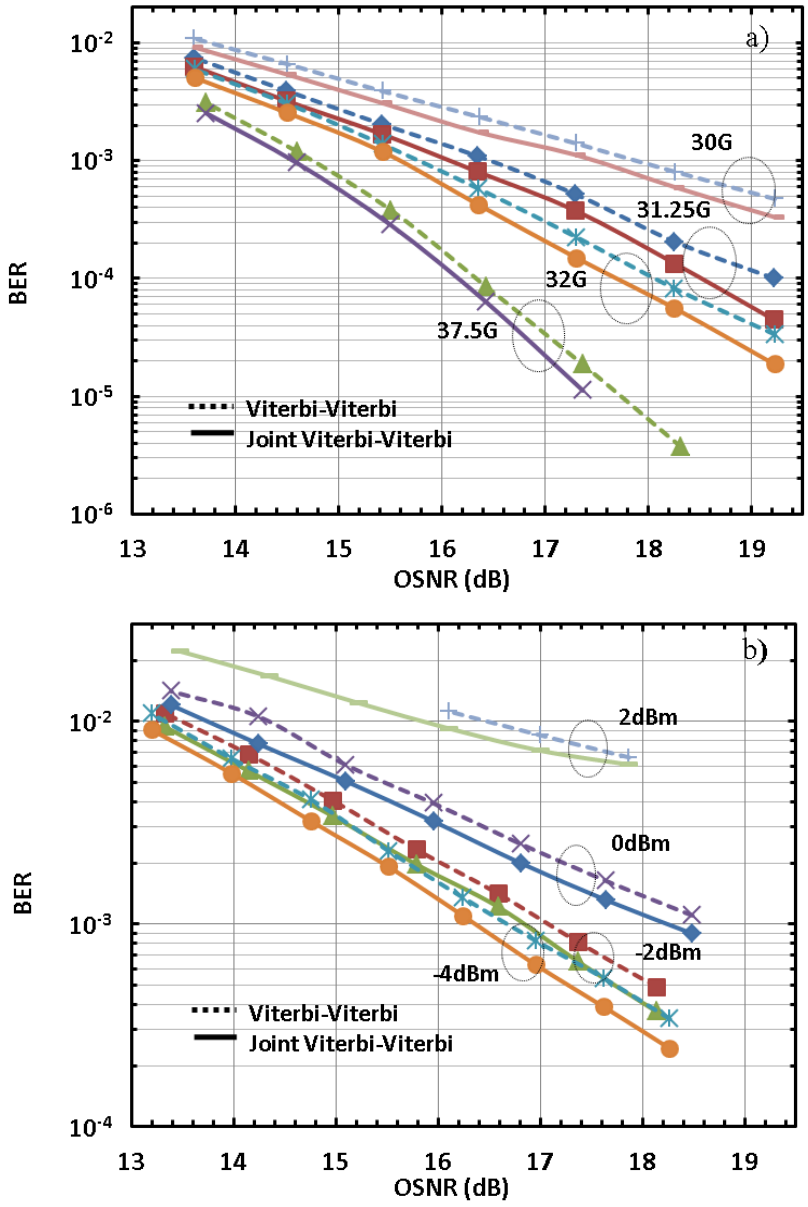

Figure 4.23. a) BER versus OSNR with and without joint carrier phase recovery at different channel spacing. b) BER versus OSNR with and without joint carrier phase recovery at 31.25 GHz channel spacing after 8×80 km fiber propagation.

4.5 Chapter Summary

As DWDM systems move to tighter channel spacing for higher capacity ICI is likely to incur a significant penalty. We have proposed and demonstrated a new "super-

channel" receiver design and three ICI cancellation schemes that effectively mitigate ICI penalties.

In the proposed "super-receiver" architecture, each channel is synchronously sampled at the receiver such that information from each channel can be aligned and used for further joint DSP. Exploiting this new receiver structure, we evaluated three ICI cancellation algorithms based on the MAP detection, the linear time domain, and the simplified frequency domain adaptive ICI equalizer. Meanwhile the necessary DSP procedures that enable the ICI compensation have been demonstrated. Simulation results have shown that all of the proposed algorithms outperform the conventional LMS-ISI equalizer, successfully mitigating the impairments caused by the ICI and dramatically reducing the need to manage the net optical system bandwidths. Lastly, we demonstrated that even with near optimal optical bandwidths receiver based ICI cancelling yields significant benefits, suggesting that non-ideal Nyquist-WDM superchannel designs may benefit from the methods demonstrated here.

MAP-ICI demonstrated slight better performance than the LMS-ICI both in linear and nonlinear regimes. The frequency domain ICI compensation can be simplified without sacrificing the performance.

In a system with phase locked carriers, the joint carrier recovery can be used, which estimated the carrier phase error using the baseband signal information from all the subchannels. The proposed approach has demonstrated improved BER performances both in linear and nonlinear regimes compared to a system with a single channel carrier phase recovery and is more tolerant to carrier phase slip.

CHAPTER 5

GAUSSIAN NOISE MODEL BASED IN-BAND CROSSTALK ANALYSIS

Transmission penalties for long haul optical transmission systems primarily originate from ASE noise accumulation; Kerr effect induced nonlinear interference (NLI); ISI due to hardware bandwidth limitations; ICI from neighboring transmission channels; and in-band crosstalk primarily caused by finite isolation of the ROADMs.

Among the mentioned penalties, the ASE noise impairment can be accurately modeled and measured. The conventional OSNR directly leads to the prediction of the BER given the ASE noise power. We note, though, the challenges associated with accurate measurements of the OSNR in systems with Nyquist or closely spaced channels. With respect to NLI, the direct computation of nonlinear propagation, via the nonlinear Schrodinger equation (NLSE), in dispersion managed (DM) links is unwieldy and the performance is hard to predict [46]. Owing to the advent of coherent detection with DSP, links with the uncompensated chromatic dispersion (UT) have become a viable and preferred option. Sufficient accumulated CD drastically distorts the signal pulse shapes in the time domain, significantly changing the signal propagation, in contrast to DM systems, rendering the highly dispersed signals as noise-like [44-46, 106-108]. Consider common QPSK or QAM signals: the histogram of the received signal amplitude (in-phase or quadrature) takes on statistically independent zero-mean Gaussian distributions after several kilometers of fiber transmission [44, 46, 106, 107]. Even after receiver DSP, the statistical distribution of each of the received constellation points appears to be

Gaussian. Therefore, it is possible to model the NLI as excess additive Gaussian noise, which can be added in a root mean square (RMS) fashion to the ASE noise. The conventional OSNR can be recalibrated to account for nonlinear effects and leveraged as a performance prediction. The ISI and ICI Gaussian contributions have been investigated using the statistical distribution of the constellation points under both impairments [46]. Similarly, both the ISI and ICI impairments can be treated as Gaussian noise and added to the ASE noise and NLI noise in a RMS fashion for performance prediction. Generally the computation of the ISI and ICI requires the back-to-back system sensitivity calibration with and without the presence of the two penalties.

In-band crosstalk is an important linear impairment that arises from the add-drop element in ROADM-enabled DWDM system. The in-band crosstalk usually varies in power and shape, and may cause significant performance degradation [39-42]. Thus, it is desirable to find a way to characterize the in-band crosstalk induced penalty and be able to quantitate the in-band crosstalk noise power and add it the GN model.

So in the following section, we will incorporate the in-band crosstalk noise to the Gaussian noise model and use the generalized OSNR to predict the performance. The nonlinear parametric interference between the crosstalk and the signal will be studied. The following discussions are based on a PM-QPSK system.

5.1 The Gaussian Noise Model

The GN model has been extensively used for nonlinearity assessment in DUM optical links. In this work, we extend the GN model to capture the in-band crosstalk penalty both in the linear and nonlinear regimes. We first review the relation between BER and the OSNR.

Assuming linear propagation in an ideal, ASE-noise-limited optical channel and neglecting PDL, the BER can be expressed as a function of $OSNR_{ASE}$ for any coherent system exploiting QPSK or QAM modulation, including PM systems [46]. Specifically, for PM-QPSK system, it is:

$$BER = \boldsymbol{\Phi}(OSNR_{ASE}) = \frac{1}{2} erfc\left(\sqrt{\frac{B_{ref}}{2R_s} OSNR_{ASE}}\right) \quad (5.1)$$

Where $erfc(\cdot)$ is the error function [104]. R_s is the transmission signal baud rate and B_{ref} is the 0.1 nm ASE noise bandwidth. $OSNR_{ASE}$ is the optical signal-to-ASE noise ratio:

$$OSNR_{ASE} = \frac{P_{ch}}{P_{ASE}} \quad (5.2)$$

P_{ch} is signal transmission power per channel. P_{ASE} is the ASE noise power defined over the 0.1 nm bandwidth. The ASE noise in the transmission link comes from the inline EDFA. Given the number of transmission spans, N_s, EDFA gain, G, and EDFA noise figure, N_F, the ASE noise power from the amplifiers is estimate by [107]:

$$P_{ASE,amp} = N_s G \hbar \omega N_F B_N \quad (5.3)$$

Where $\hbar$ is Plank's constant and ω is the reference frequency. If considering the loaded ASE noise at the end of the transmission, P_{ASE} is the total ASE noise from the inline amplifiers and the added ASE noise power, $P_{ASE,added}$ (0.1 nm bandwidth):

$$P_{ASE} = P_{ASE,amp} + P_{ASE,added} \quad (5.4)$$

Invoke the two assumptions that both the crosstalk and nonlinear noise can be modeled as additive Gaussian noise, statistically independent of ASE noise, a generalized $OSNR_{tot}$

can be defined in Eq. 5.5. With the generalized $OSNR_{tot}$, the BER under the impairments of nonlinearity and crosstalk is expressed as $\boldsymbol{\Phi}(OSNR_{tot})$.

$$OSNR_{tot} = \frac{P_{ch}}{P_{ASE} + P_{effXT} + P_{NLI}} \tag{5.5}$$

P_{effXT} is the effective crosstalk noise power that is actually causing the performance degradation and is quantitatively the same as the ASE noise. P_{NLI} is the nonlinear noise power caused by both the transmission signal and the crosstalk. It is computed from the nonlinear PSD generated using the FWM approaches. We consider the case when the nonlinear noise generated in each span is accumulated in each span incoherently. The corresponding nonlinear PSD after transmission through one span of fiber is: $G_{ss,NLI}(f)$ [107]:

$$G_{ss,NLI}(f) = \frac{16}{27}\gamma^2 \iint_{-\infty}^{\infty} G_{tx}(f_1)\, G_{tx}(f_2) G_{tx}(f_1 + f_2 - f) \cdot \left| \frac{1 - e^{-2\alpha L_S + i4\pi^2 \beta_2 L_S (f_1 - f)(f_2 - f)}}{2\alpha - i4\pi^2 \beta_2 (f_1 - f)(f_2 - f)} \right|^2 df_1 df_2 \tag{5.6}$$

$G_{tx}(f)$ is the transmission PSD. For the system without crosstalk addition, we denote the transmitted PSD as $S(f)$. Then $G_{tx}(f)$ equals $S(f)$ The nonlinear PSD amplitude is directly proportional to the span length, L_s, and decreases with increasing attenuation, α, or dispersion, β_2. The $\frac{1-e^{-2\alpha L_S + i4\pi^2 \beta_2 L_S (f_1 - f)(f_2 - f)}}{2\alpha - i4\pi^2 \beta_2 (f_1 - f)(f_2 - f)}$ term is akin to the FWM efficiency. The total nonlinear PSD of the signal after N_s span transmission is in Eq. 5.7.

$$G_{Sig,NLI}(f) = G_{ss,NLI}(f) \cdot N_s \tag{5.7}$$

The nonlinear power is usually defined as the integration of the nonlinear PSD $G_{sig,NLI}(f)$, within the 0.1 nm bandwidth, B_N, similar to the conventional ASE noise definition. This is likely to be true when the signal spectrum is flat, for example, Nyquist

shaped signals. Otherwise, we may need to consider the nonlinear power in larger bandwidth.

$$P_{sig,NLI} = \int_{-B_N/2}^{B_N/2} G_{Sig,NLI}(f)df \tag{5.8}$$

For the system with crosstalk addition, the nonlinear PSD is generated similarly as in Eq. 5.6. Denote the crosstalk PSD as $X(f)$, the total transmitted PSD becomes $G_{tx}(f) = S(f) + X(f)$.

The linear impairment, such as ISI and ICI, is estimated by the back-to-back transmission system sensitivity with and without the presence of linear impairments [46]. Since crosstalk generally varies in power and in shape, the back-to-back performance needs to be measured multiple times to count for the dynamic properties of the crosstalk. In this work, we demonstrate an efficient way for the P_{effXT} assessment with the knowledge of the transmitted signal PSD for various crosstalk power and shapes. We start out by introducing the in-band crosstalk spectral weighting metric, which is an essential step for P_{effXT} evaluation.

5.2 Weighted In-band Crosstalk Metric

Standard crosstalk power ratio (φ_{XT}) measures the crosstalk power (P_{XT}) that falls in the transmission channel bandwidth f_0 and compares it to the signal power (P_{ch}), Eq. 5.9. $X(f)$ and $S(f)$ are the crosstalk and transmission signal PSDs respectively. For a certain crosstalk shape, φ_{XT} describes the performance penalty at different crosstalk power. However, it is insufficient to quantify the system penalty brought by different crosstalk shapes, as the crosstalk impairment is spectra associated. It follows a general rule that at a fixed φ_{XT}, the crosstalk happens near the center of the transmission signal spectra is more detrimental than the one happens near the edges [39-42].

$$\varphi_{XT} = \frac{P_{XT}}{P_{ch}} = \frac{\int_{f_0} X(f)df}{\int_{f_0} S(f)df} \tag{5.9}$$

$$\varphi_{XTw} = \frac{P_{XTw}}{P_{ch}} = \frac{\int_{f_0} X(f) \cdot W(f)\, df}{\int_{f_0} S(f)df} \tag{5.10}$$

Where $W(f) = k \cdot S(f)$ and $k = \frac{\int_{f_0} S(f)df}{\int_{f_0} S^2(f)df}$

To account for the non-uniform spectral content of in-band crosstalk, a weighted crosstalk metric (φ_{XTw}) has been proposed, Eq. 5.10. It measures the weighted crosstalk power (P_{XTw}) by applying a weighting function $W(f)$ to the crosstalk PSD and normalized to the signal power. The scaling factor k is defined such that when the crosstalk signal has the same spectral attribution as the transmission signal, Eq. 5.10 is the same as Eq. 5.9 [39-41]. If $X(f)$ is out of the transmission band, φ_{XTw} equals to 0. If $X(f) = S(f)$, φ_{XTw} equals to 1.

The weighted crosstalk metric is demonstrated via RSOFT OptSim. Both the primary transmission signal and the crosstalk are NRZ-PM-QPSK modulated with a bit rate equals to 112 Gb/s. The crosstalk data source is independent of the transmission signal. The crosstalk is shaped and then dispersed to ensure it is noise-like. A 50 GHz grid (3.5^{th} order SuperGaussian optical filter) is applied at the transmitter to mimic the real transmission system. The crosstalk and transmission signal power are measured after the 50 GHz grid. At the receiver side, after photodetection, the received electrical signals are filtered individually by a 10^{th} order Bessel low pass electrical filter with 22 GHz bandwidth. The sampling rate is set at 80 Gsamples/s and the DSP is the same as Section 3.2.

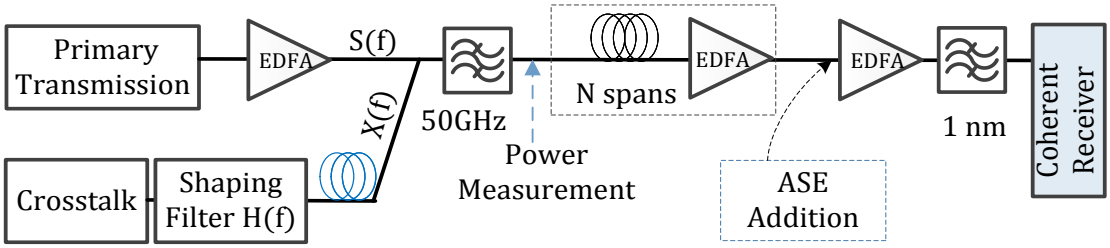

Figure 5.1. Rsoft simulation configuration for transmission system with in-band crosstalk addition.

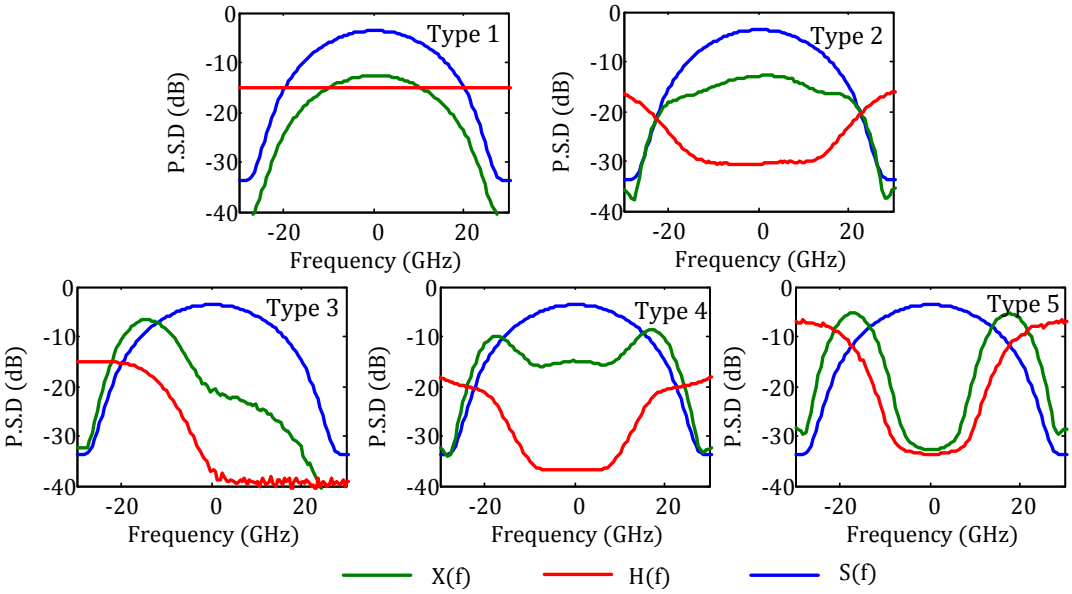

Figure 5.2. Crosstalk shaping filters, transmission signal PSDs and crosstalk PSDs.

We demonstrate the weighted crosstalk metric for a 28 Gbaud PM-QPSK system with PSD illustrated in Figure 5.2. Five crosstalk shapes are investigated with type 1 has the same PSD shape as the transmitted signal and type 5 has the most crosstalk power at the edges. The crosstalk is delayed by SSMF fiber. The input crosstalk power to the delaying fiber is small such that nonlinearity can be ignored. The Gaussian characteristic of the crosstalk signal is investigated by exploring the back-to-back received signal properties with no ASE noise presented. Even with a small dispersion (20 km SSMF), the

constellation of the transmission signal under the impairments of type 1 and type 5 crosstalk (φ_{XTw}=-13 dB) is Gaussian-*like*, Figure 5.3.a and b. The statistical distribution of the received signal is investigated by the histogram plot of the signal amplitude. Fig. 5.3.c and d. The Gaussian distribution with the same variance as the signal samples is shown to fit well with the signal samples. Based on this analysis, we can conclude that the crosstalk signal appears to be Gaussian and can be treated as an additional Gaussian noise contribution.

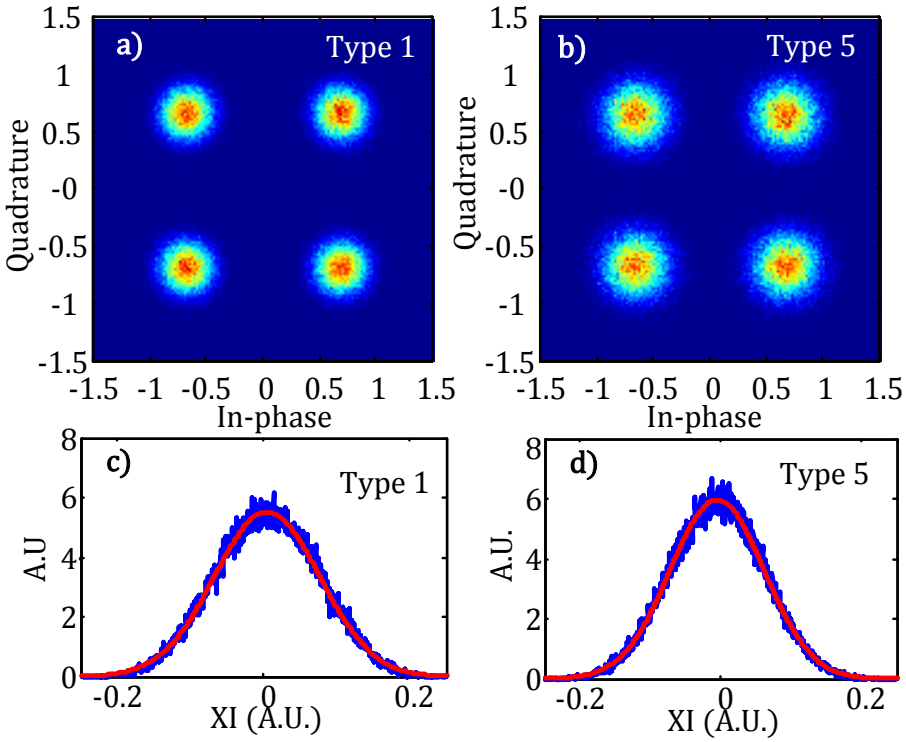

Figure 5.3. PM-QPSK received constellation in the absence of ASE noise under the impairments of in-band crosstalk φ_{XTw}=-13 dB: a) type 1 crosstalk, b) type 5 crosstalk; Histogram of the received signal points about their statistical average: c) type 1 crosstalk, d) type 5 crosstalk.

In real transmission systems, crosstalk is usually at least one span away from the transmission signal, so in the following simulation, all the crosstalk signals are delayed with 80 km SSMF. The OSNR penalty for five types of crosstalk is demonstrated for back-to-back transmission in Figure 5.4. Before weighting, the same OSNR penalty occurs over a large range of crosstalk powers, Figure 5.4.a). By applying the weighting metric in Eq. 5.10, an excellent correlation between the OSNR penalty and weighting crosstalk is observed, Figure 5.4.b). The same OSNR penalty is expected at a given φ_{XTw} for various crosstalk shapes. We investigate the OSNR penalty versus φ_{XTw} when the crosstalk signal is shaped ASE noise and compare the performance with the case when dispersed PM-QPSK is the crosstalk source. For all types of crosstalk, the OSNR penalty is close to the ASE noise reference, which supports our assessment that the crosstalk signal is statistically Gaussian distributed and is essentially colored ASE noise.

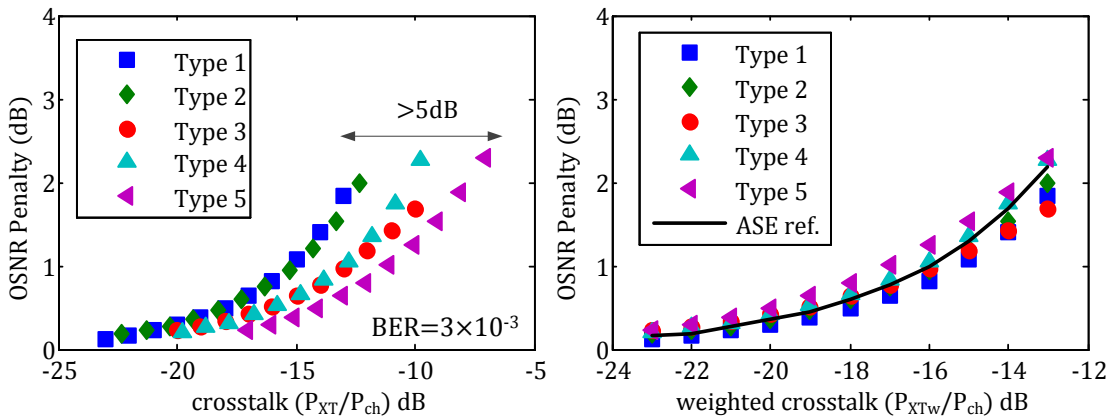

Figure 5.4. OSNR penalty versus a) crosstalk and b) weighted crosstalk at BER=3×10^{-3} for five types of crosstalk shapes of back-to-back transmission systems.

5.3 Equating Crosstalk Noise and ASE Noise

The weighted crosstalk metric treats all crosstalk equally with respect to the BER performance. However, P_{XTw} is not equal to P_{effXT} and is not equivalent to ASE noise since the weighting crosstalk metric uses the transmission signal PSD as a reference. Considering that the ASE noise is defined over 0.1 nm bandwidth and the signal PSD usually has bandwidth greater than 0.1 nm, only a portion of P_{XTw} counts towards the BER degradation. Thereafter, a crosstalk-to-ASE weighting factor η is introduced to treat P_{XTw} quantitatively as ASE noise:

$$P_{effXT} = \eta P_{XTw} \tag{5.11}$$

For a given signal PSD, it is anticipated that η is a constant for various crosstalk types at different P_{XTw}. Crosstalk is independent of the ASE noise, therefore, η shouldn't vary with ASE noise power. Based on the above discussion, for a given signal PSD, once η is known for one crosstalk type, it is applicable for other crosstalk types. Therefore, the theoretical η can be computed by considering a special case when the crosstalk signal is white ASE noise. P_{effXT} is essentially P_{ASE}, which is the integration of the crosstalk PSD (white ASE noise) over the center 0.1 nm bandwidth. Moreover, with the knowledge of the transmission signal PSD and crosstalk PSD (white ASE noise), P_{XTw} is calculated by the weighting metric in Eq. 5.10. Finally, η is calculated by

$$\eta = \frac{P_{effXT}}{P_{XTw}} = \frac{\int_{center\ 0.1nm\ BW} X(f)df}{\int_{f_0} X(f)W(f)df} \tag{5.12}$$

Since a 50 GHz grid is applied to both the crosstalk and the transmission signal, the integration bandwidth is limited to be 50 GHz. Take an example of the 28 Gbaud PM-

QPSK system with the transmitted signal PSD illustrated in Figure 5.2, the predicted η value is 0.41.

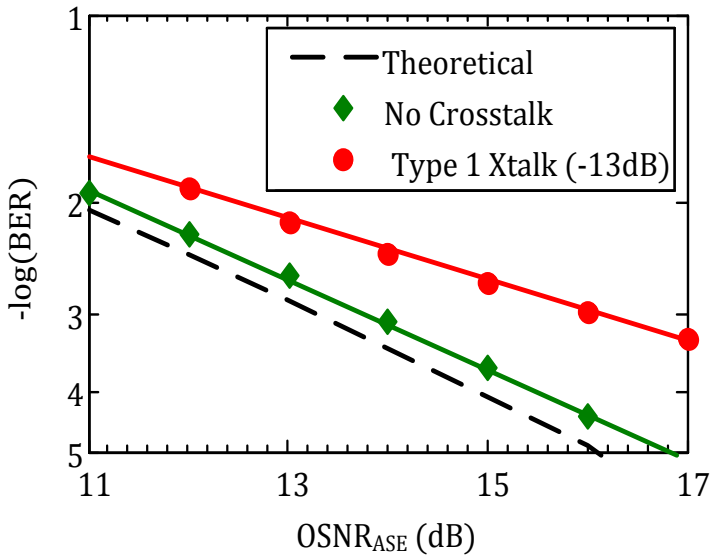

Figure 5.5. BER versus $OSNR_{ASE,dB}$ for back-to-back 112 bits/s PM-QPSK transmission with and without crosstalk impairments and the theoretical performance curve (dashed line).

Simulations are carried out in the back-to-back transmission system to validate the theoretical η value. Suppose the back-to-back transmission system sensitivity with and without crosstalk impairments is known in Figure 5.5 and the PSDs of the transmission signal and crosstalk are given Figure 5.2. According the BER and $OSNR_{ASE}$ relation in Eq. 5.1, a linear relation exists between $OSNR_{ASE,dB}$ and $log_{10}[(erfc^{-1}(BER)]$ [47], Figure 5.5. As real transmission systems exhibit imperfect modulator extinction ratios, quantization noise, equalization and etc., there is a mismatch between the theoretical (dashed line) and the simulated system performance (green line)

for back-to-back 112 bits/s PM-QPSK system. We consider the deviation as a change in slope and offset [47]. Therefore, $OSNR_{ASE,dB}$ is represented in terms of BER as:

$$OSNR_{ASE,dB} = p10log_{10}\boldsymbol{\Phi}^{-1}(BER) + q \tag{5.13}$$

and

$$\boldsymbol{\Phi}^{-1}(BER) = \left(2\frac{R_s}{B_{ref}}(erfc^{-1}(2BER))^2\right) \tag{5.14}$$

p and q are calculated by fitting (in the least square sense) the theoretical and simulated curves.

BER degrades when the crosstalk is introduced, Figure 5.5. The effective crosstalk noise needs to be taken into account for the generalization of $OSNR_{XT}$, Eq 5.15, such that the $OSNR_{XT}$ versus BER relation can still be described by Eq. 5.14.

$$OSNR_{XT} = \frac{P_{Tx,ch}}{P_{ASE} + P_{effXT}} \tag{5.15}$$

For any BER points on the BER versus $OSNR_{ASE,dB}$ curve with crosstalk impairment, $OSNR_{XT,dB}$ is computed through Eq. 5.15 and $OSNR_{ASE,dB}$ is known. P_{effXT} is then computed by:

$$P_{effXT} = \frac{P_{Tx,ch}}{OSNR_{XT}} - \frac{P_{Tx,ch}}{OSNR_{ASE}} \tag{5.16}$$

As the transmission signal and crosstalk PSDs are given, P_{XTw} is calculated using the weighting crosstalk metric in Eq. 5.10. Finally η is computed by Eq. 5.12.

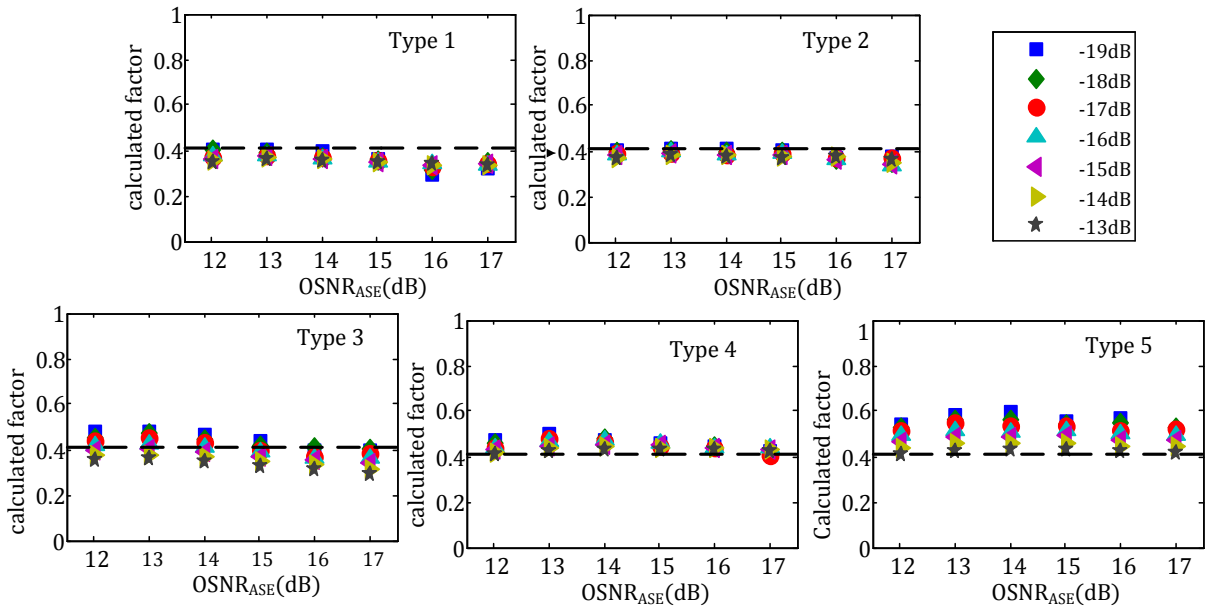

Figure 5.6. Calculated weighting factor η versus $OSNR_{ASE,dB}$ for back-to-back transmission with crosstalk impairments and the theoretical predicted η=0.41 (dashed line).

The calculated η versus $OSNR_{ASE,dB}$ at different weighted crosstalk φ_{XTw} are illustrated in Figure 5.6, with the corresponding crosstalk and transmission signal PSDs are presented in Figure 5.2. In all cases, the calculated η is around the predicted values 0.41. As expected, η is a constant at different crosstalk powers and is independent of ASE noise. Type 5 crosstalk gives a slightly higher η than the theoretical values, which is corresponding to the OSNR penalty results in Figure 5.4.b. We believe it is because for a given φ_{XTw}, the total φ_{XT} that enters the receiver is high for type 5 crosstalk such that the equalization effect on the crosstalk noise becomes noticeable. The variation of η brings less OSNR difference at low φ_{XTw} than high φ_{XTw}. Because at low φ_{XTw}, the dominant impact is the ASE noise, a variation of η is overshadowed by the ASE noise.

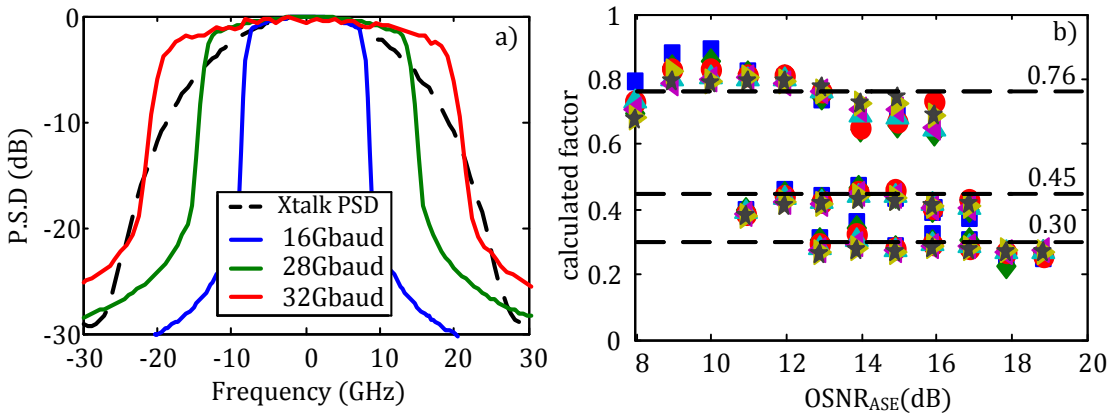

Figure 5.7. a) PM-QPSK transmission signal PSDs with Nyquist pulse shaping (rolloff is 0.1) at 16 Gbaud, 28 Gbaud and 32 Gbaud. The dashed line is the crosstalk PSD. b) Calculated η for systems with Nyquist signaling. Crosstalk powers vary from -19 dB to -13 dB. Dashed lines are the theoretical η.

The variation of η with the transmission signal properties is also investigated. Suppose the transmission signal PSDs are PM-QPSK Nyquist shaped (rolloff is 0.1) with baud rate equal to 16 Gbaud, 28 Gbaud, and 40 Gbaud, Figure 5.7.a and the crosstalk is the 112 Gbit/s NRZ-PM-QPSK signal. The calculated η is presented in Figure 5.7.b, comparing to the theoretical η: 0.76 ,0.45 and 0.3. In all cases, the calculated η follows well with the theoretical values. η increases with the decreasing of baud rate, as the same ASE noise power measured within 0.1 nm bandwidth is more detrimental when the signal spectra occupies less bandwidth.

5.4 Performance Predictions and Nonlinear Crosstalk Analysis

In the following section, the system's performance is predicted using the GN model. The crosstalk induced penalty is investigated both in the linear and nonlinear regime. The transmission signal and crosstalk properties are described in section 5.2.

5.4.1 Performance Predictions

Start with the back-to-back transmission system performance prediction with crosstalk impairments. Suppose the back-to-back sensitivity is known for a system without the presence of crosstalk. Obtain p and q in Eq. 5.13 by least square fitting the theoretical and simulated BER versus $OSNR_{ASE,dB}$ curves. Apply the weighted crosstalk metric in Eq. 5.10 for the computation of P_{XTw}. Then calculate P_{effXT} using Eq. 5.12 with η equals 0.41. Substitute P_{effXT} and the P_{ASE} in to Eq. 5.15 for $OSNR_{XT}$ computation. P_{ASE} in back-to-back transmission is the purposely loaded ASE noise at the end of transmission. Finally, $OSNR_{XT}$ is used in Eq. 5.13 for BER predictions. The predicted OSNR penalty versus weighted crosstalk φ_{XTw} is compared with the simulated results in Figure 5.8. Only one prediction curve is showing up for five types of crosstalk, because the same α is used for different crosstalk types. We notice that the predictions are mostly accurate at $\varphi_{XTw} \leq$-15 dB, with less than ±0.2 dB deviation shown between the predicted and simulated results. As expected, the predicted result overlaps with the ASE noise reference.

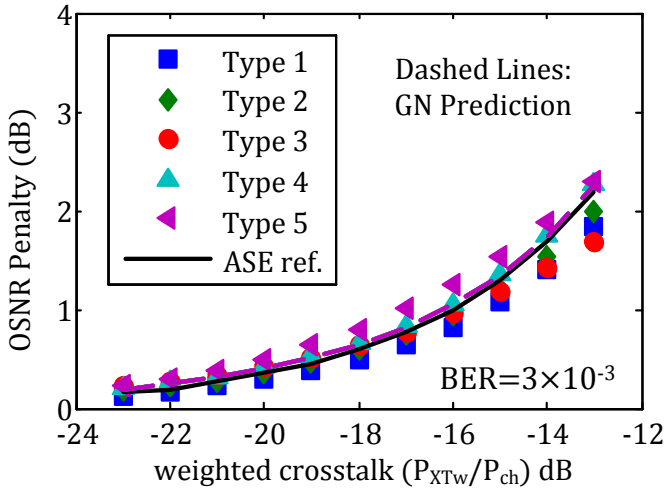

Figure 5.8. Predicted and measured OSNR penalty versus weighted crosstalk for five types of crosstalk shapes for back-to-back transmission.

The span test is carried out at 14×90 km SSMF transmission. The launch power is -4 dBm and 5 dBm in the linear and nonlinear regime respectively. The performance prediction in the linear regime follows the same procedure as the back-to-back transmission. P_{ASE} includes the ASE noise loaded at the end of transmission and originated from the EDFAs. Given the EDFA configurations such as the noise floor, amplifier gains and etc., the ASE noise from the EDFAs can be calculated by Eq. 5.3. Similar OSNR penalty shows up comparing with the back-to-back transmission. The predicted curve matches well with the simulated results.

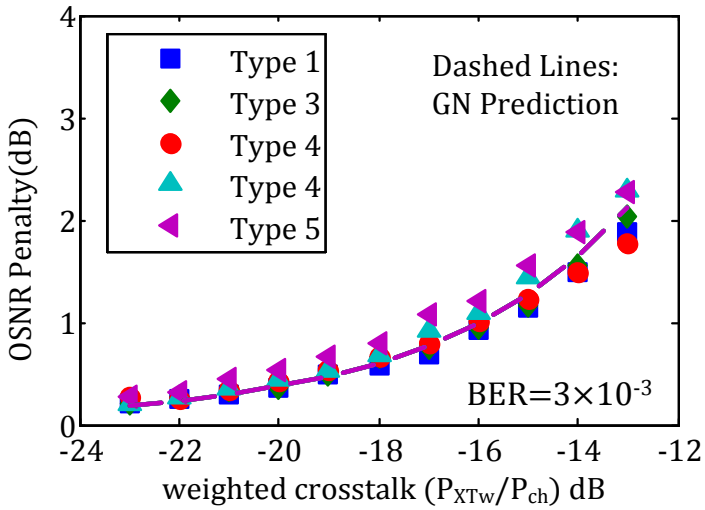

Figure 5.9. Predicted and measured OSNR penalty versus weighted crosstalk for five types of crosstalk shapes in linear regime 14×90 km SSMF transmission (P_{ch}=-4 dBm).

In the nonlinear regime, we first estimate the nonlinear PSD using the GN nonlinear analysis. We investigate here the case when nonlinear noise accumulated incoherently. With the presence of crosstalk, we consider the total transmission PSD as $X(f) + S(f)$, since crosstalk and transmission signals are considered as independent

signals. Moreover, after several kilometers of fiber transmission, the transmission signal together with the crosstalk has been fully dispersed to be noise like, the FWM analysis is still applicable to the system with crosstalk impairments.

Once P_{NLI} is computed, it is substituted into Eq. 5.5 for $OSNR_{tot}$ calculation and finally $OSNR_{tot}$ is applied into Eq. 5.13 for BER prediction. The nonlinear regime performance prediction example is shown in Figure 5.10. OSNR penalty follows a similar trend as in the linear regime. The prediction is accurate when $\varphi_{\mathrm{XTw}} \leq$-15 dB. In practical WDM system, the crosstalk ratio is designed to be lower than -16 dB, so the prediction is applicable to evaluate the system performances. The predicted OSNR penalty is slightly higher for type 5 crosstalk, as it has the highest transmission power. However, a larger OSNR penalty spread is observed compared with the linear regime performance even at small φ_{XTw}. We contribute this to the fact that the performance mismatch among different crosstalk types in the linear regime transmission has been enhanced due to the contribution of signal induced nonlinearity. Comparing with the global OSNR penalty in the nonlinear regime with the linear regime transmission, there is an enhanced OSNR penalty. It might be caused by the nonlinear parametric interaction between crosstalk and signals; or simply by the presence of the nonlinear noise which ensures that the ASE contribution is lower and further increases in additional noise sources result in large penalty [109]. In the following section, we will study the crosstalk induced nonlinear noise via the aid of GN model.

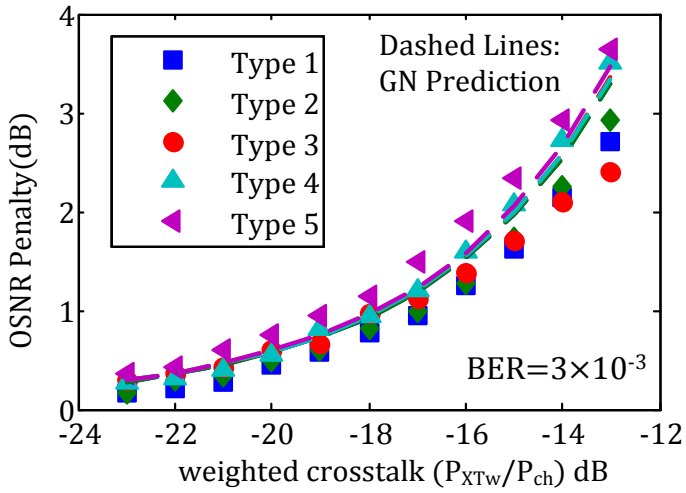

Figure 5.10. Predicted and measured OSNR penalty versus weighted crosstalk for five types of crosstalk shapes for nonlinear regime 14×90 km SSMF transmission (P_{ch}=5 dBm).

5.4.2 Crosstalk induced Nonlinear Noise Analysis

We investigate the crosstalk induced nonlinear noise after 14×90 km SSMF fiber transmission with P_{ch}=5 dBm. We denote the nonlinear PSD computed via the FWM model as $G_S(f)$ and $G_{SX}(f)$ of the transmission signal without and with crosstalk addition respectively. The net crosstalk induced nonlinear PSD is computed by $G_X(f) = G_{SX}(f) - G_S(f)$. Figure 5.11 exemplifies $G_X(f)$ for five crosstalk types. Even at φ_{XTw}=-13 dB, $G_X(f)$ carries less weight comparing with other penalties: the linear crosstalk and signal induced nonlinearity.

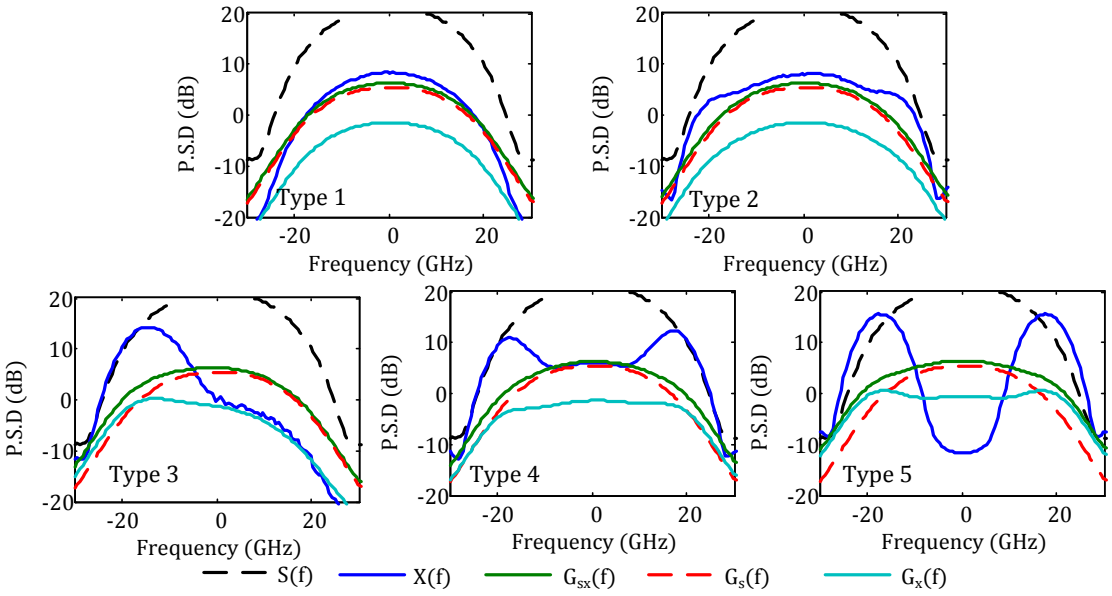

Figure 5.11. Transmission signal PSD: $S(f)$, Crosstalk PSDs $X(f)$, transmission nonlinear PSDs with and without crosstalk addition: $G_S(f)$ and $G_{SX}(f)$. crosstalk induced nonlinear PSDs $G_X(f)$ (weighted crossalk is -13 dB, 14×90 km SSMF fiber transmission, P_{ch}=5 dBm).

To make a further assessment of the crosstalk induced nonlinear noise, we compare the nonlinear noise power with the linear crosstalk noise power. Define the nonlinear crosstalk $\varphi_{NLI,XT}$ as the ratio of the integration of $G_X(f)$ to the transmission signal power P_{ch}, similar to the definition in Eq. 4. A comparison between $\varphi_{NLI,XT}$ and φ_{XTw} is shown in Figure 5.12.a. $\varphi_{NLI,XT}$ scales linearly with the φ_{XTw}, as the dominant nonlinearity is the mixing between crosstalk and transmission signal. It increases with the φ_{XTw} due to the enhanced crosstalk-signal beating in the nonlinear regime at high crosstalk powers. Type 5 crosstalk delivers the highest nonlinear noise because for the same φ_{XTw} it has the highest φ_{XT} comparing with other crosstalk types. Overall, the $\varphi_{NLI,XT}$ is much smaller than φ_{XTw}.

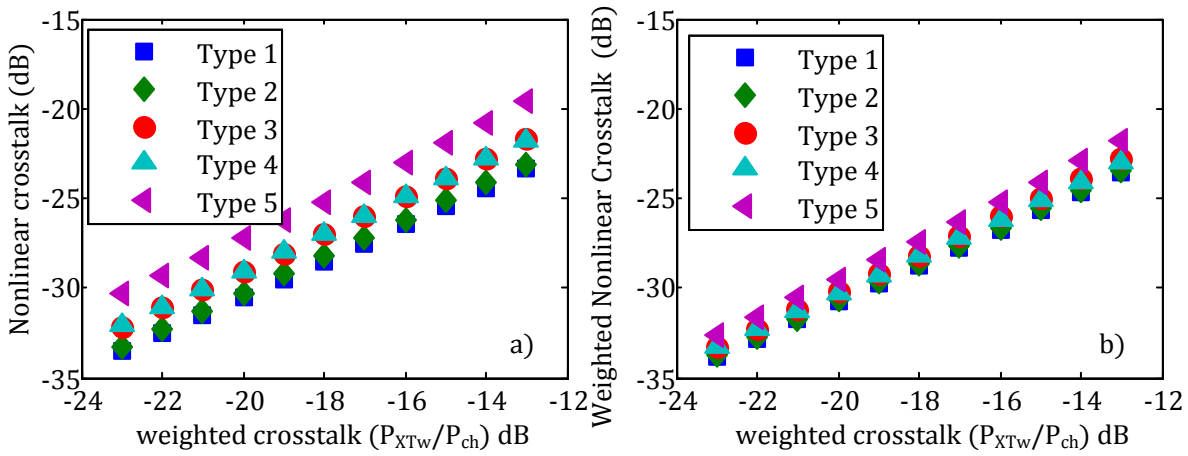

Figure 5.12. a) Nonlinear crosstalk versus linear weighted crosstalk, b) Nonlinear weighted crosstalk versus linear weighted crosstalk for five crosstalk types after span transmission (P_{ch}=5 dBm).

Figure 5.11 depicts the $G_X(f)$ at φ_{XTw}=-13 dB. Generally, $G_X(f)$ carries similar spectral shape as the crosstalk shapes $X(f)$. In order to better quantify the crosstalk induced nonlinearity, we weight the nonlinear PSD $G_X(f)$ towards the signal PSD, Eq. 5.10. We denote the weighted nonlinear crosstalk $\varphi_{NLI,XTw}$ as the ratio of the weighted nonlinear crosstalk power over the transmission signal power. All the crosstalk types bring small but similar $\varphi_{NLI,XTw}$, with type 5 has slightly higher nonlinear noise. The crosstalk induced nonlinear noise probably doesn't play significant role in system performance degradation at practically existing crosstalk powers for single channel transmission.

In summary, the weighted nonlinear crosstalk has small but similar values for in-band crosstalk with different spectral shapes. Major performance degradation is due to the signal induced nonlinearity and linear crosstalk addition.

5.5 Experimental Validations

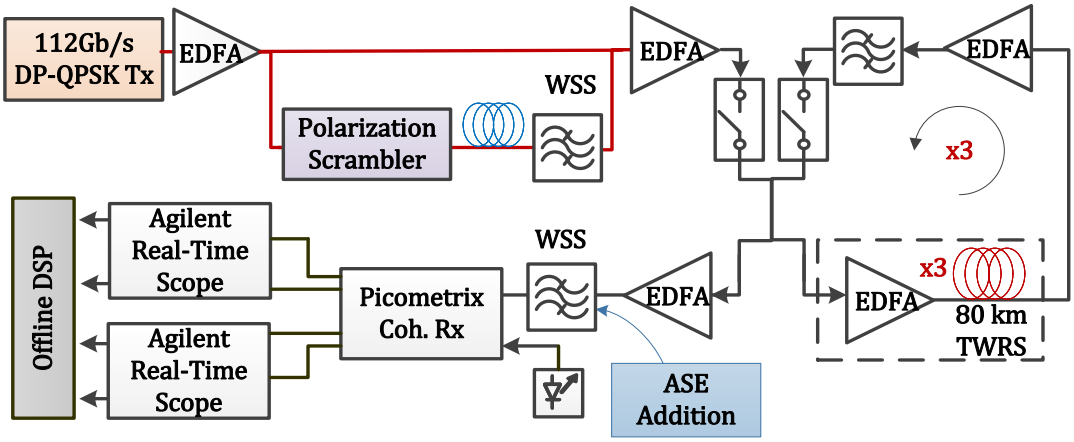

Figure 5.13. Experimental setup for PM-QPSK with crosstalk addition.

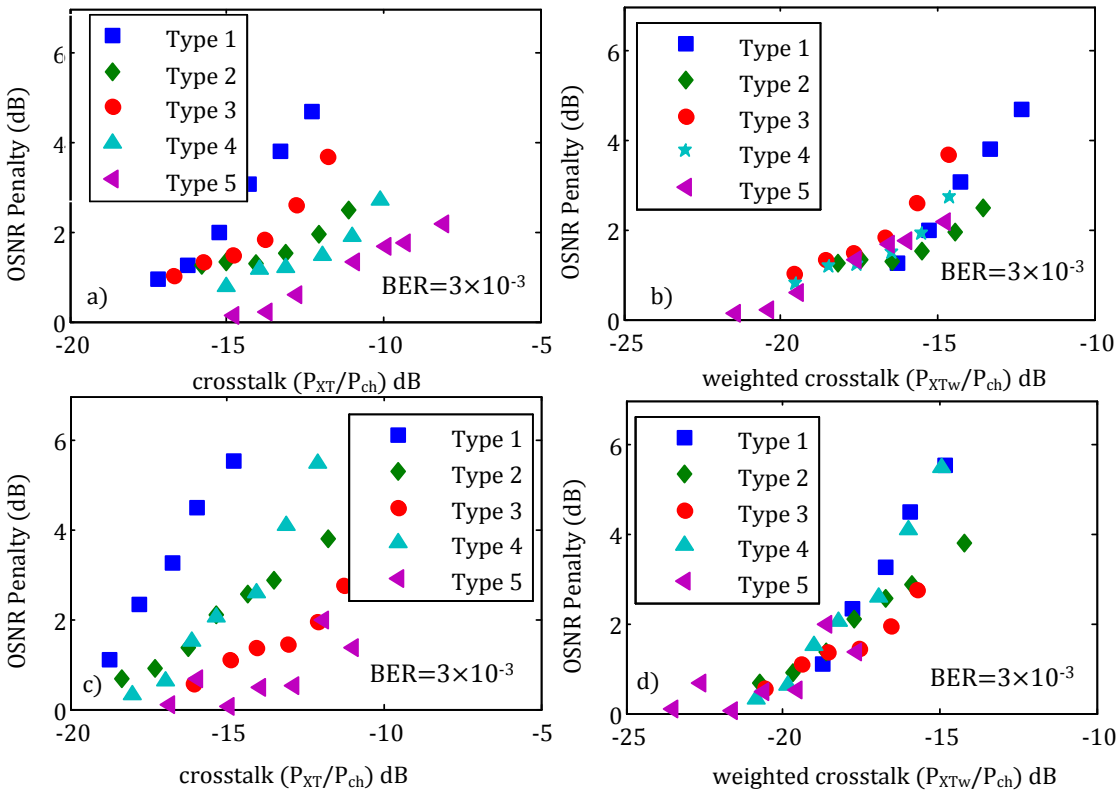

Figure 5.14. OSNR penalty versus a) crosstalk, b) weighted crosstalk (P_{ch}=-1 dBm), c) crosstalk, d) weighted crosstalk (P_{ch}=3 dBm) [110].

We experimentally investigate the crosstalk impairments after 8×83 km TWRS fiber transmission at different launch powers for 112 Gbits/s NRZ-PM-PQSK system, Figure 5.13, with the crosstalk spectra similar to Figure 5.2.

The weighting metric has been applied to the linear and nonlinear regime transmission. Consistent with the simulation results, OSNR penalty converges for five crosstalk types after applying the weighting metric, Figure 5.14. The overall OSNR penalty is higher both in the linear and nonlinear regime due to extra penalty from the loop switch implementation. In the nonlinear regime, and increased OSNR penalty is observed.

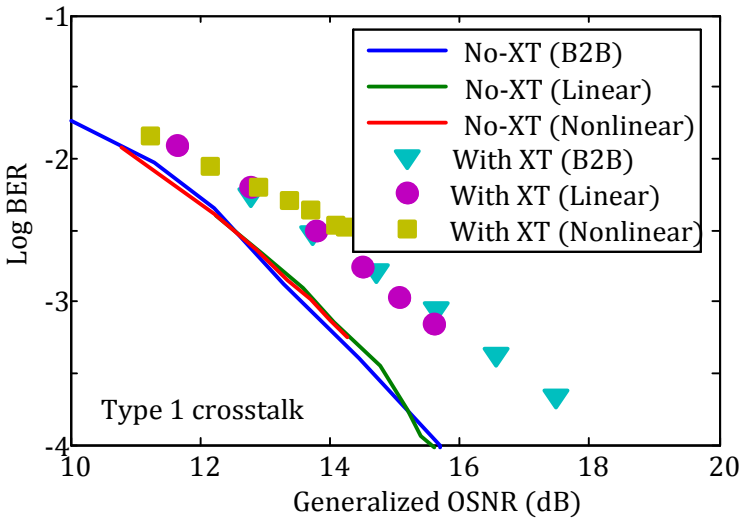

Figure 5.15. BER versus OSNR for system with and without crosstalk impairments in back-to-back, linear, and nonlinear regimes (type 1 crosstalk, weighted crosstalk is -15 dB).

To demonstrate the net penalty due to crosstalk addition both in the back-to-back, linear, and nonlinear regime, we use the generalized OSNR, the loop penalties need to be

computed. Assume the loop penalty is modeled as additive Gaussian noise and it a pure linear impairment, the loop penalty power P_{loop} can be used to generalized the OSNR. The generalized OSNRs in the back-to-back, linear and nonlinear regime are defined as following:

$$OSNR_{btb} = \frac{P_{ch}}{P_{ASE}} \tag{5.17}$$

$$OSNR_{linear} = \frac{P_{ch}}{P_{ASE} + P_{loop}} \tag{5.18}$$

$$OSNR_{linear} = \frac{P_{ch}}{P_{ASE}+P_{loop}+P_{sig,NLI}} \tag{5.19}$$

Where $P_{sig,NLI}$ is the transmission signal induced nonlinear noise. Now that we have the system performance curves in the back-to-back, linear and nonlinear regimes, along with the generalized OSNR definition, P_{loop} and $P_{sig,NLI}$ can be computed. The plot of the BER versus the generalized OSNR should overlaps in all cases, Figure 5.15.

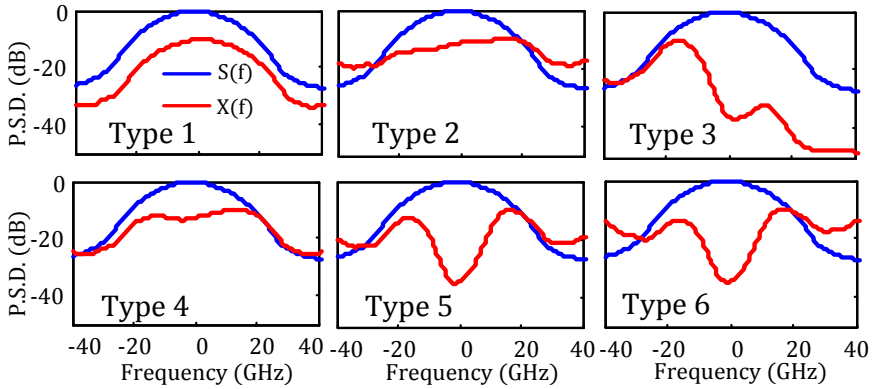

Figure 5.16. PSDs of primary transmission signal and crosstalk.

We experimentally measured the BER versus OSNR for all six crosstalk PDSs of Figure 5.16 for crosstalk power ranging from -22 to -9 dB corresponding to a weighted

crosstalk power between -24 to -12 dB. We then compute the colored noise weighting factor η, Figure 5.17. In all cases, the experimentally determined η is nearly constant for different crosstalk powers, is independent of ASE noise (OSNR), and is close to the theoretical value of 0.38. Type 3 exhibits a slightly higher value. This is likely the result of the variation in the dynamic equalization of the receiver decoder and is also apparent in the slightly higher OSNR penalty in Figure 5.18.b. We note that at low OSNR (high P_{ASE}) the ASE noise dominates and there is more uncertainty in the determination η.

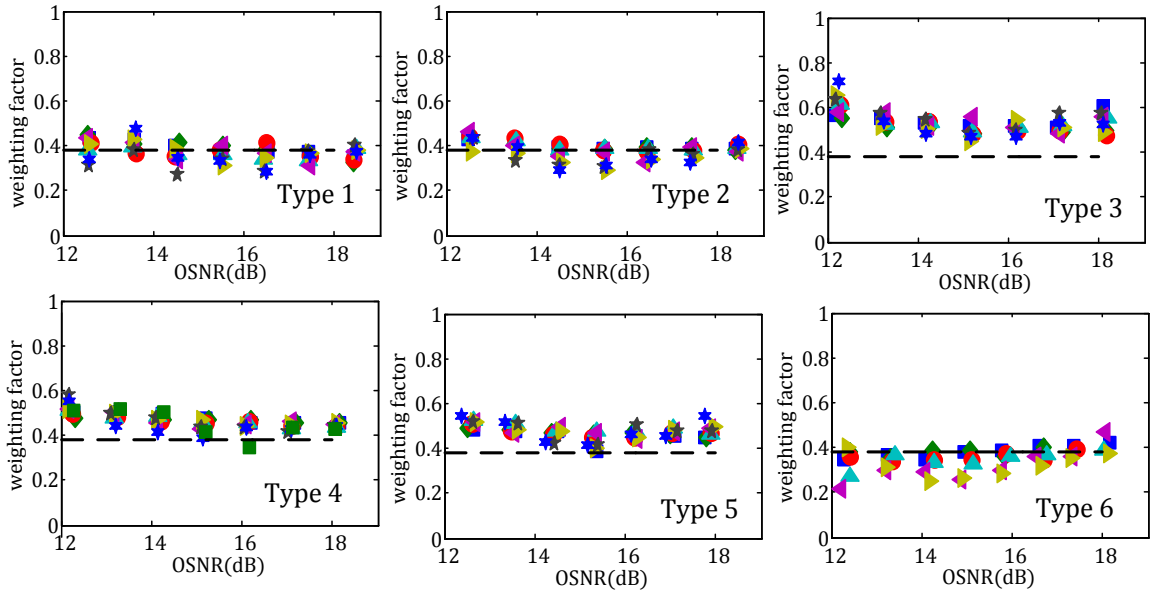

Figure 5.17. Measured colored-to-white noise weighting factor for weighted crosstalk between -21 dB to -12 dB (different data marks) for each of the crosstalk PSDs of Figure 5.16. The dashed line represents the theoretical expectation.

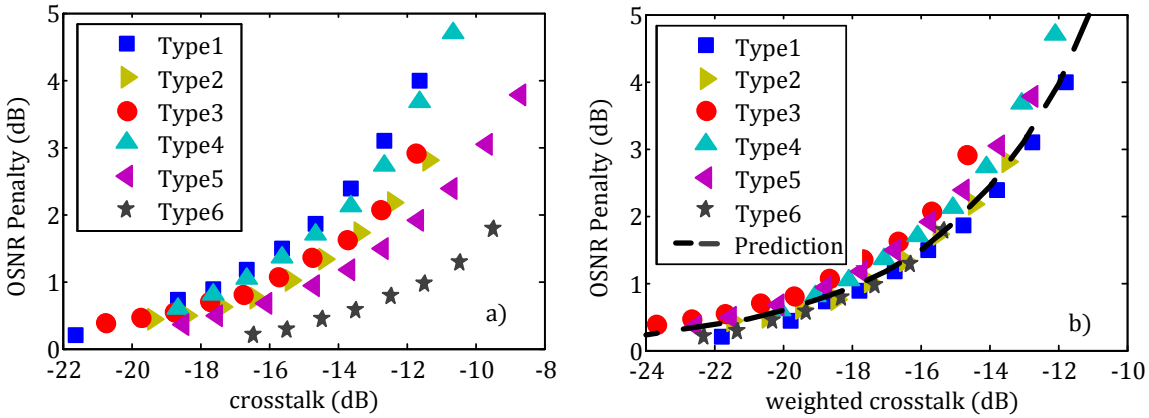

Figure 5.18. OSNR penalty versus a) crosstalk, b) weighted crosstalk for six types of crosstalk shapes in back-to-back 31.5Gbaud PM-QPSK transmission systems (BER=10^{-3}). Dashed line: GN model predicted performance.

We also demonstrate the use of η as a design metric to predict the OSNR penalty via the GN model. Since the crosstalk penalty is a linear impairment, the demonstrated back-to-back capability suggests it is also applicable in the linear and nonlinear transport regimes for overall system performance prediction. Specifically, for a given crosstalk PSD, we evaluate P_{XTw} and P_{effXT} via Eqs. 5.10 and 5.11. Then $OSNR_{XT}$ is determined via Eq. 5.15 using P_{effXT}. Finally the BER is predicted by the measured $\Phi(OSNR_{XT})$. The results are shown as the dashed line in Figure 5.18. There is an excellent match between the measured results and the predicted results validating our methods.

As in real transmission systems, the PDL between X/Y-pol of the crosstalk signal may significantly vary. We study the crosstalk PDL impact on the system performance by purposely introducing power imbalance for type 1 crosstalk with φ_{XTw} fixed at -17.7 dB. The BER vs. OSNR results demonstrate the system performance is insensitive to the crosstalk PDL, indicating the proposed work is valid at large crosstalk PDL.

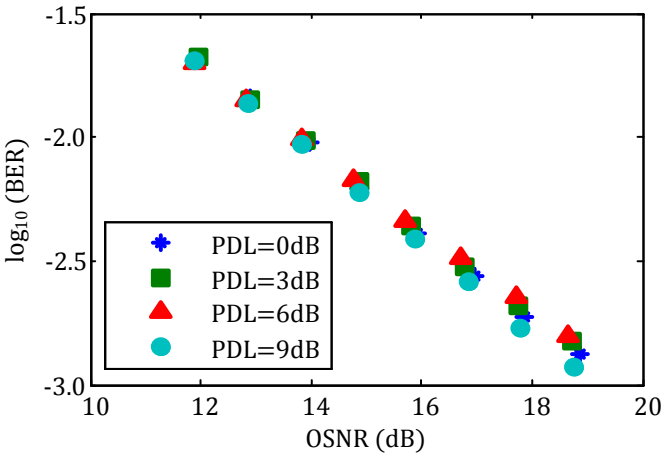

Figure 5.19. BER versus OSNR at different crosstalk PDL value for type 1 crosstalk of weighted crosstalk power -17.7dB.

5.6 Chapter Summary

In this work, the GN model has been extended to assess the in-band crosstalk induced performance penalty both in the linear and nonlinear regimes. We concluded that the in-band crosstalk is statistically Gaussian distributed, even after the crosstalk being dispersed for a short fiber distance. It can be added with the ASE and nonlinear noise to generalize OSNR for performance prediction. A crosstalk-to-ASE weighting factor has been introduced to treat the weighted crosstalk power quantitatively equivalent to ASE noise. The weighting factor has been shown to be transmission signal PSD dependent and don't vary with crosstalk shapes and powers. It is combined with the crosstalk weighting metric for assessing the system performance under the impairments of in-band crosstalk. The crosstalk induced nonlinearity has been investigated via the aid of a GN nonlinear model. It has been shown that the crosstalk induced nonlinearity is weak both analytically and experimentally.

CHAPTER 6

CONCLUSIONS

We proposed two novel blind channel estimation techniques based on the DD-LMS and the frequency domain method. Both experiments and simulations showed that the two algorithms were able to mitigate narrow band filtering and were very tolerable to the channel estimation noise. Tap length as low as ten can be used for channel compensation. It was also found that the frequency domain approach delivered slightly better performance than the DD-LMS approach and was more robust to the channel estimation noise because no receiver demodulation was performed. The frequency domain pre-shaper only needed to be estimated once and may compensate ISI effects for different baud rates, enabling a 50 Gbaud PM-QPSK (1.28 sample/symbol) transmission. The CD pre-compensation via the DAC was studied. The Nyquist filter implementation can be combined with the CD filter without adding additional computational complexity. The transmitter CD compensation was beneficial when the LO laser linewidth was large.

A novel super-receiver structure was proposed, where information from different subchannels was captured with synchronized sampling scopes, enabling a joint ICI mitigation. The pre-required techniques that enabled a successful ICI compensation were discussed; including the joint CD compensation, frequency shifting, and inter-channel de-skew. Three different ICI compensation algorithms were introduced with their performance compared. All the ICI compensation methods demonstrated improved performance compared to the conventional ISI equalization. A joint carrier phase

recovery was proposed and it was concluded that the joint carrier recovery was less vulnerable to the phase slip.

Lastly, we proposed the in-band crosstalk analysis and performance prediction using the GN model. Through a crosstalk weighting metric and a crosstalk to ASE noise weighting factor, we successfully incorporated the effective crosstalk noise in the GN model. The nonlinear parametric interaction between the crosstalk and transmission signal were discussed in the dispersion uncompensated link. It was concluded that the crosstalk induced nonlinearity was much smaller than its corresponding linear crosstalk power.

6.1 Future Research Topics

With the accessibility of high speed DACs, there are several aspects to expand current research topics.

6.1.1 Transmitter Signal Processing

The ongoing research investigates the linear pre-shaping for single channel applications, mostly in the back-to-back transportation regime. Therefore, the pre-shaping performances after fiber transmission, both in the linear and nonlinear regimes, need to be investigated. Because the high frequency components of the signal spectra are enhanced with pre-shaping which may introduce ICI penalty, it is desirable to study the pre-shaping effects in WDM systems. Meanwhile, the transmitter signal processing is not only limited to the channel bandwidth compensation, but also can be extended to driver, modulator, and transmission channel nonlinearity compensation.

6.1.2 Gaussian Noise Model Generalization

The GN model has been applied to assess the in-band crosstalk penalty in the linear and nonlinear regimes, mostly for PM-QPSK system. It is desired to validate the weighted in-band crosstalk metric thoroughly for higher order modulation formats, such as PM-16QAM and PM-64QAM.

REFERENCES

1. Index, C.V.N., Forecast and Methodology, 2009–2014, 2010.

2. R. Ramaswami, et al., Optical networks: a practical perspective. 2009: Morgan Kaufmann.

3. K. Roberts, et al., "100G and beyond with digital coherent signal processing". *IEEE Communications Magazine*, 2010. 48(7): p. 62-69.

4. S. J. Savory, et al., "Electronic compensation of chromatic dispersion using a digital coherent receiver". *Optics Express*, 2007. 15(5): p. 2120-2126.

5. N. Kaneda, et al., "Coherent polarization-division-multiplexed QPSK receiver with fractionally spaced CMA for PMD compensation". *IEEE Photonics Technology Letters*, 2009. 21(4): p. 203-205.

6. F. P. Guiomar, et al., "Experimental demonstration of a frequency-domain Volterra series nonlinear equalizer in polarization-multiplexed transmission". *Optics Express*, 2013. 21(1): p. 276-288.

7. N. K. Fontaine, et al., "Fiber nonlinearity compensation by digital backpropagation of an entire 1.2-Tb/s superchannel using a full-field spectrally-sliced receiver". in European Conference and Exhibition on Optical Communication, 2013, paper Mo.3.D.5.

8. E. Ip, et al., "Compensation of dispersion and nonlinear impairments using digital backpropagation". *Journal of Lightwave Technology*, 2008. 26(20): p. 3416-3425.

9. L. E. Nelson, et al., "A robust real-time 100G transceiver With soft-decision forward error correction". *IEEE/OSA Journal of Optical Communications and Networking*, 2012. 4(11): p. B131-B141.

10. W. Shieh, et al., "A two-mode fiber design and characterization". 2012.

11. S. Randel, et al. "Mode-multiplexed 6× 20-GBd QPSK transmission over 1200-km DGD-compensated few-mode fiber". in National Fiber Optic Engineers Conference, 2012, paper PDP5C.5.

12. D. Richardson, et al., "Space-division multiplexing in optical fibres". *Nature Photonics*, 2013. 7(5): p. 354-362.

13. H. Takara, et al., "1.01-Pb/s (12 SDM/222 WDM/456 Gb/s) crosstalk-managed transmission with 91.4-b/s/Hz aggregate spectral efficiency". in European Conference and Exhibition on Optical Communication, 2012, paper Th.3.C.1.

14. R. Tucker, et al., “Optical time-division multiplexing for very high bit-rate transmission”. *Journal of Lightwave Technology*, 1988. 6(11): p. 1737-1749.

15. G. Raybon, et al., “High symbol rate coherent optical transmission systems: 80 and 107 Gbaud”. *Journal of Lightwave Technology*, 2014. 32(4): p. 824-831.

16. M. Nakazawa, et al., “Ultrahigh-speed “orthogonal” TDM transmission with an optical Nyquist pulse train”. *Optics Express*, 2012. 20(2): p. 1129-1140.

17. T. Hirooka, et al., “Highly dispersion-tolerant 160 Gbaud optical Nyquist pulse TDM transmission over 525 km”. *Optics Express*, 2012. 20(14): p. 15001-15007.

18. S. Randel, et al., “Generation of a digitally shaped 55-GBd 64-QAM single-carrier signal using novel high-speed DACs”. in Optical Fiber Communication Conference, 2014, paper M2A.3.

19. J. Rahn, et al., “Super-channels: DWDM transmission beyond 100 Gb/s”. in IEEE Photonics Conference, 2012.

20. G. Bosco, et al., “Performance limits of Nyquist-WDM and CO-OFDM in high-speed PM-QPSK systems”. *IEEE Photonics Technology Letters*, 2010. 22(15): p. 1129-1131.

21. S. Chandrasekhar, et al., “Experimental investigation on the performance of closely spaced multi-carrier PDM-QPSK with digital coherent detection”. *Optics Express*, 2009. 17(24): p. 21350-21361.

22. S. Chandrasekhar, et al., “Transmission of a 1.2-Tb/s 24-carrier no-guard-interval coherent OFDM superchannel over 7200-km of ultra-large-area fiber”. in European Conference and Exhibition on Optical Communication, 2009.

23. X. Liu, et al., “Transmission of a 448-Gb/s reduced-guard-interval CO-OFDM signal with a 60-GHz optical bandwidth over 2000 km of ULAF and five 80-GHz-grid ROADMs”. in Optical Fiber Communication Conference, 2010, paper PDPC2.

24. Y. Ma, et al., “1-Tb/s single-channel coherent optical OFDM transmission with orthogonal-band multiplexing and subwavelength bandwidth access”. *Journal of Lightwave Technology*, 2010. 28(4): p. 308-315.

25. G. Bosco, et al. “Investigation on the robustness of a Nyquist-WDM terabit superchannel to transmitter and receiver non-idealities”. in European Conference and Exhibition on Optical Communication, 2010, paper Tu.3.A.4.

26. G. Bosco, et al., “On the performance of Nyquist-WDM terabit superchannels based on PM-BPSK, PM-QPSK, PM-8QAM or PM-16QAM subcarriers”. *Journal of Lightwave Technology*, 2011. 29(1): p. 53-61.

27. G. Gavioli, et al., “Investigation of the impact of ultra-narrow carrier spacing on the transmission of a 10-carrier 1Tb/s superchannel”. in Optical Fiber Communication Conference, 2010, paper OThD3.

28. J. Zhao, et al., “Electronic impairment mitigation in optically multiplexed multicarrier systems”. *Journal of Lightwave Technology*, 2011. 29(3): p. 278-290.

29. J. X. Cai, et al., “20 Tbit/s transmission over 6860 km with sub-Nyquist channel spacing”. *Journal of Lightwave Technology*, 2012. 30(4): p. 651-657.

30. R. Cigliutti, et al., “Transmission of 9 x 138 Gb/s prefiltered PM-8QAM signals over 4000 km of pure silica-core fiber”. *Journal of Lightwave Technology*, 2011. 29(15): p. 2310-2318.

31. R. Schmogrow, et al., “Pulse-shaping with digital, electrical, and optical filters-a comparison”. *Journal of Lightwave Technology*, 2013. 31(15): p. 2570-2577.

32. J. Wang, et al., “Generation of spectrally efficient Nyquist-WDM QPSK signals using digital FIR or FDE filters at transmitters”. *Journal of Lightwave Technology*, 2012. 30(23): p. 3679-3686.

33. R. Schmogrow, et al., “Real-time Nyquist signaling with dynamic precision and flexible non-integer oversampling”. *Optics Express*, 2014. 22(1): p. 193-209.

34. R. Schmogrow, et al., “Real-time Nyquist pulse generation beyond 100 Gbit/s and its relation to OFDM”. *Optics Express*, 2012. 20(1): p. 317-337.

35. M. Rubsamen, et al., “MLSE receivers for narrow-band optical filtering”. in Optical Fiber Communication Conference, 2006, paper OWB6.

36. C. Yi, et al., “Ultra-long-haul WDM transmission with high spectral efficiency”. *IEICE transactions on communications*, 2011. 94(2): p. 392-399.

37. Y. Jiang, et al., “Electronic pre-compensation of narrow optical filtering for OOK, DPSK and DQPSK modulation formats”. *Journal of Lightwave Technology*, 2009. 27(16): p. 3689-3698.

38. Z. Dong, et al., “6×144-Gb/s Nyquist-WDM PDM-64QAM generation and transmission on a 12-GHz WDM grid equipped with Nyquist-band pre-equalization”. *Journal of Lightwave Technology*, 2012. 30(23): p. 3687-3692.

39. M. Filer, et al., “Generalized weighted crosstalk for DWDM systems with cascaded wavelength-selective switches”. *Optics Express*, 2012. 20(16): p. 17620-17631.

40. Y.T. Hsueh, et al. “Crosstalk-induced OSNR penalty prediction on 112 Gb/s PolMux-QPSK system”. in Conference on Lasers and Electro-Optics, 2011, paper CThH6.

41. Y. T. Hsueh, et al., “Passband narrowing and crosstalk impairments in ROADM-enabled 100G DWDM networks”. *Journal of Lightwave Technology*, 2012. 30(24): p. 3980-3986.

42. T. Zami, et al.,. Impact of crosstalk on real-time coherent detection of 112 Gb/s PDM-QPSK signal in WDM transparent networks”. in National Fiber Optic Engineers Conference, 2013, paper NM2E.4.

43. P. Johannisson, “Analytical modeling of nonlinear propagation in a strongly dispersive optical communication system”. 2012.

44. P. Poggiolini, “The GN model of non-linear propagation in uncompensated coherent optical systems”. *Journal of Lightwave Technology*, 2012. 30(24): p. 3857-3879.

45. G. Bosco, et al., “Experimental investigation of nonlinear interference accumulation in uncompensated links”. *IEEE Photonics Technology Letters*, 2012. 24(13): p. 1230.

46. A. Carena, et al., “Modeling of the impact of nonlinear propagation effects in uncompensated optical coherent transmission links”. *Journal of Lightwave Technology*, 2012. 30(10): p. 1524-1539.

47. A. J. Stark, et al., “System performance prediction with the Gaussian noise model in 100G PDM-QPSK coherent optical networks”. *Journal of Lightwave Technology*, 2013. 31(21): p. 3352-3360.

48. V. Bobrovs, et al., “Influence of nonlinear optical effects on the NRZ and RZ modulation signals in WDM systems”. *Electronics and Electrical Engineering*, 2007. 4(76): p. 55-58.

49. I. P. Kaminow, et al., Optical Fiber Telecommunication IV B Systems and Impairments. Academic, San Diego, 2002.

50. H. S. Chung, et al., “Impact of non-ideal pulse carving induced phase distortions on QPSK based modulation format”. in European Conference and Exhibition on Optical Communication, 2009, paper P3.07.

51. E. Ip, et al., “Power spectra of return-to-zero optical signals”. *Journal of Lightwave Technology*, 2006. 24(3): p. 1610-1618.

52. P. J. Winzer, et al., “Advanced optical modulation formats”. *Proceedings of the IEEE*, 2006. 94(5): p. 952-985.

53. C. Caspar, et al., “RZ versus NRZ modulation format for dispersion compensated SMF-based 10-Gb/s transmission with more than 100-km amplifier spacing”. *IEEE Photonics Technology Letters*, 1999. 11(4): p. 481-483.

54. M. Hayee, et al., “NRZ versus RZ in 10-40-Gb/s dispersion-managed WDM transmission systems”. *IEEE Photonics Technology Letters*, 1999. 11(8): p. 991-993.

55. C. Xie, et al., “Comparison of RZ and NRZ formats in 112-Gb/s PDM-QPSK long haul coherent transmission systems”. in National Fiber Optic Engineers Conference, 2011, paper JThA039.

56. S. Yan, et al., “Generation of square or hexagonal 16-QAM signals using a dual-drive IQ modulator driven by binary signals”. *Optics Express*, 2012. 20(27): p. 29023-29034.

57. X. Zhou, et al., “Spectrally-efficient high-speed optical transmission technologies”. in OptoElectronics and Communications Conference, 2009.

58. W. R. Peng, et al., “DAC-free generation and 320-km transmission of 11.2-GBd PDM-64QAM using a single I/Q modulator”. in European Conference and Exhibition on Optical Communication, 2012, paper We.1.C.3.

59. Y. Gao, et al., “Reducing the complexity of nonlinearity pre-compensation using symmetric EDC and pulse shaping”. *Optics Express*, 2013. 22(2): p. 1209-1219.

60. L. Bangjiang, et al., “Pre-compensation of Mach-Zehnder modulator nonlinearity for DD-OFDM system”. in OptoElectronics and Communications Conference held jointly with International Conference on Photonics in Switching, 2013, paper MP1.3.

61. Q. Zhuge, et al., “Aggressive quantization on perturbation coefficients for nonlinear pre-distortion”. in Optical Fiber Communication Conference. 2014, paper Th4D.7.

62. S. Hughes, et al., “Linearity Requirements of QAM Transmitters”. in Optical Fiber Communication Conference, 2015, paper Th2A.12.

63. A. J. Stark, “16QAM for next-generation optical transport networks”. Thesis, 2013.

64. A. J. Stark, et al., “Advanced signaling technologies for high-speed digital fiber-optic links”. *Applied Optics*, 2014. 53(25): p. 5824-5840.

65. M. Nakazawa, et al., High spectral density optical communication technologies. Vol. 10. 2010: Springer.

66. H. S. Chung, et al., “Field trial of automatic bias control scheme for optical IQ modulator and demodulator with directly detected 112 Gb/s DQPSK Signal”. *Optics Express*, 2013. 21(21): p. 24962-24968.

67. A. Sano, et al., “69.1-Tb/s (432×171-Gb/s) C- and extended L-band transmission over 240 km using PDM-16-QAM modulation and digital coherent detection”. in Optical Fiber Communication Conference, 2010, paper PDPB7.

68. X. Zhou, et al., “32Tb/s (320×114Gb/s) PDM-RZ-8QAM Transmission over 580km of SMF-28 Ultra-Low-Loss Fiber”. in Optical Fiber Communication Conference and National Fiber Optic Engineers Conference, 2009, paper PDPB4.

69. J. A. Buck, Fundamentals of optical fibers. 2004: John Wiley & Sons.

70. K. O. Hill, et al., “Fiber Bragg grating technology fundamentals and overview”. *Journal of Lightwave Technology*, 1997. 15(8): p. 1263-1276.

71. Y. Painchaud, et al. “Fiber Bragg grating based dispersion compensator slope-matched for LEAF fiber”. in Optical Fiber Communication Conference, 2006, paper OThE2.

72. L. Li, “Interaction between PDL and intra-channel nonlinearity in dual polarization systems”. in 16th Opto-Electronics and Communications Conference. 2011.

73. O. Vassilieva, et al.,. “Statistical analysis of the interplay between nonlinear and PDL effects in coherent polarization multiplexed systems”. in European Conference and Exhibition on Optical Communication, 2012.

74. C. R. Menyuk, et al., “Interaction of polarization mode dispersion and nonlinearity in optical fiber transmission systems”. *Journal of Lightwave Technology*, 2006. 24(7): p. 2806.

75. D. Rafique, et al., “Compensation of intra-channel nonlinear fibre impairments using simplified digital back-propagation algorithm”. *Optics Express*, 2011. 19(10): p. 9453-9460.

76. X. Liang, et al., “Digital compensation of cross-phase modulation distortions using perturbation technique for dispersion-managed fiber-optic systems”. *Optics Express*, 2014. 22(17): p. 20634-20645.

77. R. Kudo, et al., “Coherent optical single carrier transmission using overlap frequency domain equalization for long-haul optical systems”. *Journal of Lightwave Technology*, 2009. 27(16): p. 3721-3728.

78. V. Ribeiro, et al. “Accurate blind chromatic dispersion estimation in long-haul 112Gbit/s PM-QPSK WDM coherent systems”. in Signal Processing in Photonic Communications, 2012, paper SpTh2B.3.

79. Q. Sui, et al., “Fast and robust blind chromatic dispersion estimation using auto-correlation of signal power waveform for digital coherent systems”. *Journal of Lightwave Technology*, 2013. 31(2): p. 306-312.

80. S. S. Haykin, Adaptive filter theory. 2008: Pearson Education India.

81. M. Oerder, et al., “Digital filter and square timing recovery”. Communications, IEEE Transactions on, 1988. 36(5): p. 605-612.

82. G. Eynard, et al., “Non data aided timing recovery algorithm for digital underwater communications”. in OCEANS, 2007.

83. K. Kikuchi, “Polarization-demultiplexing algorithm in the digital coherent receiver”. in IEEE/LEOS Summer Topical Meetings, 2008.

84. K. Kikuchi, “Performance analyses of polarization demultiplexing based on constant-modulus algorithm in digital coherent optical receivers”. *Optics Express*, 2011. 19(10): p. 9868-9880.

85. D. Godard, “Self-recovering equalization and carrier tracking in two-dimensional data communication systems”. *IEEE Transactions on Communications*, 1980. 28(11): p. 1867-1875.

86. S. Guo, et al., “Weighted multi-modulus blind equalization algorithm based on momentum term”, in Mechanical Engineering and Technology. 2012, Springer. p. 625-630.

87. Mendes Filho, et al., “A family of algorithms for blind equalization of QAM signals”. in IEEE International Conference on Acoustics, Speech and Signal Processing, 2011.

88. X. Zhou, et al., “Cascaded two-modulus algorithm for blind polarization de-multiplexing of 114-Gb/s PDM-8QAM optical signals”. in Optical Fiber Communication Conference, 2009, paper OWG3.

89. M. G. Taylor, “Phase estimation methods for optical coherent detection using digital signal processing”. *Journal of Lightwave Technology*, 2009. 27(7): p. 901-914.

90. S. Dris, et al., “M-QAM carrier phase recovery using the viterbi-viterbi monomial-based and maximum Likelihood Estimators”. in Optical Fiber Communication Conference and Exposition and the National Fiber Optic Engineers Conference, 2013, paper OTu3I.3.

91. G. Picchi, et al., “Blind equalization and carrier recovery using a" stop-and-go" decision-directed algorithm”. *IEEE Transactions on Communications*, 1987. 35(9): p. 877-887.

92. J. Pan, et al., “Digital pre-shaping for narrowband filtering impairment compensation in superchannel applications”. in Optical Sensors, 2013, paper JT3A.1.

93. J. Li, et al., “Spectrally efficient quadrature duobinary coherent systems with symbol-rate digital signal processing”. *Journal of Lightwave Technology*, 2011. 29(8): p. 1098-1104.

94. J. Li, et al., “Approaching Nyquist limit in WDM systems by low-complexity receiver-side duobinary shaping”. *Journal of Lightwave Technology*, 2012. 30(11): p. 1664-1676.

95. E. Tipsuwannakul, et al., “Performance comparisons of DP-16QAM and duobinary-shaped DP-QPSK for optical systems with 4.1 Bit/s/Hz spectral efficiency”. *Journal of Lightwave Technology*, 2012. 30(14): p. 2307-2314.

96. J. Pan, et al., “DAC enabled frequency domain pre-shaper design for nyquist signaling”. in Signal Processing in Photonic Communications, 2014, paper SM3E.2.

97. X. Liu, et al., “Phase-conjugated twin waves for communication beyond the Kerr nonlinearity limit”. *Nature Photonics*, 2013. 7(7): p. 560-568.

98. T. Xu, et al., “Analytical estimation of phase noise influence in coherent transmission system with digital dispersion equalization”. *Optics Express*, 2011. 19(8): p. 7756-7768.

99. A. Stark, et al., “Filter bandwidth and subcarrier spacing tolerance of single-carrier 32 GBaud PDM-QPSK”. in Photonics Society Summer Topical Meeting Series, 2011, paper TuC1.3.

100. L. Cheng, et al., “Joint digital signal processing for superchannel coherent optical systems: Joint CD compensation for joint ICI cancellation”. in European Conference and Exhibition on Optical Communication, 2012, paper Th.1.A.4.

101. J. Pan, et al., “Inter-Channel crosstalk cancellation by MAP detection for Nyquist-wdm superchannel”. in Signal Processing in Photonic Communications, 2012, paper SpTu3A.3.

102. J. Pan, et al., “Fractionally-spaced frequency domain linear crosstalk cancellation with spectral alignment techniques for coherent superchannel optical systems”. in Optical Fiber Communication Conference/National Fiber Optic Engineers Conference, 2013, paper OW4B.6.

103. A. Tumewu, et al., “Phase-based alignment of two signals having partially overlapped spectra”. in IEEE International Conference on Acoustics, Speech and Signal Processing, 2009.

104. J. Proakis and M. Salehi, Digital communications. 2008: McGraw Hill.

105. O. Zia-Chahabi, et al., “Efficient frequency-domain implementation of Block-LMS/CMA fractionally spaced equalization for coherent optical communications”. I*EEE Photonics Technology Letters,* 2011. 23(22): p. 1697-1699.

106. P. Poggiolini, et al., “A detailed analytical derivation of the GN model of non-linear interference in coherent optical transmission systems”. 2012.

107. P. Poggiolini, et al., “Analytical modeling of nonlinear propagation in uncompensated optical transmission links”. *IEEE Photonics Technology Letters*, 2011. 23(11): p. 742-744.

108. A. Carena, et al., “EGN model of non-linear fiber propagation”. *Optics Express*, 2014. 22(13): p. 16335-16362.

109. Y. T. Hsueh, et al., “Nonlinearity-enhanced crosstalk effects for a 112 Gb/s PDM-QPSK transmission over 1620-km SSMF”. in Photonics Conference (PHO), 2011, paper WEE2.

110. J. Pan, et al., “Gaussian noise model aided in-band crosstalk analysis in ROADM-enabled DWDM networks”. in Optical Fiber Communication Conference. 2014, paper Th1I.1.